Diffusion of silver in 6H-SiC

by

Thulani Thokozani Hlatshwayo

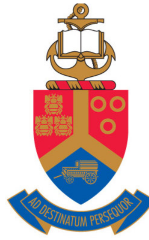

Submitted in partial fulfilment of the requirements for the degree of

DOCTOR OF PHILOSOPHY (PhD) {PHILOSOPHIAE DOCTOR} in Physics

in the Faculty of Natural and Agricultural Sciences at the University of Pretoria

July………2010

Supervisor/Promoter: Prof. J.B. Malherbe

Co-supervisor: Prof. E. Friedland

© University of Pretoria

UNIVERSITEIT VAN PRETORIA
UNIVERSITY OF PRETORIA
YUNIBESITHI YA PRETORIA

Summary

Diffusion of silver in 6H-SiC

by

Thulani Thokozani Hlatshwayo

Submitted in partial fulfillment of the requirements for the degree of (PhD) in Physics in the Faculty of Natural and Agricultural Science, University of Pretoria

Supervisor/Promoter: Prof. J.B. Malherbe
Co-Supervisor: Prof. E. Friedland

SiC is used as the main diffusion barrier in the fuel spheres of the pebble bed modular reactor (PBMR). The PBMR is a modern high temperature nuclear reactor. However, the release of silver from the fuel spheres has raised some doubts about the effectiveness of this barrier, which has led to many studies on the possible migration paths of silver. The reported results of these studies have shown largely differing results concerning the magnitude and temperature dependence of silver being transported through the fuel particle coatings. Results from earlier investigations could be interpreted as a diffusion process governed by an Arrhenius type temperature dependence. In this study, the silver diffusion in 6H-SiC was investigated using two methods.

In the first method a thin silver layer was deposited on 6H-SiC by vapour deposition while in the second method silver was implanted in 6H-SiC at room temperature, 350 ^{o}C and 600 ^{o}C to a fluence of 2×10^{16} silver ions cm^{-2}. Finally the effect of neutron irradiation on the diffusion of silver was investigated for the samples implanted at 350 ^{o}C and 600 ^{o}C.

Silver depth profiles before and after annealing were determined by Rutherford backscattering (RBS). Both isothermal and isochronal annealing were used in this

study. Diffusion coefficients as well as detection limits were extracted by comparing the silver depth profiles before and after annealing. The radiation damage after implantation and their recovery after isothermal and isochronal annealing were analysed by Rutherford backscattering spectroscopy combined with channelling.

The results of in-diffusion of silver into 6H-SiC at temperatures below the melting point (960 ^{o}C) using un-encapsulated 6H-SiC samples with 100 nm deposited silver indicated no in-diffusion of silver; however, disappearance of silver occurred at these temperatures. For the encapsulated samples, no in-diffusion of silver was observed at 800 ^{o}C, 900 ^{o}C and 1000 ^{o}C but silver disappeared from the samples' surface and was found on the walls of the quartz glass ampoule. This disappearance of silver was established to be due to the wetting problem that existed between silver and SiC.

The room temperature implantation resulted in a completely amorphous surface layer of approximately 270 nm thick. Epitaxial re-growth from the bulk was already taking place during annealing at 700 ^{o}C and the crystalline structure seemed to be fully recovered at 1600 ^{o}C, for samples that were sequentially isochronally annealed from 700°C in steps of 100 ^{o}C up to 1600 ^{o}C. However, no silver signal was detected at this temperature, which left certain doubts regarding the crystalline structure of the samples at this temperature. This was speculated to be due to thermal etching of the top original amorphous layer while the deeper amorphous layer was epitaxial re-growth from the bulk. The decomposition of SiC, giving rise to a carbon peak in the RBS spectra due to evaporation of Si, was clearly observed on the same samples at 1600 ^{o}C. Isothermal annealing at 1300 ^{o}C for 10 h cycles up to 80 h caused epixatial re-growth from the bulk during the first annealing cycle (10 h). No further epitaxial re-growth from the bulk was observed up to 80 h. This was believed to be due to the amorphous layer re-crystallising into crystals that were randomly oriented to the 6H-SiC substrate.

No diffusion of silver was observed at temperatures below 1300 ^{o}C but silver seemed to form precipitates at these temperatures. Diffusion of silver towards the surface accompanied by silver loss from the surface began at 1300 ^{o}C and was very high at 1400 ^{o}C, with silver profiles becoming asymmetric and closer to the surface. The loss of silver was already taking place at 1100 ^{o}C. This loss was found to be due to the

following: diffusion of silver towards the surface; the mass flow of silver via holes that were observed to be becoming larger with higher annealing temperatures on SiC surfaces and thermal etching of SiC. Isothermal annealing at 1300 ^{o}C for 10 h up to 80 h caused diffusion of silver during the first annealing cycle, while no further diffusion was observed for any further annealing at the same temperature up to 80 h. The diffusion coefficient was not calculated due to the lack of information on the structural evolution of SiC during the first annealing cycle. Isothermal annealing at 1300 ^{o}C and 1350 ^{o}C for 30 minute cycles up to 120 minutes caused high diffusion during the first cycle and reduced diffusion during the second cycle, while no diffusion was observed for any further annealing longer than the second cycle. The higher diffusion during the first 30 minutes was due to ion induced amorphization. The diffusion of silver in amorphised SiC was measured at different temperatures in the range 1300 ºC to 1385 ^{o}C and yielded to $D_0 \sim 1.4 \times 10^{-12}$ m^{2}s^{-1} and $E_a \sim 3.3 \times 10^{-19}$ J. These values were found to be approximately the same as the values of silver diffusion in polycrystalline CVD-grown SiC found by our group which were due to grain boundary diffusion: $D_o \sim 4\times10^{-12}$ m^2 s^{-1} and $E_a \sim 4\times10^{-19}$ J.

Implantation of silver at 600 ^{o}C retained crystallinity although distortions occurred in the implanted region while implantation at 350 ^{o}C also retained crystallinity but more distortions occurred as compared to silver implanted at 600 ^{o}C. This was caused by the fact that at 600 ^{o}C, the displaced atoms were more mobile because of their higher thermal energy than at 350 ^{o}C. The higher thermal energy increased the probability of the displaced atoms combining with their original lattice sites. Annealing of these samples at 1300 ^{o}C, 1350 ^{o}C and 1500 ^{o}C caused the annihilation of some defects but certain others were retained.

No diffusion of silver was observed during annealing of the samples (implanted at 350 ^{o}C and at 600 ^{o}C) at 1300 ^{o}C, 1350 ^{o}C and 1500 ^{o}C but silver moved towards the surface at 1500 ^{o}C. The upper limit of the diffusion coefficient of $D < 10^{-21}\ m^2s^{-1}$ was obtained at 1300 ^{o}C. The movement of silver towards the surface was found to be due to thermal etching at 1500 ^{o}C. Neutron irradiation of these samples caused no silver diffusion but silver ^{110m}Ag, due to ^{109}Ag capturing a neutron during neutron irradiation, was detected in the samples.

DECLARATION

I, Thulani Thokozani Hlatshwayo, declare that the thesis, which I hereby submit for the degree of PhD in Physics at the University of Pretoria is my own work and has not previously been submitted by me for a degree at this or any other tertiary institution.

Signature: ……………………………………………………………

Date: …………………………………………………………………

UNIVERSITEIT VAN PRETORIA
UNIVERSITY OF PRETORIA
YUNIBESITHI YA PRETORIA

Acknowledgements

I would like to acknowledge the following people for their valuable contribution towards the completion of my PhD work.

- My academic promoter, Prof. J.B. Malherbe, my co-promoter Prof. E. Friedland, Dr. N.G. van der Berg, A.J. Botha and Prof. C.C. Theron for their tireless guidance, discussions and support throughout this study.

- The head of department, Prof. J.B. Malherbe, for arranging some part-time work in the department, which helped in supporting my family financially.

- Mr. J. Smith, G. Pretorius and Mr. J. Jan van Ransburg, for all the help they provided with the accelerator.

- Dr. L. Prinsloo, for all the help she provided with the Raman.

- SANHARP, for the Bursaries that enabled my study to progress smoothly.

- Fellow senior students in the physics department, for their encouragement and moral support.

- My parents, my wife and my sons for their understanding, never ending love and encouragement throughout my studies and beyond.

UNIVERSITEIT VAN PRETORIA
UNIVERSITY OF PRETORIA
YUNIBESITHI YA PRETORIA

TABLE OF CONTENTS

CHAPTER 1 Introduction _____ *1*

1.1 REFERENCES _____ **5**

CHAPTER 2 DIFFUSION _____ *6*

2.1 DIFFUSION MECHANISMS _____ **9**
2.1.1 VACANCY MECHANISM _____ 9
2.1.2 INTERSTITIAL AND INTERSTITIALCY MECHANISMS _____ 9
2.1.3 HIGH DIFFUSIVITY PATHS _____ 10

2.2 ANALYSING DIFFUSION COEFFICIENTS _____ **11**
2.2.1 DETERMINING DIFFUSION COEFFICIENTS _____ 11

2.3 REFERENCES _____ **13**

CHAPTER 3 ION IMPLANTATION _____ *14*

3.1 STOPPING POWER _____ **14**
3.1.1 NUCLEAR STOPPING _____ 16
3.1.2 ELECTRONIC STOPPING _____ 18

3.2 ENERGY LOSS IN COMPOUNDS _____ **20**

3.3 ENERGY STRAGGLING _____ **21**

3.4 RANGE AND RANGE STRAGGLING _____ **24**

3.5 ION CHANNELLING _____ **26**

3.6 SIMULATION OF ION IMPLANTATION _____ **31**

3.7 REFERENCES _____ **35**

CHAPTER 4 ANALYTICAL TECHNIQUES _____ *37*

4.1 RUTHERFORD BACKSCATTERING SPECTROSCOPY - CHANNELLING (RBS-C) _____ **37**
4.1.1 ACCELERATOR, SCATTERING CHAMBER AND DETECTOR SYSTEM _____ 37
4.1.2 DETAILS OF RUTHERFORD BACKSCATTERING SPECTROSCOPY _____ 41
4.1.3 KINEMATIC FACTOR _____ 41
4.1.4 DEPTH PROFILING _____ 42
4.1.5 DIFFERENTIAL CROSS SECTION _____ 44

4.2 RUTHERFORD BACKSCATTERING SPECTROSCOPY COMBINED WITH CHANNELLING (RBS-C) _____ **45**

4.3 SCANNING ELECTRON MICROSCOPY (SEM) _____ **49**

4.4 REFERENCES _____ **54**

CHAPTER 5 EXPERIMENTAL PROCEDURE _____ *55*

5.1 SAMPLE PREPARATION _____ **55**

5.2 DEPOSITION _____ **57**

5.3 IMPLANTATIONS _____ **58**

5.4 ANNEALING SYSTEMS _____ **59**

5.5 DATA ACQUISITION _____ **65**

5.6 DATA ANALYSES _____ **67**

5.7 ERROR ANALYSES _____ **69**

5.8 REFERENCES ____ 70

CHAPTER 6 REVIEW OF PREVIOUS RESULTS ____ 71

6.1 BATCH MEASUREMENTS ____ 72

6.2 INDIVIDUAL INVENTORY MEASUREMENTS ____ 78

6.3 ION IMPLANTATION ____ 82

6.4 DIFFUSION COUPLE METHODS ____ 85

6.5 REFERENCES ____ 87

CHAPTER 7 RESULTS AND DISCUSSION ____ 89

7.1 LAYER IN-DIFFUSION ____ 90

7.2 IMPLANTATION RESULTS ____ 93

7.2.1 ROOM TEMPERATURE IMPLANTATION ____ 93

7.2.2 HIGH TEMPERATURE IMPLANTATIONS ____ 117

7.3 REFERENCES ____ 130

CHAPTER 8 SUMMARY OF RESULTS ____ 131

8.1 SILVER IN-DIFFUSION RESULTS ____ 131

8.2 ROOM TEMPERATURE IMPLANTATION ____ 131

8.3 HIGH TEMPERATURE IMPLANTATIONS ____ 133

CHAPTER 9 APPENDIX A ____ 135

9.1 REFERENCES ____ 142

ABBREVIATIONS

ACT-Accident Condition Test

AEM-Analytical Electron Microscopy

AVR-Arbeitsgemeinschaft Versuchsreaktor

BCA-Binary Collision Approximation

BISO-Bistructural Isotropic

CAB-Core and Bonds (Model)

CFE- Cold Field Emitter

CVD-Chemical Vapour Deposition

EBSD-Electron Backscattered Diffraction

EDS-Energy Dispersive X-ray Spectroscopy

FIMA- Fissions per Initial Metal Atom

FP-Fission Product

FWHM-Full Width at Half Maximum

HTGR –High Temperature Nuclear Gas Reactor

HTTR-High Temperature Test Reactor

IPyC- Inner Pyrolytic Carbon

MCA-Multi-Channel Analyzer

MD-Molecular Dynamics

OPyC-Outer Pyrolytic Carbon

PBMR-Pebble Bed Modular Reactor

PyC-Pyrolytic Carbon

RBS-Rutherford Backscattering Spectroscopy

RBS-C- Rutherford Backscattering Spectroscopy combined with Channelling

SA PBMR-South African Pebble Bed Modular Reactor

SCA-Single Channel Analyser

SEM-Scanning Electron Microscopy

SFE-Schottky Field Emitter

TEM-Transmission Electron Microcopy

TFE-Thermal Field Emitter

TRIM-TRansport of Ions in Matter

TRISO-TRistructural ISOtropic

XPS-X-ray Photoelectron Microscopy

XRD-X-ray Diffraction

CHAPTER 1 INTRODUCTION

In a High Temperature Gas-cooled Nuclear Reactor (HTGR) safety is one of the most significant considerations. In the Pebble Bed Modular Reactor (PBMR), such as the South African Pebble Bed Modular Reactor (SA PBMR) which had been proposed – one of the HTGR safety factors is achieved by retaining the radioactive fission products (FPs) from the nuclear chain reactions in the fuel so as to avoid contamination of the primary cooling circuit components, which complicates the reactor's maintenance, thus increasing the maintenance cost and putting the personnel involved in danger.

A nuclear chain reaction is a continuous process where a slow neutron reacts with a fissile isotope which then fissions into many different FPs and fast neutrons while energy is liberated in the process. Some of the FPs are radioactive. In the HTGR the fast neutrons are cooled down by means of materials with a low neutron cross section (e.g. carbon) so that they will further react with fissile isotopes (e.g.^{235}U), to produce more heat. By passing the coolant between particles, heat is transferred to the coolant (viz. helium), which, in the direct cycle PBMR, drives the turbine motor for the purposes of electricity generation. The radioactive FPs are retained by coating layers for safety purposes.

In the modern PBMR high-temperature nuclear reactor, the fuel particles are encapsulated by chemical vapour deposited (CVD) layers which serve as a barrier in preventing the FPs' release. In recent designs the fuel kernels are surrounded by four successive layers of low-density pyrolytic carbon buffer, inner high-density pyrolytic carbon (IPyC), silicon carbide (SiC) and outer high-density pyrolytic carbon (OPyC) - see figure 1. This kind of particle is termed TRISO (TRistructural ISOtropic). The fuel kernel (UO_2) is 0.5 mm in diameter, the buffer layer is 95 μm thick, the IPyC and the thickness of the OPyC are of the order of 40 μm thick while the SiC is of the order of 35 μm. The functions of these coating layers in a TRISO particle are strongly determined by their physical and chemical properties. Carbon usage is based on the following properties: stability up to a very high temperature, a low neutron capture cross section, reasonable moderator (low *Z*), and its being non toxic and cheap. Silicon carbide usage is based on the following physical and

chemical properties: high thermal conductivity, extreme hardness, high temperature stability, small neutron capture cross-section and good dimensional stability under neutron radiation [Hua97] [Sen03]. The main functions of the low-density PyC layer, which is also known as the buffer layer, are to attenuate the fission recoils and to provide voids for the gaseous FPs and carbon monoxides that are produced. The IPyC retains gaseous fission products. The SiC layer retains solid FPs or acts as a barrier to solid FPs and provides adequate structural stability during fuel compact fabrication. The outer high-density PyC protects silicon carbide mechanically. In the pebble bed reactor, 11,000-15,000 fuel particles are mixed with a graphite (5 mm) material to form a 60 mm diameter fuel spheres known as pebbles. These pebbles are inserted from the top of the core in the reactor and circulate from the top to the bottom until they have reached minimal burn up.

At the high end of the envisaged operating temperatures of the PBMR, the TRISO particles quite effectively retain most of the important FPs such as cesium, iodine, xenon and krypton, but the release of silver seems to present a major problem. The failure of these particles to retain silver has raised concerns about the effectiveness of the SiC layer as a layer that is impenetrable to fission fragments, despite the low fission yield of the stable ^{109}Ag (0.03% for ^{235}U) and its low conversion rate of 0.1% ^{110m}Ag by neutron capture. ^{110m}Ag is considered to be one of the dangerous FPs because of its longer half- life ($t_{1/2}$ = 253 days) and the high gamma-rays dose rate.

Due to this problem with respect to silver, a number of studies have been undertaken in order to understand its migration mechanism, but to date the results are contradictory. For example, the studies by [Nab77] and [Min00] have indicated that a significant amount of ^{110m}Ag was released from the coated particles at high temperatures ranging from 1500 ^{o}C to 1700 ^{o}C, which was strongly believed to be associated with its migration through grain boundaries of the coated polycrystalline SiC enhanced by traces of free silicon [Nab77]. However, in a follow-up study it was revealed that particle-particle variations in the release behaviour of silver could not be explained only by the presence and/or absence of cracks in the SiC coating layer [Min00]. In addition, the work by MacLean et al [Mac02], [Mac03] and [Mac04] indicated that silver did not move by diffusion, neither in the matrix nor along grain boundaries; hence a flow mechanism through nano-pores was suggested as the

possible migration path. The study by Jiang et al [Jia04] indicated that there is no significant diffusion of implanted silver in single crystalline SiC during annealing at a temperature up to 1300 ^{o}C, but that the silver tends to diffuse towards the surface in amorphous SiC at 1300 ^{o}C. The contradiction in the above results might be due to the structural differences between the samples investigated since they were manufactured by different manufacturers. In order to better understand the migration path of silver through a CVD-SiC layer of a TRISO particle, one needs first to understand the diffusion in single crystalline SiC and then that in polycrystalline SiC. From the various measurements that have been carried out on such systems [Nab76] [Mac04] [Jia04] no consistent diffusion coefficients of silver have been determined. The published results differ by more than several orders of magnitude. In order to understand the transport of silver through SiC coatings, the importance of volume and grain boundary diffusion and the effects of radiation damage on these two have to be clarified.

In this thesis the diffusion of silver in single crystalline SiC (6H-SiC) was investigated. This should to yield in the same results as in single crystalline SiC (3C-SiC) because they only differ in stacking order as explained in chapter 3. Two methods were used in our investigations. For analyses of in-diffusion, a silver layer was deposited onto clean single crystalline 6H-SiC samples. The samples were then annealed under a vacuum at temperatures below the melting point of silver. The post annealing Rutherford backscattering spectroscopy (RBS) and scanning electron microscopy (SEM) results indicated no in-diffusion of silver, but rather the disappearing of silver at these temperatures. This is due to a wetting problem between silver and SiC. Further in-diffusion of silver was performed by encapsulation. Samples were encapsulated in a quartz ampoule together with a silver source to maintain the silver layer on the samples' surface during annealing. The encapsulated samples were annealed at temperatures below the quartz's softening temperature (1200 ^{o}C). The post annealing RBS and SEM analyses results also indicated no in-diffusion of silver into 6H-SiC and the disappearing of silver on 6H-SiC surfaces.

Due to the negative results of in-diffusion of silver into 6H-SiC, further research was undertaken on silver diffusion in 6H-SiC. Silver was implanted in 6H-SiC at different temperatures (i.e. room temperature (23 ^{o}C), 350 ^{o}C and 600 ^{o}C for 6H-SiC) at a

fluence of 2×10^{16} cm^{-2}. The samples were then annealed from the temperatures below the melting point of silver to 1600 ^{o}C for different annealing times. Using RBS, the silver depth profiles after implantation and after annealing were compared to calculate diffusion coefficients. RBS, combined with channelling (RBS-C), was employed to investigate the production and annealing of radiation, while scanning electron microscopy (SEM) was used to investigate the changes that occurred in the samples' surfaces during annealing.

The rest of this thesis is organized as follows: Chapter 2 discusses diffusion, Chapter 3 ion implantation, Chapter 4 analytical techniques used in this thesis, Chapter 5 experimental procedures, Chapter 6 the previously published results, while Chapter 7 presents and discusses the results of this study. Chapter 8 summarises the results of this study and furnishes a number of insights into the work that still needs to be done; Chapter 9 is the appendix.

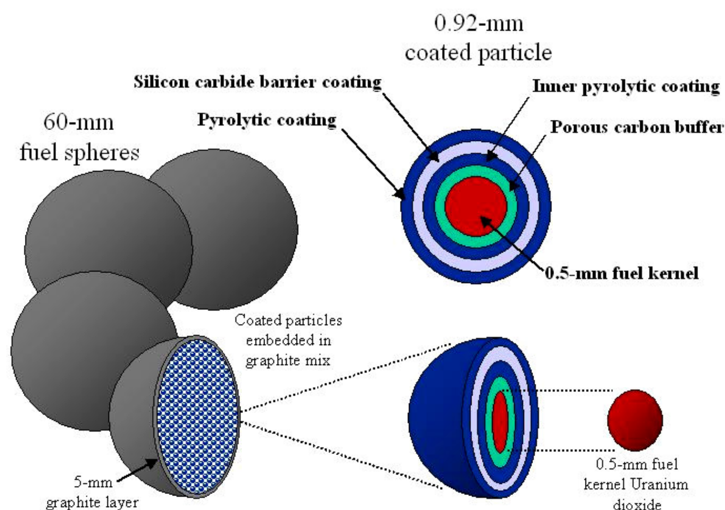

Figure 1. The fuel for a pebble-bed reactor consists of a 0.5 mm sphere of UO_2 surrounded by a porous carbon buffer, an inner layer of isotropic pyrolytic carbon, a barrier layer of SiC, and an outer layer of isotropic pyrolytic carbon which completes a TRISO particle of PBMR [www1].

1.1 REFERENCES

[Hua97] H. Huang and N. Ghoniem, J. Nucl. Mater. **250** (1997) 192.

[Jia04] W. Jiang, W.J. Weber, V. Shutthanandan, L. Li, and S. Thevuthasan, Nucl. Instr. Meth. B **219-220** (2004) 642.

[Mac02] H. J. MacLean and R. G. Ballinger, ANS Annual Winter Meeting, Washington, DC, Nov. (2002).

[Mac03] H. J. MacLean and R. G. Ballinger, ANS Global 2003, New Orleans, LA, Nov. (2003).

[Mac04] H. J. MacLean and R. G. Ballinger, 2nd International Topic Meeting on High Temperature Reactor Technology, Beijing, China, Sep. (2004).

[Min00] K. Minato, K. Sawa, T. Koya, T. Tomita, A. Ishikawa, C.A. Baldwin, W.A. Gabbard and C.M. Malone, Nucl. Tech. **131** (2000) 36.

[Nab77] H. Nabielek, P. E Brown and P. Offerman, Nucl. Tech. **35** (1977) 483

[Sen03] D. J. Senor, G. E. Youngblood, L. R. Greenwood, D. V. Archer, D. L. Alexander, M. C. Chen and G.A. Newsome, J. Nucl. Mater. **317** (2003) 145.

[www1] http://www.pbmr.co.za/contenthtml/pictureFX/imgcache/00000048.jpg, 21, October, 2008.

CHAPTER 2 DIFFUSION

Atoms in a crystal are oscillating around their equilibrium position or their lattice positions. If these oscillations are large enough the atom can change lattice sites. This can only occur if it overcomes the potential energy barrier between itself and its neighbours. The atoms in motion collide with other atoms in the same material, which causes them to move. Since collisions influence the movement of atoms, their paths form zigzags and the overall movement of the atoms exhibits an observable drift from a region of high concentration to one of low concentration in the inhomogeneous material. The movement of atoms from a region of higher concentration is called diffusion. This implies that diffusion is a transport phenomenon, which strongly depends on concentration gradients and alters the physical and chemical properties of materials.

In order to understand the diffusion process, one needs to know how fast the atoms move from the region of high concentration to the region of lower concentration. This information is provided by the diffusion coefficient. The latter is a quantity that provides information regarding how many atoms are passing through an area per unit time, as can be seen in Fick's first law [Fic55], which macroscopically connects the diffusion coefficient D and the gradient of the concentration (C) gradient to the flux J (see equation 2.1). In equation 2.1 D is calculated for the scenario where the concentration gradient does not alter over time for one-dimensional diffusion in the x direction.

$$J = -D\frac{dC}{dx} \qquad \ldots 2.1$$

However, in most systems where diffusion takes place, the concentration gradient changes over a period, and this modifies equation 2.1 for calculating the diffusion coefficient. This scenario is explained by Fick's second law which is derived from Fick's first law, i.e. equation 2.1, by assuming diffusion in the positive x-direction of a cylinder of a unit cross section and from the continuity equation:

$$\frac{\partial C}{\partial t} = -\frac{dJ}{dx} \qquad \ldots 2.2$$

If D does not depend on position, one can substitute $J=-D\frac{dC}{dx}$ into equation 2.2 to yield [She89]:

$$\frac{\partial C}{\partial t} = D\frac{\partial^2 C}{\partial x^2} \qquad ...2.3$$

This can be written for diffusion in three dimensions as:

$$\frac{\partial C}{\partial t} = D\nabla^2 C \qquad ...2.4$$

Equations 2.3 and 2.4 are solved by taking into consideration the boundary conditions. There are many examples where this has been done for different conditions of this type [Bar51]. At the temperature range where diffusion takes place, the diffusion coefficient (D) is often found to obey an Arrhenius type temperature relationship:

$$D = D_0 \exp(\frac{-E_a}{RT}) \qquad ...2.5$$

where R is the gas constant, E_a is the activation energy, D_0 is the pre-exponential factor and T is the absolute temperature.

In crystalline materials diffusion occurs mainly via defects. The types of defects found in such materials are point, extended and complex defects; all play a role in the diffusion rate. Some of these defects are introduced either during creation of the crystalline materials or during the treatment of the sample, such as the ion implantation that is used in this study. During implantation (explained in chapter 3) the defects that are retained in the implanted material depend on the implantation temperature, the implantation rate and the kind of material they are implanted into. For example, in SiC which is investigated in this study, more defects are retained for implantation at low temperatures compared to high temperatures [Wen98]. This is owing to the fact that at low temperature atoms have less kinetic energy to move around, compared to high temperature implantations where atoms possess enough kinetic energy to move around and recombine with their original lattice sites.

In crystals the defects sometimes act as locations of minimum energies for displaced impurity atoms. This requires the said atoms to have more activation energy so as to move from the sites of minimum energies to other sites. In some cases movement of atoms in a crystal seems to be the movement of vacancies. Therefore, the vacancies also possess activation energy. For example, if there are N atoms, the equilibrium number n of vacancies is given by [Kit76]:

$$\frac{n}{N-n} = \exp(-E_V / k_B T) \qquad \ldots 2.6$$

where E_V is the energy required to displace one atom from one lattice site to a lattice on the surface and k_B is the Boltzmann constant. If $n<<N$ equation 2.6 can be written as:

$$n = N \exp(-E_V / k_B T) \qquad \ldots 2.7$$

If diffusing atoms/impurities are trapped in lattice defects they can precipitate or undergo chemical reactions with the matrix elements. In such a scenario, equation 2.4 has to be adjusted in order to describe a Fickean diffusion process in the presence of a trapping mechanism. If this is done, it leads to [Soa04] [Tam95] [Kas94]:

$$\frac{\partial C_f}{\partial t} = D\frac{\partial^2 C_f}{\partial x^2} - AC_f + BC_t,\ C_f = C_f(x,t) \qquad \ldots 2.8$$

$$\frac{\partial C_t}{\partial t} = AC_f - BC_t, \quad C_t = C_t(x,t) \qquad \ldots 2.9$$

where C_t and C_f represent the concentrations of trapped and free atoms respectively. $C=C_f+C_t$ is the total concentration of ions, while B and A are the probability rates for atoms trapping and detrapping respectively and are respectively given by:

$$B = v\exp(-Et/kT) \quad \text{and} \quad A = 4\pi r_s D c_s$$

Where v is the jump frequency, E_t the activation energy for the trapping process, r_s the effective trapping radius, D the diffusion coefficient and c_s the concentration of the effective trapping centres. Equations 2.8 and 2.9 have been solved numerically using the finite difference method [Smi78] [Kas94].

2.1 DIFFUSION MECHANISMS

Since crystals display different defects such as point, planar (dislocation or stacking faults) and complex defects (defects resulting from clustering of point or planar defects) which play a role in diffusion, it is vital to understand the various mechanisms by which diffusion takes place. Therefore, in this section only the three main diffusion mechanisms are discussed. A discussion of the other mechanisms is furnished in the book by Heitjans et al. [Hei05].

2.1.1 VACANCY MECHANISM

All crystals have vacancies, i.e. lattice sites that are not occupied, and that play a role in the diffusion of impurities. If one of the neighbour atoms jumps into the vacancy, the atom is said to have been diffused by the vacancy mechanism. This is due to the fact that when atoms jump or move into the vacancies, they leave vacancies behind as a result. Therefore, during this process the vacancies seemed to have also moved or jumped in the opposite directions of the atoms, as depicted in figure 2-1. In this figure, the dotted circle and solid circle represent the vacancy and atom respectively while (a) and (b) illustrate the position before and after diffusion.

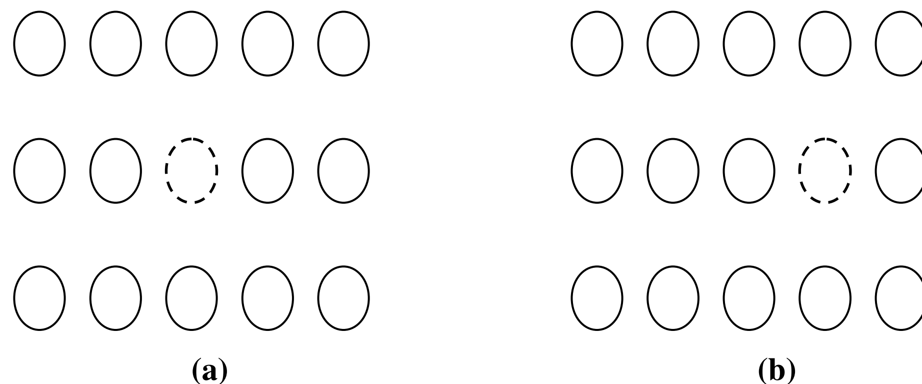

Figure 2-1: Vacancy diffusion mechanism: the dotted circle represents a vacancy, the open circles represent atoms, (a) and (b) represent positions before and after diffusion respectively.

2.1.2 INTERSTITIAL AND INTERSTITIALCY MECHANISMS

In (crystalline) materials there are atoms situated not on their regular site, but between other atoms, i.e. on the interstitial sites: they are called interstitials. Interstitial atoms can be smaller or bigger than the host atoms. Interstitial diffusion occurs when an

interstitial atom jumps from one interstitial site to the other as shown in figure 2-2, where the interstitial is depicted as an atom of smaller size. In some cases interstitial diffusion occurs faster than vacancy diffusion because there are more interstitial sites than vacancies and interstitial atoms are smaller [Sha70]. In the case where interstitial atoms are of the same size as the lattice sites, the interstitial atom can move into another normal lattice site by pushing a neighbouring normal lattice atom into an adjacent lattice site, as shown in figure 2-3. This process is known as interstitialcy diffusion [Sha70] [She89].

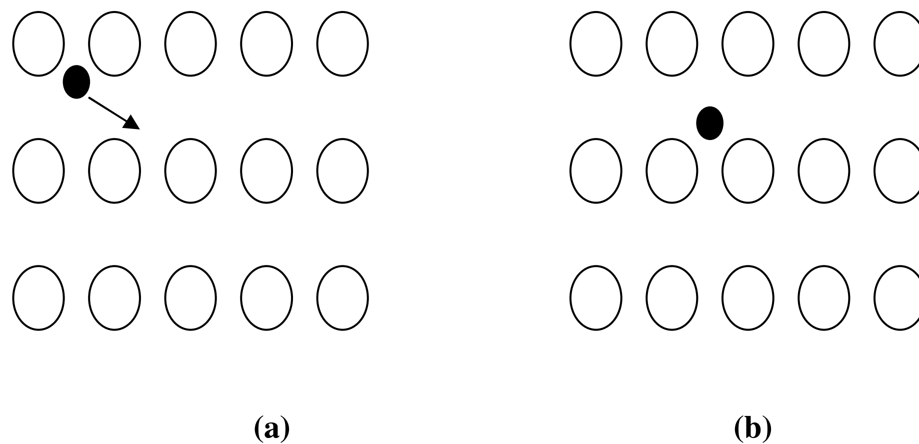

Figure 2-2: *Interstitial mechanism, (a) before and (b) after an interstitial diffusion.*

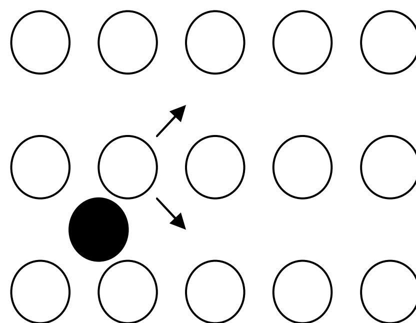

Figure 2-3: *The process of interstitialcy diffusion.*

2.1.3 HIGH DIFFUSIVITY PATHS

The diffusion mechanisms discussed above for volume diffusion are found to be temperature dependent, whereas diffusion along high diffusivity paths, i.e. via

dislocations loops, grain boundaries, surfaces, etc., is often found to be more or less temperature independent compared to the former. These kinds of diffusion mechanisms are those that take place when the regular lattice structure is broken down: for example in polycrystalline systems. Details of these mechanisms are found in [Poa78] and in references therein.

2.2 ANALYSING DIFFUSION COEFFICIENTS

There are several methods that are used in analyzing diffusion of impurities in different materials, some of which are discussed by Poate et al. and Heitjans et al. [Poa78] [Hei05]. RBS was used in this thesis. RBS is discussed in detail in chapter 4 but, briefly, it is based on the backscattering of charged particles of known incident energy (the alpha-particle was used in this study) from the specimen of interest. The backscattered alpha particles are then detected and the yield versus channel number is recorded, from which concentration and depth profiles are calculated.

2.2.1 DETERMINING DIFFUSION COEFFICIENTS

In this thesis the diffusion coefficients were determined by comparing the silver depth profiles before and after annealing steps. This was motivated by the fact that the depth profiles of our results were almost Gaussian. Fick's diffusion equation for the dilute limit leads to a particularly simple solution if the original profile at time t = 0 can be described by a Gaussian distribution [Mye74]. After annealing for a time t the concentration profile stays in a normal distribution given by [Mye74]:

$$C(x,t) = K[\pi Dt]^{-1/2} exp(-x^2/4Dt) \qquad ...2.10$$

where K is an adjustable constant, while the position of maximum concentration is unchanged at $x = 0$. If the profile width $W(t)$ is defined as the full width at half maximum *(FWHM)*, the following relationship between final and original width obeys equation 2.11.

$$[W(t)]^2 = 4Dtln(2) + [W(0)]^2 \qquad ...2.11$$

From equation 2.11, it is clear that the slope of $[W(t)]^2$ versus annealing time at constant temperature gives the diffusion coefficient D. The pre-exponential factor (D_0) and activation energy E_a to completely describe diffusion are found by establishing the diffusion coefficients at three or more different temperatures and using them to solve for the unknowns (i.e. D_0 and E_a) in the Arrhenius equation, i.e. equation 2.5.

2.3 REFERENCES

[Bar51] R. M. Barrier, Diffusion in and through Solids, Cambridge University Press, Cambridge, England (1951).

[Fick55] A. Fick, Ann. Phys. (Leipzig) **170** (1855) 59.

[Hei05] P. Heitjans and J. Karger, Diffusion in Condensed Matter, Springer (2005).

[Kas94] J. R. Kachny, M. Behar, Nucl. Instr. and Meth. B **88** (1994) 267.

[Kas96] J. R. Kaschny, M. Behar Nucl. Instr. and Meth. B **111** (1996) 51.

[Kit76] C. Kittel, Introduction to Solid State Physics, 5th ed., John Wiley and Sons, Inc. California (1976).

[Mye74] S. M. Myers, S.T. Picraux, T.S. Provender, Phys. Rev. **B9** (1974) 3953.

[Poa78] J. M. Poate, K. N. Tu, J. W. Mayer, Thin Films Interdiffusion and Reactions, John Wiley and Sons, Inc., USA (1978).

[Sha70] B. L. Sharma, Diffusion in Semiconductors, Trans. Tech. Publications, D-3392 Clausthal-Zellerfeld, Germany (1970).

[She89] P. Shewmon, Diffusion in Solids, 2nd ed., TMS, USA , (1989).

[Smi78] G.D. Smith, Numerical Solution of Partial Differential Equations: Finite Difference Methods, 2nd, ed. Oxford (1978).

[Soa04] M. R. F. Soares, L. Amaral, M. Behar, F. Fink, Nucl. Instr. and Meth. B **215** (2004) 90.

[Tam 95] S. W. Tam, J.P. Kopasz, C.E. Johnson, J. Nucl. Mater. **219** (1995) 87.

[Wen98] E. Wendler, A. Heft, W. Wesch, Nucl. Instr. and Meth. **B141** (1998) 105.

CHAPTER 3 ION IMPLANTATION

When an energetic ion penetrates a material it loses energy until it comes to rest inside the material. The energy is lost via inelastic and elastic collisions with the target atoms. When an ion has lost all its energy and comes to rest in the substrate, it is said to be implanted in the material. Consequently this technique is known as ion implantation. It is widely used in the manufacturing of semiconductors' electronic devices and in different material doping processes. If this technique is used, it is important to be able to predict the final distribution of the ions in the material. This can only be achieved if all the processes involved until the ion comes to rest inside the material of interest are clearly understood. Hence this chapter describes the most important processes that occur during ion implantation.

3.1 STOPPING POWER

Energy loss by ions in a material is the factor which determines the final distribution of ions and defects. Since the ion loses its energy (E) per penetration depth (x), where x is the distance within the target measured from the surface of the target, the energy loss in a material, which is referred to as the stopping power or energy loss, is defined as dE/dx.

An energetic ion penetrating a material loses its energy mainly via two processes which are considered to be independent of each other. They are: nuclear energy loss and electronic energy loss. Therefore, the stopping can also be separated into nuclear stopping and electronic stopping. These are described in sections 3.1.1 and 3.1.2 respectively. From the two stopping powers the total stopping power (S) can be written as:

$$S = \frac{dE}{dx} = \left(\frac{dE}{dx}\right)_n + \left(\frac{dE}{dx}\right)_e \qquad \text{....3.1}$$

where the stopping powers with subscript n and e represent nuclear and electronic stopping power respectively.

From the total stopping power S, the stopping cross section can be calculated from dividing S by target density N':

$$\varepsilon = -\frac{dE}{N'dx} \qquad \ldots 3.2$$

The penetration length R of ions with initial incident energy of E_0 is given by:

$$R = \frac{1}{N'}\int_{0}^{E_0} \frac{dE}{dx} \qquad \ldots 3.3$$

The independence of nuclear stopping and electronic stopping suggests that the stopping power is strongly dependent on the energy E of the ion, as can be observed in figure 3-1below.

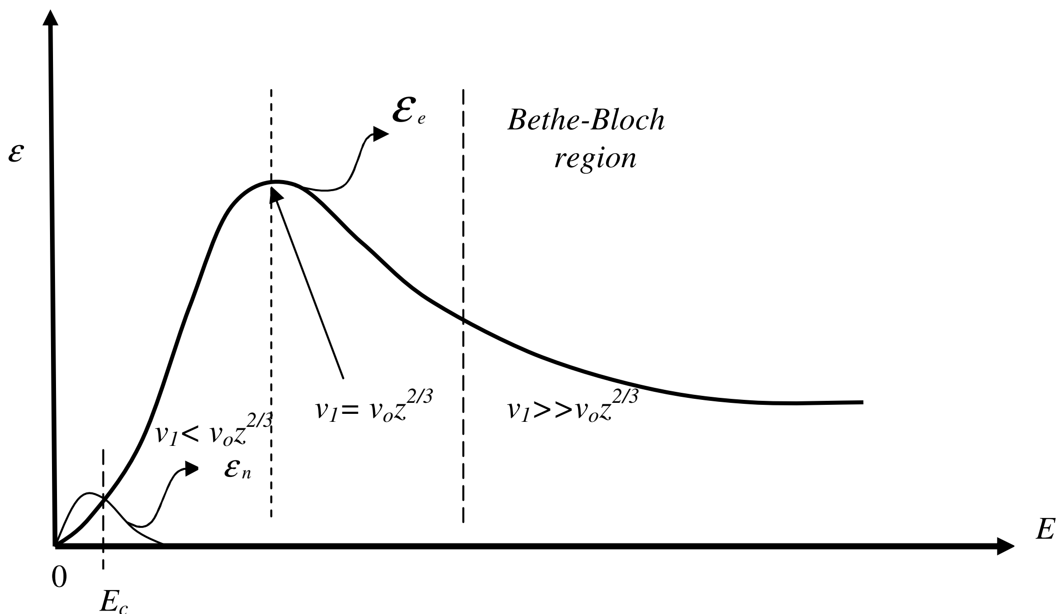

Figure 3-1: The dependences of electronic ε_e and nuclear ε_n contributions to the stopping cross section ε as a function of the ion energy E. The Bethe-Bloch equation [Bet30] is a good approximation at very high energies, v_1 is the velocity of an ion, v_o is the Bohr velocity and Z is the atomic number of the ion.

At low energies the nuclear stopping dominates while at high energy it decreases and electronic stopping dominates. Electronic stopping starts to dominate above the critical energy E_c (see figure 3-1), then reaches a maximum and decreases at the very high energy region or Bethe-Bloch region. This is caused by the shorter amount of time which the ion has to interact with the electrons of the target atoms owing to its high velocity. The details of figure 3-1 are discussed in subsections 3.1.1 and 3.1.2.

3.1.1 NUCLEAR STOPPING

Nuclear stopping power is the stopping process which includes all the processes that result in the transfer of energy from the implanted ion into the target atom as a whole. Therefore, the nuclear scattering can be described by the potential between an ion (1) and a target (2) atom. For example, in the head-on collisions case, where there is backscattering of the colliding ions from the target atoms due to repulsion between colliding ions and target nuclei, the interatomic potential between the two positive charges of ion and the target atoms can be written as:

$$V = \frac{Z_1 Z_2 e^2}{4\pi\varepsilon_0 r} \qquad \ldots 3.4$$

where Z_1 and Z_2 are the atomic numbers of ion and target respectively, e is the electron charge, ε_0 is the permittivity of free space and r is the interatomic distance. This potential is a pure Coulomb potential that does not take into account the screening effects. The scattered ions that result in a large scattering angle are said to be Rutherford backscattered. The analytical technique that is based on the analyses of the backscattered particles is discussed in chapter 4. From figure 3-1, it is evident that the probability of this Rutherford backscattering process is negligible for energetic ions since the nuclear stopping is dominant only at low energies.

There are many different methods of calculating interatomic potentials (which take screening effects into consideration): these are categorised into simple and complicated methods. The former are those that assume fixed charge distributions. In these methods different contributions to the interatomic potential are calculated independently as a function of interatomic distance r. The complicated methods are those that are performed directly from the first principles of quantum mechanics and require a large amount of numerical computations. The interatomic potentials for a wide number of atomic pairs have been calculated using the Hartree-Fock charge distributions method [Zie85] and have been found to be generally in agreement with the experimental data. From these results the analytical expression known as the universal interatomic potential was derived [Tes95]:

$$V_U = \frac{Z_1 Z_2 e^2}{4\pi\varepsilon_0 r}\Phi_U\left(\frac{r}{a_U}\right) \qquad \ldots 3.5$$

where the universal screening function $\Phi_U(x)$ and the screening radius $a_U(Z_1,Z_2)$ are given by fitted formulas [Zie85].

The energy transfer from the ion to the target atoms can be calculated using the interatomic potential between an ion and the target atom. Generally this is performed by taking into consideration the motion of all the N atoms in a system determined by N potentials. Such calculations are known as molecular dynamics (MD) simulations and are tedious but today they are used to study phenomena related to individual ion-target interactions. A simplification of this method has been developed, viz. the binary collision approximation (BCA), where collisions between two atoms at a time are considered. These methods break down at low energy when many body effects become important [Rim95].

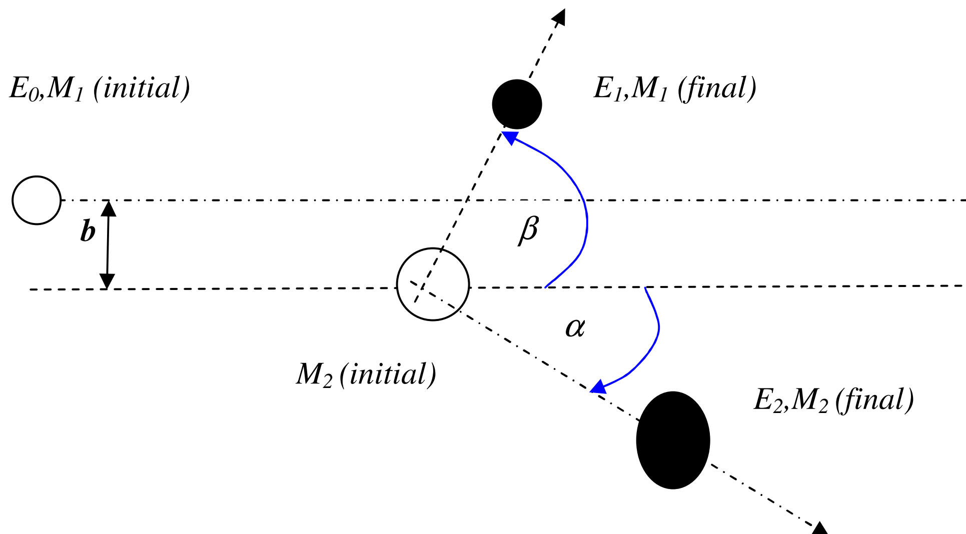

Figure 3-2: A schematic diagram showing the ion M_1 of initial energy E_0 colliding with the target atom M_2 (initial) causing it to move with E_2 and its own energy reducing to E_1.

The geometry of a collision between an energetic ion and a target atom is depicted in figure 3-2. In figure 3-2, an ion M_1 with an initial energy of E_0 is deflected by the target atom M_2. The position of M_2 relative to the M_1 trajectory is called the impact parameter and is represented by b (it is a projection of the projectile path to the target axis). During the collision M_1 and M_2 are deflected with angles relative to the M_1 original trajectory, α and β respectively. During the collision the kinetic energy T is

transferred from M_1 to M_2. From the conservation of energy and momentum the kinetic energy transfer can be calculated. When this is carried out, T is found to be a function of α, projectile energy E_0, the mass of the projectile M_1, and the mass of the target atoms M_2 in the laboratory system [Tho03]:

$$T = E_0 \frac{4M_1M_2}{(M_1 + M_2)^2} \cos^2(\alpha) \qquad \ldots 3.6$$

and in the centre of the mass system:

$$T = E_0 \frac{4M_1M_2}{(M_1 + M_2)^2} \sin^2(\frac{\alpha_c}{2}) \qquad \ldots 3.7$$

where α_c is the recoiling angle in the centre of this system.

The nuclear stopping is calculated from the integration over all the impact parameters:

$$\varepsilon_n = 2\pi \int_0^{b_{\max}} T(E, \alpha) b db \qquad \ldots 3.8$$

Using equation 3.5, a universal nuclear cross section can be determined as is done in [Zie85].

3.1.2 ELECTRONIC STOPPING

Electronic stopping is the process where an energetic ion penetrating a material loses its energy to the target electrons. The process of transferring the ion's kinetic energy to the target electrons is a complicated one compared to the nuclear stopping discussed in section 3.1.1, because it originates from different processes. Some of these are as follows: Direct kinetic energy transfers to electrons mainly due to electron-electron collisions, excitation or ionization of target atoms, excitation of conduction electrons, and excitation, ionization or electron-capture of the ion itself, etc. [Zie85a]. The complexity of these processes makes it difficult to describe the electronic energy loss in terms of one theory. Hence different models are applied for different ion energies to describe this process. The said energies are usually divided into three parts. These parts are separated by comparing the ion's velocity with the Bohr velocity $v_o = e^2/\hbar$, where e and $\hbar$ are the electron charge and Planck's constant

respectively. In this theory a hydrogen atom at 25 *keV* moves with the same velocity as its orbital electron, while helium moves with the same velocity as its orbital electrons at 252 *keV*. Hence, the ion's initial energy with velocity equal to orbital velocity can be written as a function of the ion's mass and atomic number as:

$$E = Z_1^{4/3} A_1 25 \quad keV \qquad \ldots 3.9$$

where Z_1 and A_1 are ion's atomic number and mass number respectively.

The first part is the low energy region. This is the part where the ion's velocity v_1 is less than $v_o Z^{2/3}$, i.e. $v_1 < v_o Z^{2/3}$. In this region the ion cannot transfer enough energy to the electrons that are much lower in energy than the Fermi level to excite them to unoccupied states. Therefore, in this region only electrons in the energy states close to the Fermi level contribute to energy loss. The electronic stopping for this region has been calculated by assuming a free electron gas with a density ρ that changes slightly with the location [Lin53][Lin61a][Lin61b]. In this model the electronic cross section of an ion with Z_1 can be written as [Zie85a]:

$$\varepsilon_e = \int I(v, \rho)(Z_1(v))^2 \rho dV \qquad \ldots 3.10$$

where ε_e is the electronic stopping cross section, I is the stopping interaction function of the particle (ion) of unit charge with velocity v, Z_1 is the charge of the particle, ρ is the electron density of the target and the integral is performed over each volume element dV of the target. If one considers the interaction with the charged particle to be a perturbation in the free electron gas (which is carried out by taking into account screening and polarization), then the state of the ion can be changed via charge transfers. Therefore, Z_1 in equation 3.10 can be replaced by an effective charge Z_1^*. The electron capture and electron loss depend greatly on the projectile velocity [Zie85b].

Since the transferred energy from the projectile to the target electron is proportional to the projectile velocity, the electronic stopping power is proportional to the projectile velocity as is given by [Lin53][Lin61a][Lin61b]:

$$\varepsilon_e = 19.2 \frac{Z_1^{7/6} Z_2 v_1}{(Z_1^{2/3} + Z_2^{2/3}) v_0} \left[\frac{eVcm^2}{10^{15} at} \right] \qquad \ldots 3.11$$

where the Bohr velocity $v_0 = e^2/\hbar$.

The second part is the region where the ion velocity v_1 is far greater than $v_oZ^{2/3}$ i.e. $v_1 >> v_oZ^{2/3}$. In this region the ion is fully stripped of all its electrons. The energy loss is proportional to Z_1^2 as found by Bethe and Bloch. Hence this region is known as the Bethe-Bloch region, as indicated in figure 3-1. The electronic stopping in this region is given by the Bethe-Bloch equation [Boh13][Bet30] [Blo33][And77]:

$$\varepsilon_e = \frac{4\pi Z_1^2 Z_2 e^4}{m_e v_1^2}\left[\ln\left(\frac{2m_e v_1^2}{I}\right) + \ln\left(\frac{1}{1-\beta^2}\right) - \beta^2 - \frac{C}{Z_2}\right] \qquad ...3.12$$

where m_e is the electron's mass, v_1 the velocity of the projectile, $\beta = v/c$ where c is the speed of light, I is the average ionisation potential and C/Z_2 is the shell correction. I is defined theoretically as $\ln I = \sum_n f_n \ln E_n$ and is very complicated except for simple target atoms. Here E_n and f_n are the possible energy transitions and corresponding oscillator strengths for target atoms. Hence the Thomas-Fermi model has been used to estimate I. The approximation is Bloch's rule: $I = Z_2 10\ eV$ [Blo33].

The third part is the intermediate one, i.e. between part 1 and part 2; i.e. the part where $v_1 \approx v_oZ^{2/3}$. In this case the ion is partly ionized and the electronic stopping reaches a maximum.

The important domains for the purposes of this thesis are the low and intermediate energy regions, since the study reports on the result of silver ions of 360 keV that were implanted into SiC (a low energy regime) and analysed by Rutherford backscattering spectroscopy (RBS) using 1.6 MeV α-particles (an intermediate energy regime).

3.2 ENERGY LOSS IN COMPOUNDS

The energy loss discussed to this point is that for a target consisting of one element. The energy loss in targets consisting of more than one element, i.e. the compounds, has not been discussed yet, but they are also the more common systems and are very

important in this study since we are working with SiC. Therefore, the purpose of this section is to discuss the energy loss in compounds.

If the target is a compound A_mB_n of two different elements A and B then the total stopping of an ion penetrating it can be found by using a simple additive rule. This rule is based on the assumption that the interaction processes between ions and component target are independent of the surrounding target atoms. Therefore, if the stopping cross sections of element A and B are written as ε^A and ε^B respectively, the total stopping cross section is:

$$\varepsilon^{A_mB_n} = m\varepsilon^A + n\varepsilon^B \qquad ...3.13$$

where m and n represent the relative molar fractions of the compound materials. Equation 3.13 is known as Bragg's rule [Bra05]. Experimentally the energy loss is found to slightly deviate from Bragg's rule owing to the chemical and physical state of the material. For example, deviations of the order of 10% - 20% from Bragg's rule are found in experimental results for the stopping maximum for light gases and solid compounds containing heavier elements [Zie85b][Zie88]. These deviations led to the development of a model with respect to correcting for the chemical state of the compound. This model is called the core and bonds model (CAB) [Zie88]. The CAB model estimates the compound's stopping power for compounds from the measured values of 114 organic compounds. In this model, each molecule is described as a set of atomic cores and bonds, corresponding to the non-bonding core and bonding valence electrons, respectively. Ziegler et al. [Zie88] has also used this model in calculating the stopping cross sections for some inorganic compounds. For this method to be successful, the bond structures of the compound must be known.

3.3 ENERGY STRAGGLING

An energetic ion penetrating a substrate loses its energy through many interactions with the target atoms, which result in interactions fluctuating statistically. This implies that identical ions with the same initial energy do not possess the same energy after penetrating a thickness Δx of the same medium. Hence, the energy loss ΔE is subjected to fluctuations. The ions having the energy loss ΔE caused by the stopping

powers of the material also spread to $\delta\Delta E$, which is due to statistical fluctuations in the nuclear energy loss and electronic energy loss. This discrete nature of the energy loss processes, resulting in uncertainty in energy or energy spread, is known as nuclear straggling and is depicted in figure 3-3.

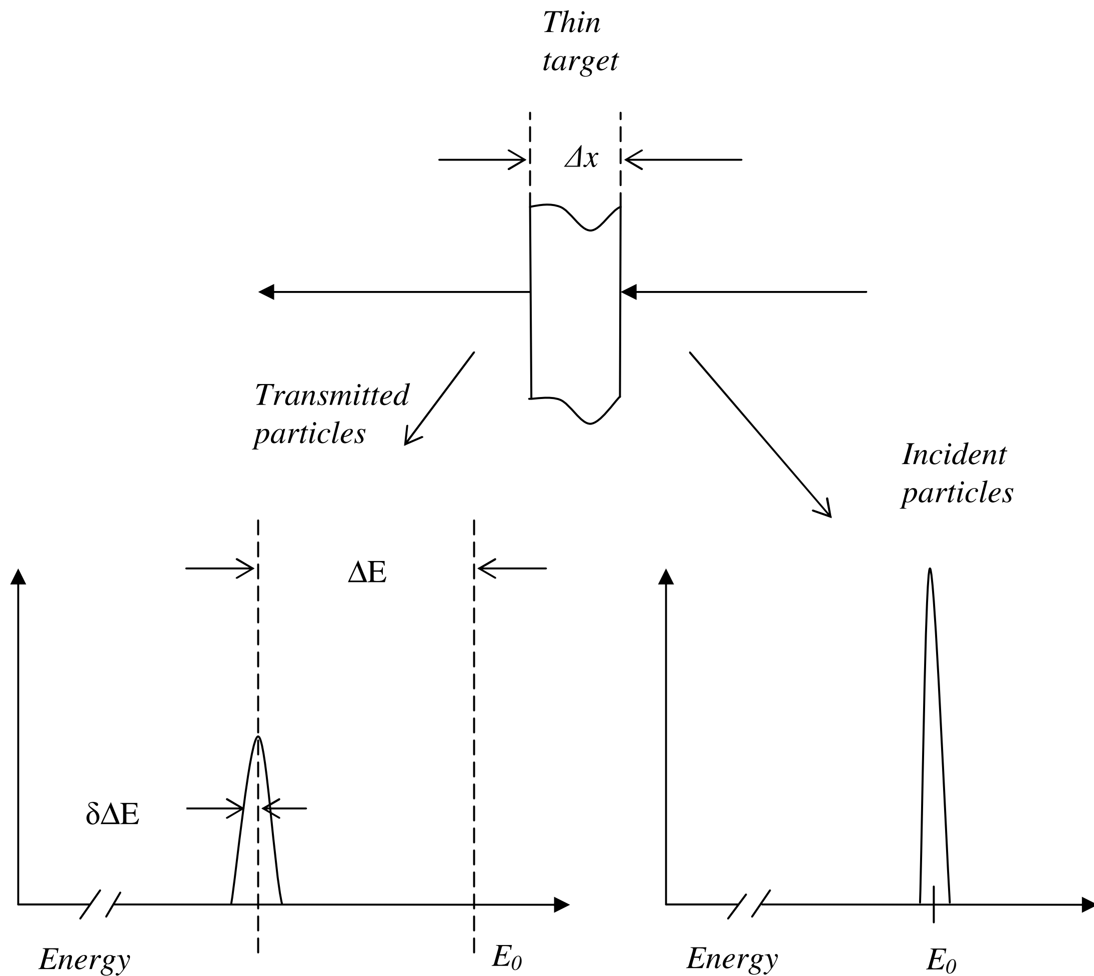

Figure 3-3: A monoenergetic beam of energy E_0 loses energy ΔE in penetrating a thin film of Δx. Simultaneously, energy straggling broadens the energy profile.

In figure 3-3, the ion with initial energy E_0 (sharp peak, right hand side of the figure) is penetrating the target of thickness $t = \Delta x$, resulting in the broadening of the energy peak (left hand side of the figure) after penetration, due to the statistical fluctuations discussed above.

The statistical fluctuations of the nuclear energy loss Q_n^2 are calculated in a similar manner to the nuclear stopping discussed in section 3.1.1, giving [Zie85b]:

$$Q_n^2 = \int_0^\infty T^2 d\sigma = 16\pi Z_1^2 Z_2^2 e^4 \frac{M_1^2}{(M_1 + M_2)^2} F_n \qquad \text{...3.14}$$

where: $F_n(\varepsilon) = \dfrac{1}{4 + 0.197\varepsilon^{-1.6991} + 6.584\varepsilon^{-1.0494}}$ and $\varepsilon = \dfrac{M_2 a}{(M_1 + M_2) Z_1 Z_2 e^2} E$

From the above equations one can perceive that when E tends to infinity then ε tends to infinity and $F_n = 0.25$. Hence, the maximum of nuclear energy loss tends to:

$$Q_n^2 = 4\pi Z_1^2 Z_2^2 e^4 \frac{M_1^2}{(M_1 + M_2)^2} \qquad \text{...3.15}$$

This result means that for high energy projectiles the importance of $Q^2{}_n$ is negligible (it becomes constant).

The straggling of electronic energy loss is derived from the Bethe – Bloch equation [Boh48]. Using the assumption of a point charge with high velocity, the following equation has been derived [Zie85a]:

$$\Omega_B^2 = 4\pi Z_1^2 Z_2 e^4 N \Delta x \qquad \text{...3.16}$$

where Ω_B^2 is called Bohr straggling. Ω_B^2 is the same as the variance of the average energy loss of a projectile after passing through a target of thickness Δx with Ω_B being the standard deviation. Therefore, the full width at half maximum of energy loss distribution is yielded by $FWHM_B = 2\Omega_B\sqrt{2\ln 2}$. The point charge assumption of Bohr has been extended by Lindhard et al. who included a correction term for energies where the assumptions may not be valid [Lin53].

The total energy straggling in a compound target is found by a linear additivity rule in a similar way to energy loss (Bragg's rule).

3.4 RANGE AND RANGE STRAGGLING

An energetic ion penetrating a material loses energy via nuclear energy loss and electronic energy loss until it comes to rest. Due to the statistical fluctuation of interactions during the energy loss processes, and multiple scattering of the ion from the target atoms, the ion's path zigzags. These statistical fluctuations cause ions with the same energy to be implanted at different depths. The total distance, which the ion travels from the surface to where it stops, is called the total range or just the range and is calculated by taking into consideration the stopping cross sections (see equation 3.3.). The deviation of the range due to energy straggling is called range straggling. Taking all these factors into account, the total range is finally given by: $R_{tot} = \sum l_i$. Where l_i represents the different paths that the ions travel inside the target (see figure 3-4.) Figure 3-4 depicts two charged particles penetrating a material, i.e. one particle with a low incident energy and another with a high incident energy. The ion with the high incident energy evidences almost a straight line path at the beginning due to electronic stopping, while at the end it tends to be a zigzag due to nuclear stopping. For the lower incident energy ion, the path is a zigzag one since the nuclear and electron stopping are of similar magnitudes. The latter takes a shorter path owing to lower energy and many deflections. The projected range R_p is defined as the average penetration depth from the target surface to where the ion comes to rest (measured parallel to the incident direction), while the perpendicular range $R_\perp$ is measured perpendicular to the direction of the incident ion. The total range is always longer than other ranges because it takes into consideration all the ion implanted paths taken inside material.

The gradual increase in the diameter of the ion beam as it passes into a sample, owing to multiple scattering of the ion inside the sample, is known as lateral spread, while the associated increasing distribution in the direction of the ions relative to the initial direction is known as the angular spread. Lateral spread and angular spread can be estimated from multiple scattering theories proposed by Sigmund and Winterbon; Markwick and Sigmund [Sig75] [Mar75]. Angular and lateral spreads also increase the path length and hence energy fluctuations, especially if the path length is not normal to the surface.

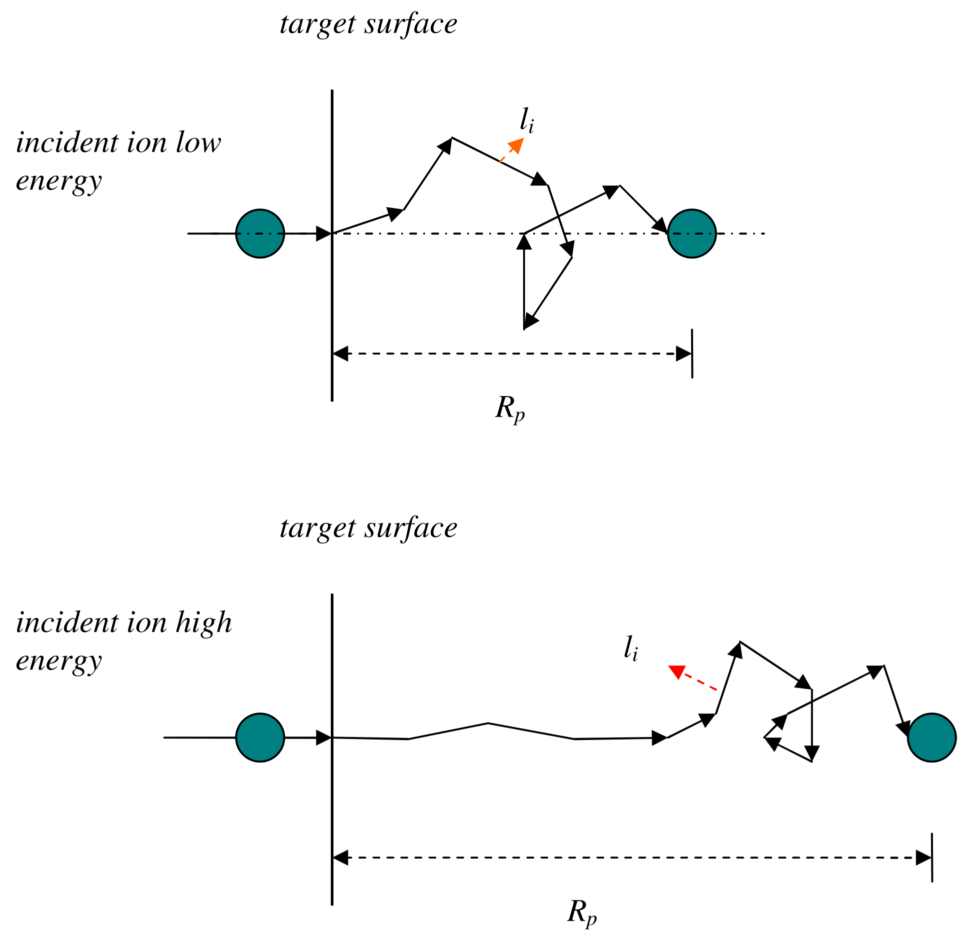

Figure 3-4: Range concepts for incident ions with low (top figure) and high (bottom figure) energies in target material.

The ions with the same initial incident energy have different impact parameters with respect to the atoms; therefore, they will not follow the same path after interacting with the target atoms. This effect varies the number of collisions which the ion undergoes and also the total range. The distribution of the final positions is usually assumed to be Gaussian, as illustrated in figure 3-5. In this figure, the projected range (R_p) is depicted. From range straggling σ the FWHM can be calculated from: FWHM $= 2\sigma\sqrt{2\ln 2}$. Our silver profiles were found to be near Gaussian. The other moments of our distribution are discussed in section 5-6.

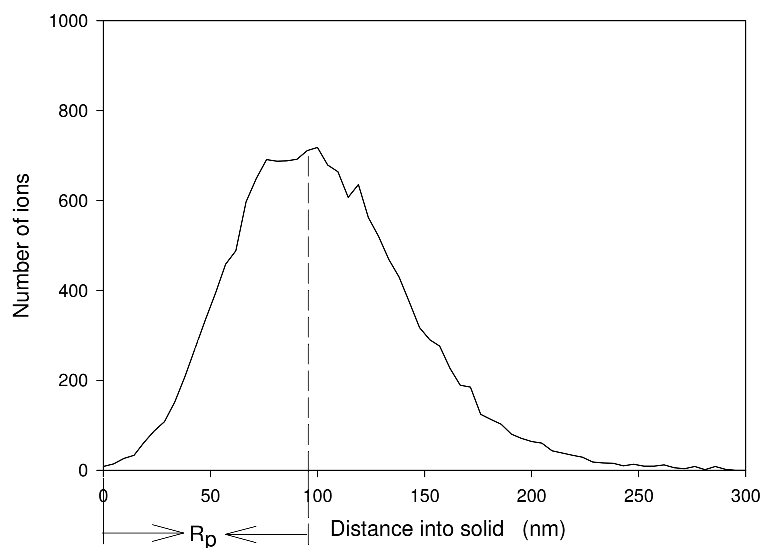

Figure 3-5: The distribution of final implanted ion positions as function of distance in the material.

3.5 ION CHANNELLING

The steering of a beam of energetic ions into open spaces between close-packed rows or planes of atoms in a crystal is called channelling. This channelling effect is illustrated in figure 3-6. The steering is the result of a correlated series of small-angle screened Coulomb scatterings between an ion and atoms bordering the channel. Therefore, channelling occurs in a crystalline solid when an ion beam is well aligned with a low index crystallographic direction. It causes a reduction in the backscattered ions or backscattered yield. This makes channelling very sensitive to crystal disorder and to small displacements of atoms from their crystalline lattice positions. Therefore, at very low fluencies, range distributions for

ions implanted in single crystals differ from those implanted in amorphous targets because of the channelling effect.

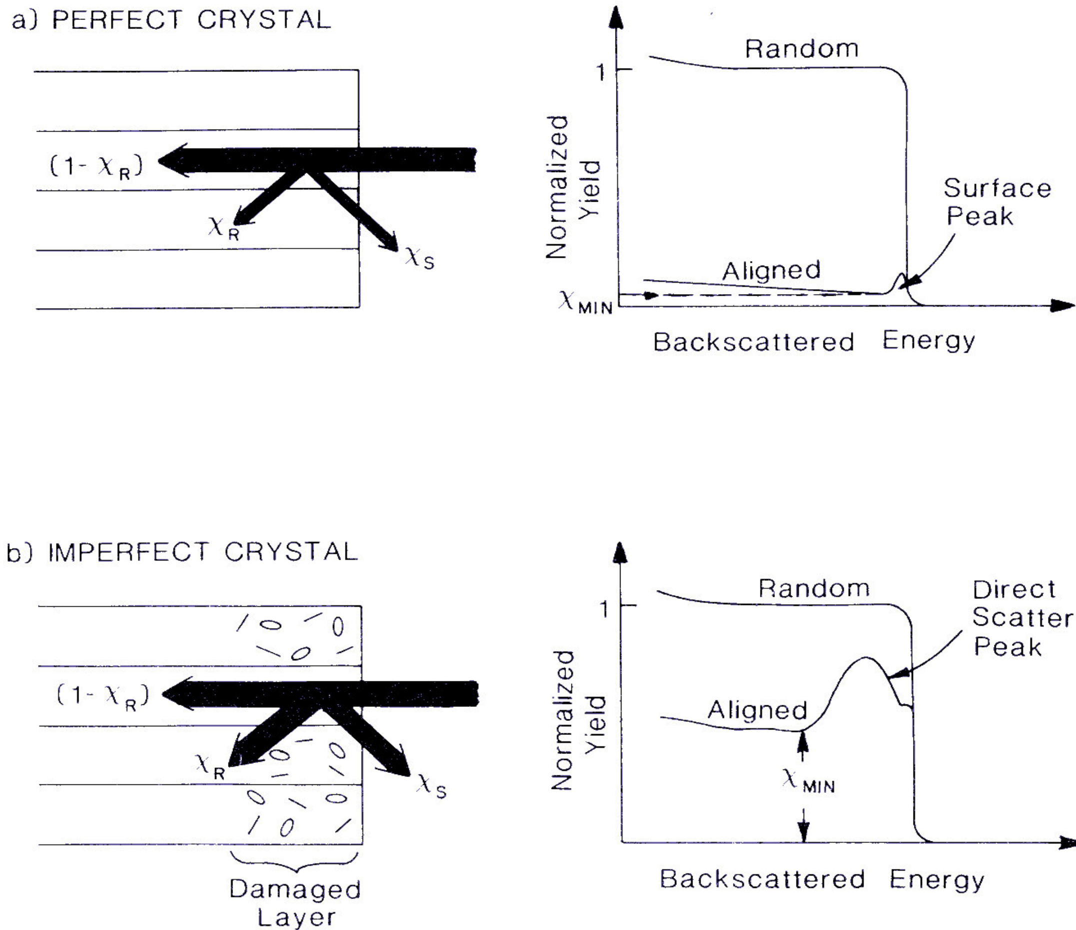

Figure 3-6: Schematic diagram showing ion channelling, dechannelling (χ_R) and direct scattering(χ_S) in a) a perfect crystal, b) an imperfect crystal. The random and aligned spectra are also shown indicating the minimum yield (χ_{MIN}) [Bir89].

For an ion beam entering a crystal parallel to a channel direction, the beam can be separated into a random component χ_R (whose path through the crystal is not affected by regular arrangement) and a channelled component (1-χ_R), which is steered along the open crystal by correlated collisions with the regular arrays of atoms. The backscattered ions χ_S represent a third component which is a very small part of an ion beam during channelling in perfect crystal (see figure 3-6). χ_S contains the information about the identity and distribution of target atoms. During the channelling process some of the channelled ions are scattered away as they penetrate into the solid and are said to be de-channelled. The small peak appearing at the surface in the

aligned RBS spectrum in figure 3-6 is due to scattering from the sample's surface. In an aligned spectrum the surface peak indicates the number of atom layers available for large angle scattering or backscattering, while the normalised yield behind the surface peak corresponds approximately to the minimum random component and is usually termed the minimum yield χ_{MIN}. Since channelling is the result of regular atomic arrangement in crystalline solids; it is sensitive to small disturbances in the crystallinity. Hence the interaction of a channelled beam with crystal defects increases the random components of the beam (by increasing the rate of dechannelling) and the direct small impact parameter collision yield, by introducing lattice atoms into the path of the channelled beam.

The axial channel is defined by rows of atoms around the trajectory i.e. the steering in 2 directions (x,y) perpendicular to the ion velocity (z-direction), while the planar channel is defined by parallel planes; i.e., is the steering of the ion in 1-direction (x) perpendicular to ion velocity (z-direction) [Bir89]. Figure 3-7 depicts the typical channelling spectra from axial and planar alignments. The planar alignment has a high backscattered yield and the spectrum contains distinct yield oscillations in the near surface region. The axial alignment on the other hand has a low minimum backscattered yield while the spectrum has only damped yield oscillation. In perfect or virgin crystals, the typical minimum yield is around 1-5% of random yield for low index axes, whereas low index planes record a minimum yield of around 10-50% of the random yield [Tes95][Gem74][Bir89].

Channelling of ions commencing their trajectories from within the crystals is also possible, namely double alignment and blocking. Double alignment refers to the situation where ions that are initial incident along a channelling direction and scattered ions are detected along the channelling direction. This results in another reduction of backscattered yield and an increase in the sensitivity to lattice disorder and atom location. Blocking denotes the situation where an ion commences its trajectory from a crystal lattice site, which might stem from the spontaneous decay of an unstable lattice atom or from some form of ion beam interaction. This results in minimum backscattering yield when viewed along certain channelling directions,

which might be due to shadowing or blocking by the crystal lattice from outside the crystal.

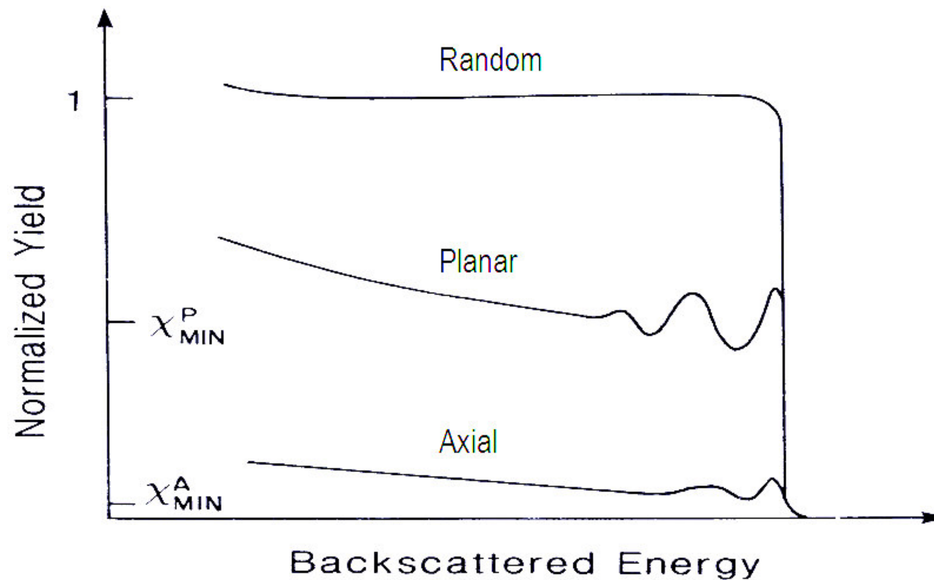

Figure 3-7: RBS-C spectra showing the result of axial and planar channelling [Bir89].

A first order approximation of channelling assumes ion scattering from atomic strings (axial channelling) and planes (planar channelling). These interactions are considered to take the form of a sequence of ion-atom collisions, as illustrated in figure 3-8. This theory is known as the continuum model. This model of channelling states that ion-string or ion-plane scattering can be approximated by scattering from a string or plane of uniform potential, which assumes that the discrete nature of the atoms is insignificant. This is a result of the fact that each steering collision is the average of many individual ion-atom collisions.

Not all the incident ions give rise to the channelling effect discussed above in this section. The channelling effect only occurs if the ion's incident angle is small. Lindhard et al. found that the channelling occurs if the incident angle of ions upon a row of atoms is less than the critical angle ψ_c [Lin65]. This critical angle is yielded by:

$$\psi_c = \left(\frac{2Z_1Z_2e^2}{E_0 d}\right)^{\frac{1}{2}} \qquad \text{....3.17}$$

where d is the atomic spacing along the aligned row and E_0 is the energy of an incident ion. ψ_c is a theoretical parameter that is not directly measured experimentally but is related to the angular half width at half $\psi_{1/2}$ of the angular scans' profiles (see figure 3-9).

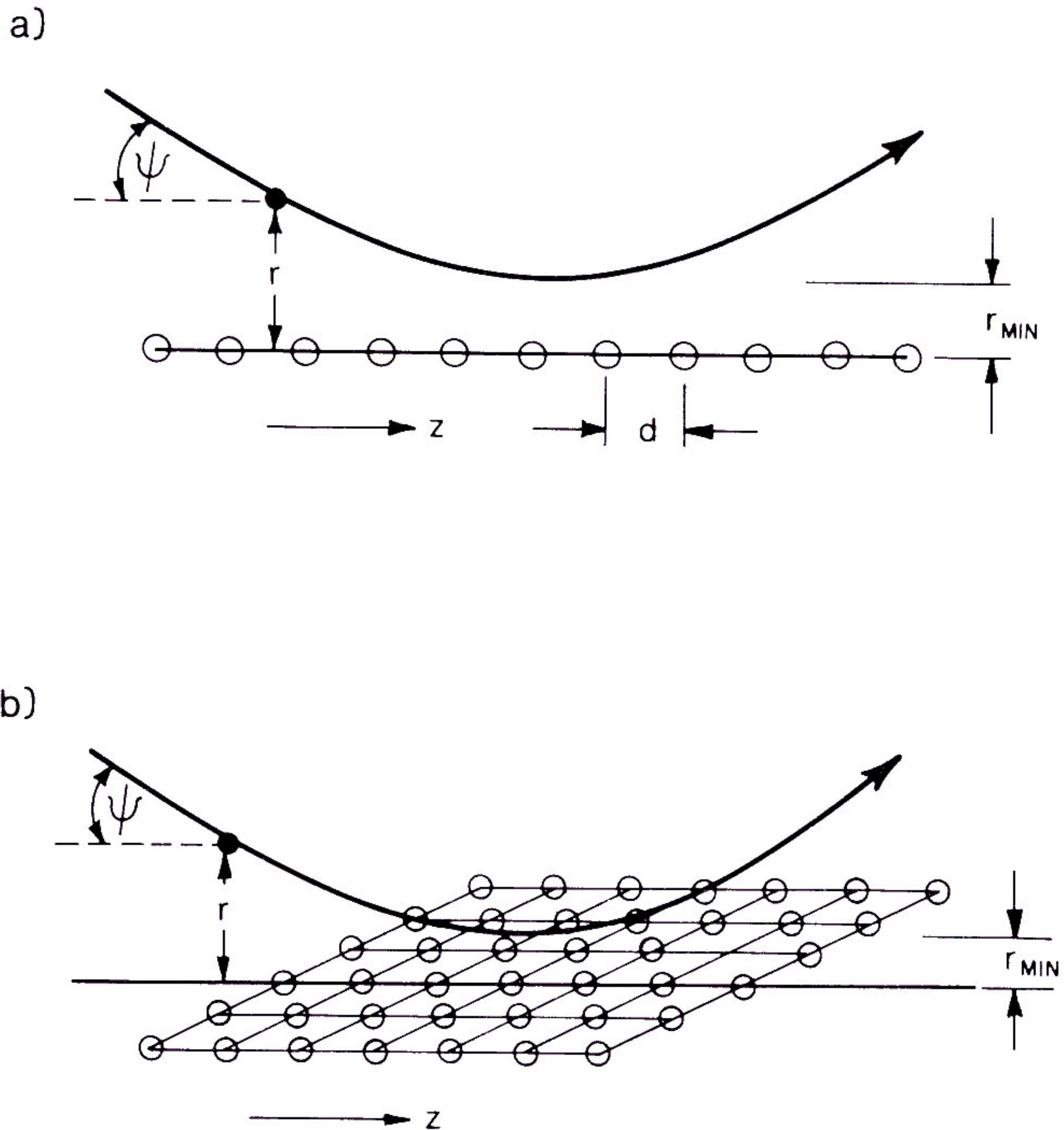

Figure 3-8: Continuum model of channelling from a string only (a) and a plane (b)[Bir89].

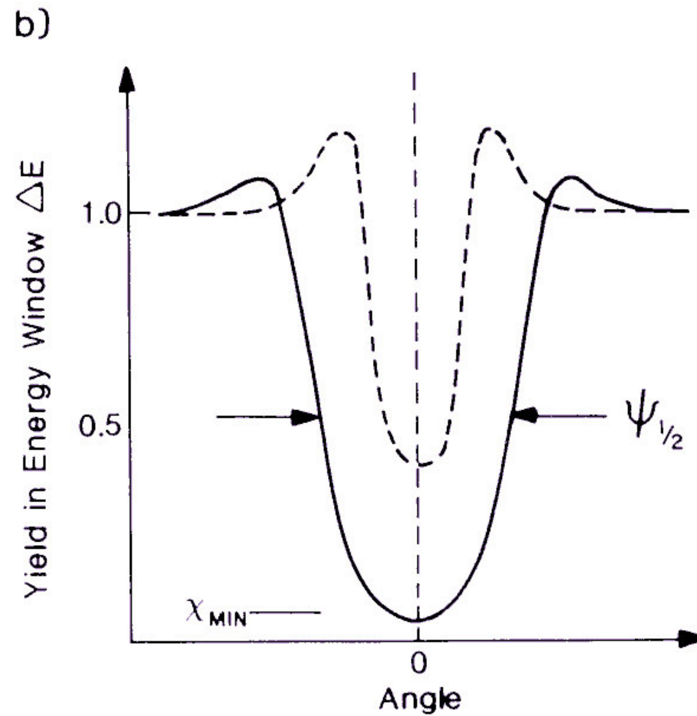

Figure 3-9: The angular yield about an axial channel (solid curve) and a planar channel (dashed curve) indicating the channelling half angle $\psi_{1/2}$ [Bir89].

The discussion of channelling in the section above indicates that channelling is an important technique in analysing the retained damage after the sample is treated, by such a method as implantation in this thesis. In this thesis Rutherford backscattering combined with channelling (RBS-C) was used to study radiation damage retained after silver implantation into 6H-SiC and after annealing. The experimental details of RBS-C are discussed in chapter 4.

3.6 SIMULATION OF ION IMPLANTATION

In order to gain an idea of the ion implantation results before performing the experiment, it is important to start by simulating it. This affords an idea of the expected experimental results. This section discusses the computer simulation performed before the implantation of silver into silicon carbide.

For simulation of ion implantation, radiation damage, sputtering and the reflection and transmission of impinging ions, a computer simulation of slowing down and scattering of ions in materials can be used. In this study the transport of ions in matter (TRIM 98) program was used [Zie85a]. It was developed for determining the ion range, damage range and damage distributions as well as the angular and energy distributions of backscattered and transmitted ions in amorphous targets. Therefore, this program does not take into consideration the channelling of bombarding ions. This program has displays high computing efficiency and maintains a moderate degree of accuracy with approximately 5-10% error. This efficiency is achieved by the fact that TRIM does not take into account the crystal structure or dynamic composition changes in the material that occurs when the ion penetrates materials, since approximations are used in this program. Approximations include the following:

- binary collision (i.e. the influence of neighbouring atoms is neglected);
- recombination of knocked off atoms (interstitials) with the vacancies is neglected;
- the electronic stopping power is an averaging fit from a large number of experiments;
- the interatomic potential as a universal form which is an averaging fit to quantum mechanical calculations;
- the target atom which reaches the surface can leave the surface (be sputtered) if it possesses enough momentum and energy to pass the surface barrier;
- the system is layered, i.e. simulation of materials with composition differences in 2D or 3D is not possible.

During simulation the ion is assumed to change direction as a result of binary nuclear collisions and to move in straight free-paths between collisions. The nuclear and electronic energy losses are considered to be independent, and the ion track is terminated either when the energy drops below a pre-specified value or when the ion position is outside the target in this program. TRIM 98 only works in the ion energy range of approximately 0.1 keV to several MeV, depending on the masses involved [Zie85]. Since nuclear and electronic energy losses are independent, the ions lose energy in discrete amounts in nuclear collisions and continuously in electronic interactions.

The TRIM 98 results of 360 keV silver ions implanted in 6H-SiC, as used in this study, are depicted in figure 3-10 where the simulated silver depth profile is compared with a typical silver depth profile from RBS (the black crossed one). The silver peak from TRIM 98 is almost a Gaussian distribution with the projected range (R_p) =106 *nm*, skewness (γ) = 0.06, kurtosis (β) =2.78 and straggling (σ) = 27 *nm*. The silver profile moments obtained from the typical silver profile measured by RBS are shown at the top of figure 3-10. R_p is in agreement with TRIM predictions but the higher moments are not in agreement with these. TRIM 98 results also indicate that displacement damage starts at the depth of 3 *nm* with the displacement peak situated at about 5 *nm*. The electronic energy loss is higher at the beginning but reduces as it enters deeper into the target, while nuclear energy loss increases. This is due to the fact that as the ion gets deeper into the target, its energy decreases, resulting in increased nuclear energy loss as explained at the beginning of this chapter. The discrepancy between simulation and our RBS results is due to approximations used during TRIM calculations as explained above.

Figure 3-10: Results of Trim 98 calculations for silver (360 keV) implanted on 6H-SiC. A typical silver depth profile (black crosses) measured by RBS is also included on the top figure. The range moments shown in the top figure are obtained from the RBS-measured silver profile.

3.7 REFERENCES

[And77] H.H. Andersen and J.F. Ziegler, Hydrogen Stopping Power and Ranges in all Elements, Vol. 3, Pergamon Press, New York (1977).

[Bet30] H. Bethe, Ann. Phys. (Leipzig) **5** (1930) 324.

[Bic84] H. Bichsel, ICRU Report, **37** (1984)130.

[Bir89] J. R. Bird and J. S. Williams, Ion Beams for Materials Analysis, Academic Press, Australia (1989).

[Blo33] F. Bloch, Ann. Phys. (Leipzig) **16** (1933) 285.

[Boh13] N. Bohr, Phil. Mag., **25** (1913) 10.

[Boh40] N. Bohr, Phys. Rev., **58** (1940) 654.

[Boh41] N. Bohr, Phys. Rev., **59** (1940) 270.

[Boh48] N. Bohr, Matt. Fys. Medd. Dan Vid. Selsk., **24** (1948) 19.

[Bra05] W.H. Bragg and R. Kleeman, Phil. Mag. **10** (1905) 318.

[Car76] G. Carter and W. A. Grant, Ion Implantation of Semiconductor, eds. A. H. W. Beck and J. Lamb, Edward Arnold, London (1976).

[Chu78] W. K. Chu, J. W. Mayer and M. A. Nicolet, Backscattering Spectrometry, Academic Press, New York (1978).

[Gem74] D. S. Gemmell, Rev. Mod. Phys. **46** (1974)129.

[Lin53] J. Lindhard, M. Scharff, K. Dan. Vidensk. Selsk. Mat. Fys. Medd. **33** (1953) No. 15.

[Lin61a] J. Lindhard and M. Scharff, Phys. Rev. **124** (1961) 128.

[Lin61b] J. Lindhard, M. Scharff and K. Dan. Vidensk. Selsk. Mat. Fys. Medd., **33** (1953) No. 14.

[Lin65] J. Lindhard, K. Dan. Vidensk. Selsk, Mat. Fys. Medd. **34** (1965) No. 14.

[Mar75] A. D. Marwick and P. Sigmund, Nucl. Instr. and Meth. **126** (1975) 317.

[Rim95] E. Rimini, Ion Implantation: Basics to Device Fabrication, Kluwer Academic Publisher (1995).

[Sig75] P. Sigmund and K. B. Winterbon, Nucl. Instr.and Meth. **119** (1974) 541.

[Tes95] J. R. Tesmer and M. Nastasi, Handbook of Modern Ion Beam Materials Analysis, MRS, Pittsburgh, USA (1995).

[Tho03] J. J. Thomson, Conduction of Electricity through Gases, Cambridge Univ. Press (1903).

[Zie85a] J. F. Ziegler, and J. M. Manoyan, Nucl. Inst. and Meth. **B35** (1988) 215.

[Zie85b] J. F. Ziegler, J. P. Biersack and Y. Littmark, The Stopping and Range of Ions in Solids, Pergamon Press, (1985).

[Zie88] J.F. Ziegler and Manoyan, J.M. Nucl. Instr. and Meth. **B35** (1988) 215.

CHAPTER 4 ANALYTICAL TECHNIQUES

This chapter discusses the main analysing techniques used in the study of silver diffusion and the production and annealing of radiation damage in 6H-single crystalline SiC. The main techniques used in this thesis are Rutherford backscattering spectrometry (RBS), RBS combined with channelling (RBS-C) and Scanning Electron Microscopy (SEM).

4.1 RUTHERFORD BACKSCATTERING SPECTROSCOPY - CHANNELLING (RBS-C)

In discussing these techniques we start by discussing the important parameters of the RBS and RBS-C techniques in section 4.1.1, followed by the details of the RBS technique in section 4.1.2; RBC-C is considered in section 4.2 and SEM in section 4.3.

4.1.1 ACCELERATOR, SCATTERING CHAMBER AND DETECTOR SYSTEM

RBS is a technique that is based on the analysis of the energy of the backscattered charged particles (helium ions (He^+) in our case) from the particular material of interest: for example in this thesis it is single crystal-6H silicon carbide with silver either deposited or implanted. The charged particles are generated by a RF-source and accelerated to high energies by applying a large potential difference across the accelerator tube. All this is done by a Van de Graaff accelerator which uses the principles discovered many years ago [Gra31]. This accelerator generates a high voltage using a moving insulating belt that carries charge which is sprayed on at the base plate and removed at the terminal. The work reported in this thesis was performed using the Van de Graaff accelerator at the University of Pretoria. The maximum voltage of this machine is 2.7 MeV but an energy of 1.6 MeV was used in this investigation. Schematic diagrams of the accelerator and the scattering chamber are reproduced in figure 4-1 (a) and (b).

The dipole magnet in front of the Van de Graaff accelerator deflects the beam into either beam line 1 or line 2. Hence, it acts as an energy and mass separator. Beam

line 1 has a chamber that is designed to operate below room temperature while line 2 functions at room temperature. For this study line 2 was used. A combination of vertical and horizontal slits in line 2 focuses and guides the beam into the chamber. The slits also help in producing a monochromatic beam consisting of one species, i.e. helium ions. The collimator inside the chamber (figure 4-1(b)) shapes the beam into a specific size before interacting with the sample. Thus the size of the beam is determined by the collimator's size. The sample is fixed on a stainless steel sample holder connected on a three axis goniometer system which has a precision of 0.02^{o} in each of the angle settings. The secondary electrons, which falsify the measurements, are suppressed by a negative voltage of 200 V connected to a ring shaped electrode in front of the target.

During analyses the beam is kept below 15 nA to avoid heating of the sample. This is also done to avoid a pile-up effect during the process of detecting backscattered particles. Pile-up occurs when the time response of the detector system is not fast enough to separate the individual events on the detector due to the high rate of encountered events. Therefore, in such a situation two events may end up being recorded as one event, which will falsify the measurements. The hydrocarbon deposition on the sample during analyses is minimised by keeping the pressure in the chamber at 10^{-4} Pa or below during the process. This carbon deposition is due to the collision of the analysing particles/beam with the residual gases and the subsequent decomposition of the gases. This occurs along the beam line but the carbon that is deposited on the sample's surface is that produced near the sample surface. The adsorption of water and carbon dioxide inside the chamber's surface is minimised by flooding the chamber with nitrogen gas during the opening of the chamber. This also helps in increasing the initial pumping rate.

The backscattered alpha particles represented by BS in figure 4-1(b) are detected by a Si surface barrier detector operating with a reverse bias of 40 V. The output charge signal (proportional to the energy of the backscattered particles) of the detector is fed into the pre-amplifier where it is integrated into a voltage signal that is proportional to the backscattered energy. This voltage signal is then amplified by the amplifier before it is digitized by an analogue to digital converter (ADC) inside the multi-channel analyzer (MCA) and stored in the computer connected to the MCA. The output of

MCA consists of counts vs. the channel number spectrum. The yield is the number of backscattered particles at 165° (for our experimental set-up) while the channel number is proportional to the backscattered energy. Using the computer, together with the RBS and RBS-C spectrum, the counts of backscattered ions as a function of channel number are monitored online and saved in the computer. The position of the sample is fixed but its orientation can be changed using the three axis goniometer with a digitized control unit that is controlled manually. Data acquisition is discussed in detail in section 5.5.

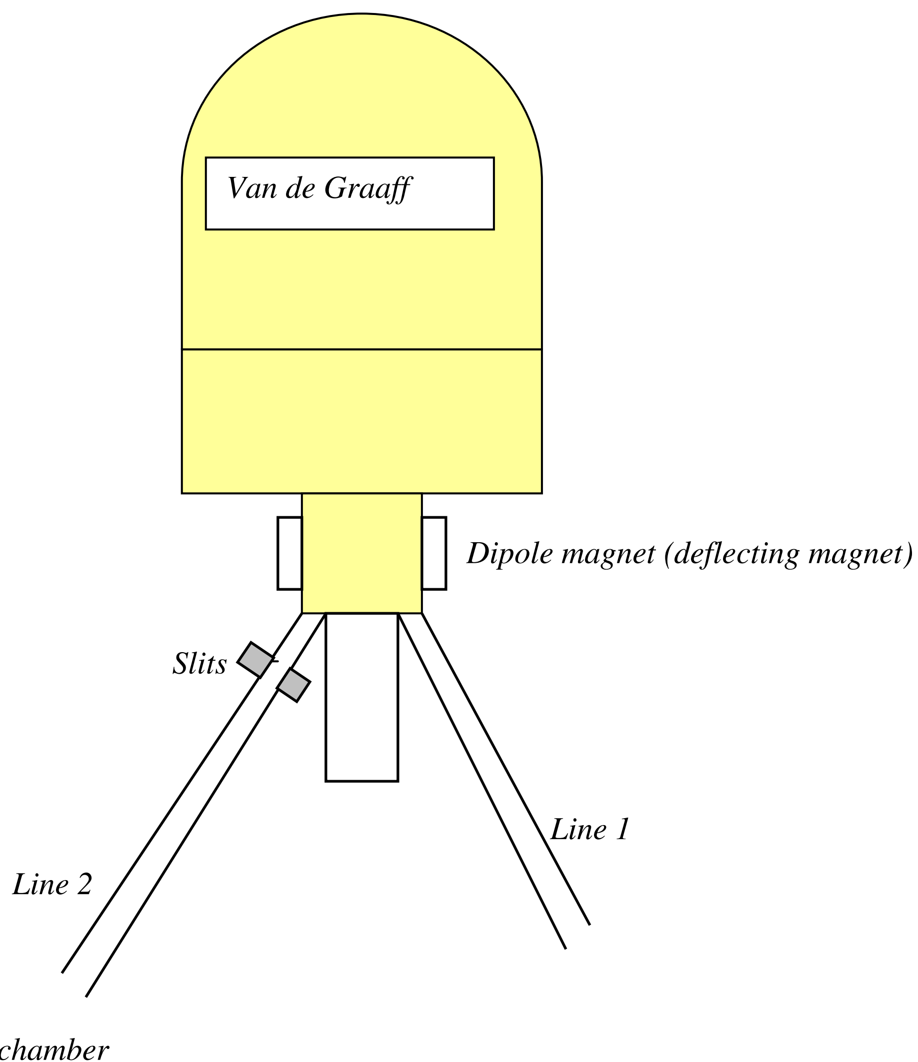

Figure 4-1 (a): A schematic diagram showing the Van de Graaff accelerator and beam lines of the University of Pretoria.

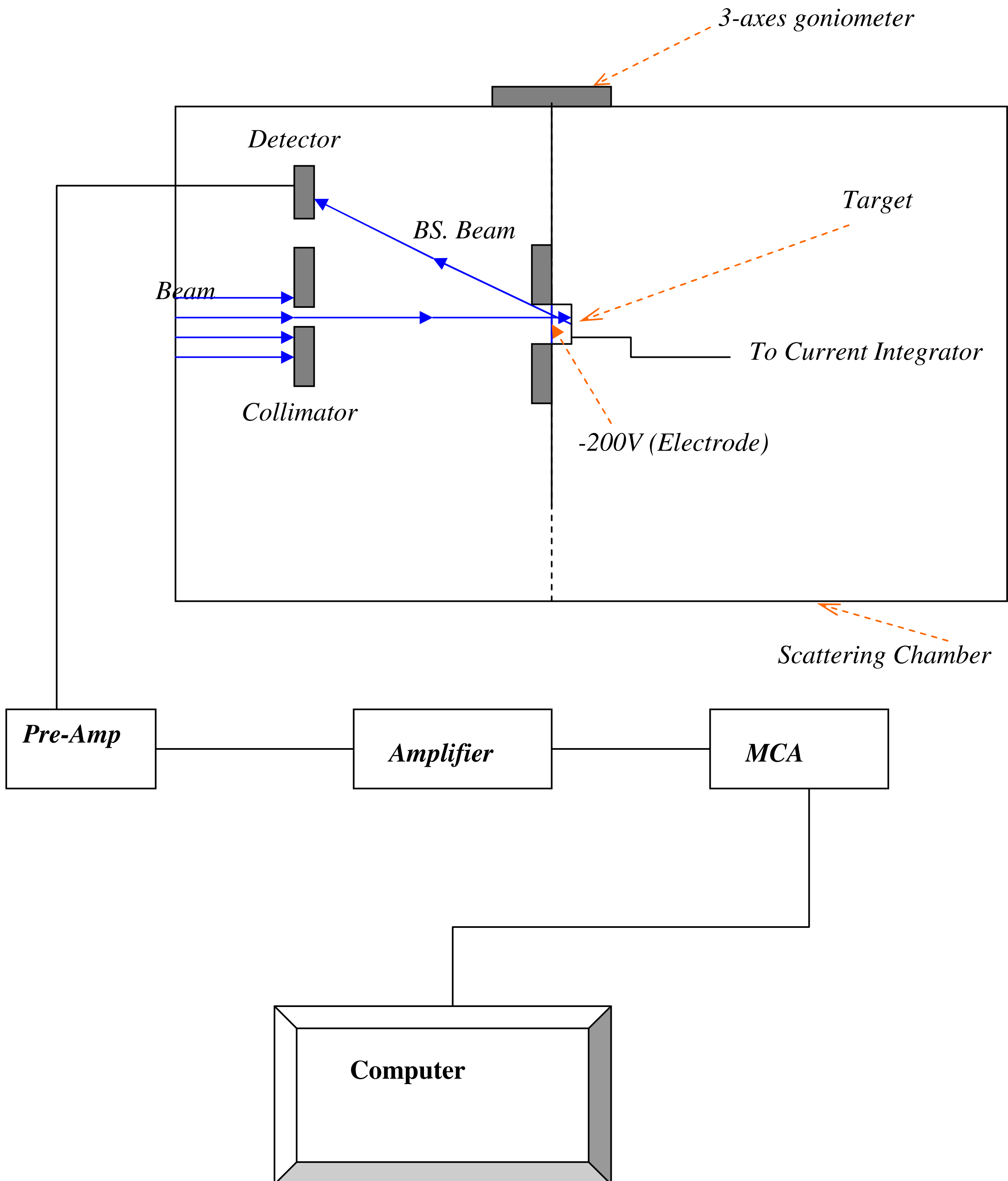

Figure 4-1(b): A schematic diagram showing the side view of the scattering chamber and detector system for the University of Pretoria's Van de Graaff accelerator.

4.1.2 DETAILS OF RUTHERFORD BACKSCATTERING SPECTROSCOPY

The non-destructive nature, simplicity, identification power, possibility of simultaneous multi element profiling and good depth resolution has caused RBS to dominate ion beam analysis in thin film science. Since this technique is based on the detection of backscattered alpha particles, the detector is placed at an angle greater than 90° but less than 180° with respect to the incoming beam – see Figure 4-2 for the definition of the angle. Therefore, only the backscattered alpha particles are detected. In this case the backscattered yield vs. channel number is measured. From the measured spectra the information about masses and the depth distribution of the target elements are extracted. This is only achieved if the kinematic factor, stopping power and scattering cross section of the ions are well understood. Therefore, all the above factors are discussed in this section together with some other factors that perturb the accuracy of RBS measurements.

4.1.3 KINEMATIC FACTOR

The setup of the RBS-C used in this thesis is illustrated in figure 4-2 below: In this setup the target is placed in such a way that the surface is facing the incoming α-beam and the detector is placed at the backscattered angle of 165° with respect to the incoming beam (see figure 4-2). For random RBS measurements the sample is oriented 5° off the channelled direction, as was discussed in section 4.2. The three angular parameters of the goniometer are digitized and not automated (see figure 4-1(b)). When the incoming beam collides with the target some of the target atoms recoil at angle ϕ (see figure 4.2) with respect to the incident beam.

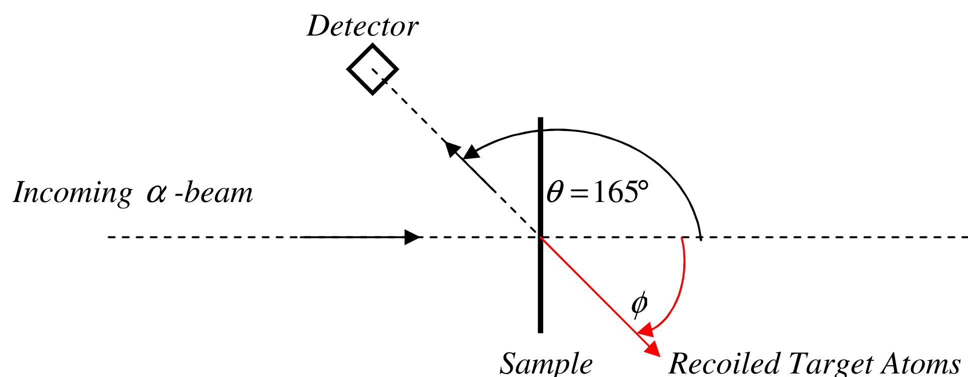

Figure 4-2: A schematic diagram showing the RBS experimental setup at the University of Pretoria.

If only elastic collisions are considered in such a setup, the energy of the backscattered α-particle (E_1) can be calculated using the conservation of energy and momentum [Chu78] [Tes95]:

$$E_1 = KE_0 = \left[\frac{M_1 \cos\theta \pm (M_2{}^2 - M_1{}^2 \sin^2\theta)^{1/2}}{M_1 + M_2} \right]^2 E_0 \qquad \ldots 4.1$$

where E_0 and E_1 is the energy of the incident and backscattered α-particles respectively, M_1 and M_2 are the masses of the analysing particle (α-particle) and the target atom, K is the kinematic factor (the ratio of the backscattered particle's energy to incident energy before scattering) and θ is the backscattering angle.

From equation 4.1 one can observe that E_1 can be calculated if the kinematic factor K is known. K can be calculated using M_1, M_2 and the scattering angle θ. At a fixed scattering angle the kinematic factor K depends only on the mass ratio i.e. M_1/M_2. The plus sign in equation 4 is only valid for the case where $M_1 < M_2$, while for $M_1 > M2$ there are two solutions, resulting in two kinematic factors K for backscattered α-particles at angle θ corresponding to different recoil angles ϕ [Chu78].

The RBS technique can be used to identify the sample components because the α-particles with the same incident energy and incident angle backscattered at different masses yield different energies according to equation 4.1. This difference in scattering energy for different masses influences the depth resolution, which is limited by a number of factors. These are: the energy resolution of the detector, the spread in energy of the α-particle, the solid angle of the detector, the beam size and the divergence of the accelerator beam. Good mass resolution is usually accomplished by using a projectile of higher mass but not larger than the target mass atom (because in the case where $M_1 > M_2$ the projectile will not backscatter) and measuring at a backscattering angle that is approximately 180°. In this study α-particles were used to minimise the energy straggling compared to other heavy atoms such as oxygen.

4.1.4 DEPTH PROFILING

The backscattered alpha particles also have different energies because they are backscattered from different depths. For example, figure 4-3 is a schematic diagram

depicting the backscattering events at the surface and at depth x. The alpha particle that backscatters at the surface possesses energy of KE_0 while the one that backscatters at depth x has an initial energy E lower than E_0 because it loses energy before backscattering at depth x. From figure 4-3, the length of the inward path where the ion loses energy is $x/\cos\theta_1$. As can be seen in figure 4-3 the ion has energy KE just after being backscattered at depth x. The ion that is backscattered at depth x continues to lose energy on its way out; with reference to figure 4-3 it is evident that the length of the outward path is $x/\cos\theta_2$.

In order to calculate the energy of the alpha particle that backscatters at depth x one needs to take into consideration the fact that it loses energy both on its way in and out. The expression of the alpha particle that backscattered at depth x was derived by assuming that the energy loss (dE/dx) is constant along the inward and outward paths [Chu78] [Tes95]:

$$KE_0 - E_1 = \left[\frac{K}{\cos\theta_1} \frac{dE}{dx}(in) + \frac{1}{\cos\theta_2} \frac{dE}{dx}(out) \right] x \qquad \ldots 4.2$$

where the 'in' and 'out' in brackets refer to the constant values of dE/dx along the inward and outward paths. KE_0 is the energy of the backscattered alpha particles at the surface atoms of the target, while E_1 is the energy of the alpha particle backscattered from the atom at depth x.

Now if one takes the difference between E_1 and kE_0 to be ΔE, i.e.

$$\Delta E = KE_0 - E_1 \qquad \ldots .4.3$$

Then equation 4.2 can be written as:

$$\Delta E = [S]x \qquad \ldots 4.4$$

where

$$[S] = \left[\frac{K}{\cos\theta_1} \frac{dE}{dx}(in) + \frac{1}{\cos\theta_2} \frac{dE}{dx}(out) \right] \qquad \ldots 4.5$$

[S] is called the energy loss factor that contains the relationship between energy and depth information. It also relates the energy width δE to depth resolution δx: $\delta x = \delta E/[S]$. Therefore, from measuring the energy which can be converted to depth as will be discussed in chapter 5, the backscattered spectrum of counts vs. energy can easily be converted into counts vs. depth.

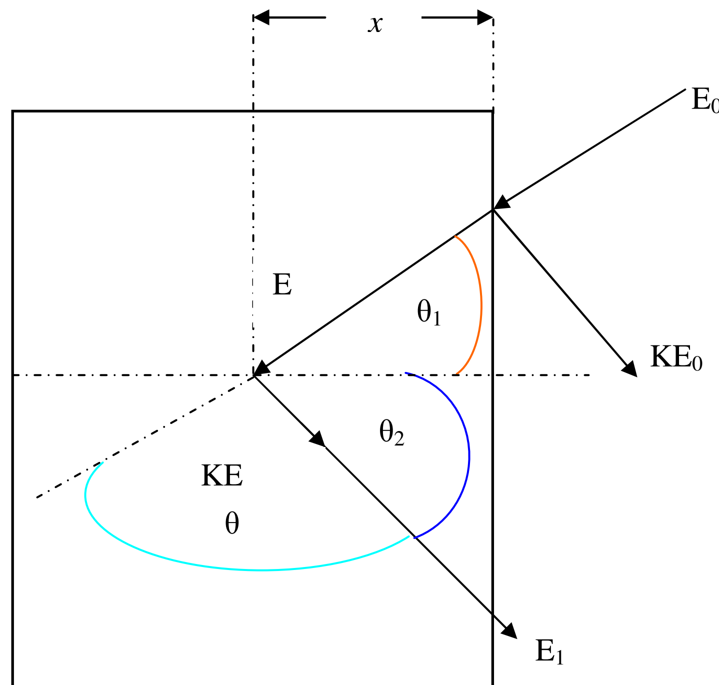

Figure 4-3: A schematic diagram showing the backscattering events in a target consisting of one element. The angles θ_1 and θ_2 are positive regardless of the side on which they lie with respect to the normal of the target.

4.1.5 DIFFERENTIAL CROSS SECTION

Up till now the backscattered α-particle has been discussed without asking: how often does this happen? In order for one to obtain an idea of how frequently this process occurs, the concept of a differential cross section must be introduced.

The probability for a backscattering event to take place is expressed in terms of the differential cross section for scattering, i.e. $d\sigma / d\Omega$ in a given direction into a solid angle $d\Omega$, and is defined as the number of particles scattered into this solid angle $d\Omega$ per number of incident particles per unit area. The differential cross section for the

scattering of a projectile into a solid angle $d\Omega$ centred around an angle θ in the laboratory frame of reference is given as [Chu78][Tes95]:

$$\frac{d\sigma}{d\Omega}=\left(\frac{Z_1Z_2e^2}{4E_0}\right)^2\frac{4(\sqrt{M_2{}^2-M_1{}^2\sin^2\theta}+M_2\cos\theta)^2}{M_2\sin^4\theta\sqrt{M_2{}^2-M_1{}^2\sin^2\theta}} \qquad \ldots 4.6$$

and the total number of detected particles can be written as:

$$A=\sigma\Omega QN \qquad \ldots 4.7$$

where E_0 is the energy of the projectile before scattering, Z_1 is the atomic number of the projectile with mass M_1, Z_2 is the atomic number of the target with mass M_2, e is the electronic charge, A is the number of backscattered and detected projectiles, Q is the total number of incident projectiles, N is the total number of target atoms per unit area, σ is the differential cross section and Ω is the solid angle of the detector. From equation 4.7 it is clear that when A, σ, Ω and Q are known N can be obtained, thus quantifying the results.

Since the differential cross section is proportional to Z_2^2 and inversely proportional to E_0^2 , it means RBS is more sensitive for the detection of elements with higher Z and one could therefore expect more backscattered count/yield if one is working with lower energy compared with higher energies.

4.2 RUTHERFORD BACKSCATTERING SPECTROSCOPY COMBINED WITH CHANNELLING (RBS-C)

RBS-C is a technique that is based on the analyses of the backscattering particles in the channelling direction explained in section 3-5. This is done by perfectly aligning the beam along the crystallographic direction of the sample using a three axis goniometer. Hence, in order to align the beam precisely, the structure of the material of interest needs to be understood. In this section, the structure of SiC is discussed before the RBS-C.

SiC is a binary compound with equal amounts of Si and C atoms. The fundamental structural unit of SiC is a covalently bonded primary co-ordinated elementary tetrahedron, either SiC_4 or CSi_4 [figure 4-4(a)]. These four bonds directed to the neighbours possess an almost pure covalent character, and from the difference in electronegativity between the silicon and the carbon atom, an ionic contribution to the bond of about 12% is estimated.

In a SiC crystal the tetrahedra are arranged in such a way that all atoms lie in parallel planes on the nodes of regular hexagonal networks. The most remarkable characteristic of the crystal structure of SiC is polytypism (which is due to one-dimensional disorder, allowing many structures with different stacking sequences). The difference between various polytypes is the stacking order of elementary tetrahedra [Wes96]. There are two stacking sequences: if the projections of silicon atoms in three successive layers are in different positions A (circles), B (squares) and C (triangles), the cubic structure is formed (figure 4-4(b)); while if the projection of atoms in the third silicon layer coincides with the position A of the first silicon atoms in the first layer (figure 4-4(c)), the hexagonal structure is formed. The SiC crystals appear in a number of modifications that display either hexagonal or trigonal symmetry. They can all be described in the usual hexagonal axis system, with one ***c***-axis perpendicular to three equivalent axes *a*, *b*, and *d* at angles of 120^0 with one another. The axes and the base of the hexagonal unit cell are indicated in figure 4-4(b). Figure 4-4(b) and figure 4-4(c) illustrate that $(11\bar{2}0)$ planes give a correct representation of the SiC structure because all relevant atoms lie in these planes and the right hand figures in figure 4-4 demonstrate such representations for the cubic (zincblend) and hexagonal (wurtzite). The positions of silicon atoms in $(11\bar{2}0)$ planes for most common polytypes of SiC are depicted in figure 4-5. The bold horizontal lines mark the completion of a unit cell on the c-axis. The zinc blend structure requires three steps in the same direction, leading to the stacking sequence ABCABC, known as 3C according to the nomenclature of Ramsdell [Ram47]. A unit cell of the wurtzite lattice is built up by a sequence of one step to the right and one to the left, leading to the stacking sequence of ABAB (figure 4-5(b)), and is called 2H.

All other polytypes can be characterized in this way as shown in figures 4-5(c) and 4-5(d) for 4H and 6H respectively. Figure 4-5(e) portrays the most common modification with a rhombohedral unit cell 15R.

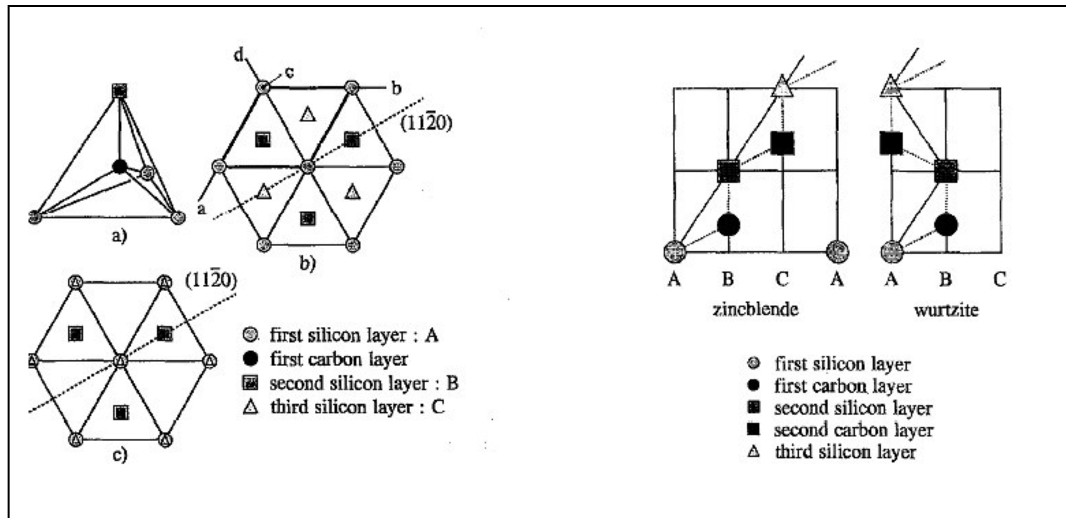

Figure 4-4: Elementary SiC-tetrahedron (a) and projections of different positions of silicon atoms in the zincblende structure; the unlabelled diagrams on the right hand side indicate the position of silicon and carbon atoms in (11 $\bar{2}$ 0) planes of the cubic (zincblende) and hexagonal (wurtzite) structures [Wes96].

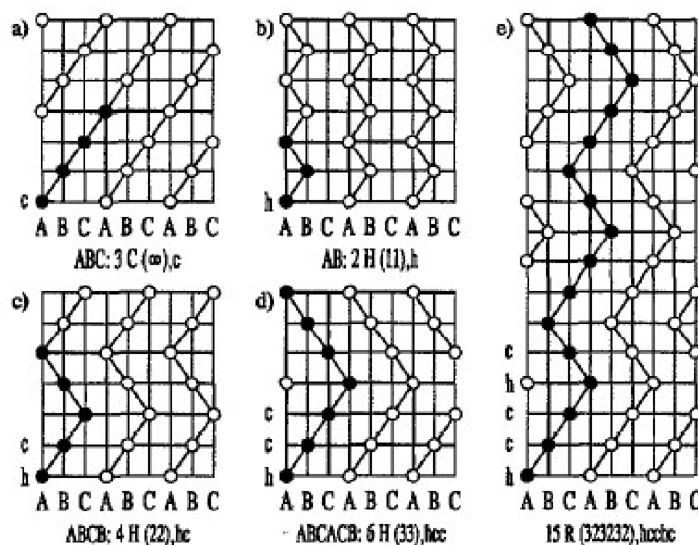

Figure 4-5: Position of silicon atoms in (11 $\bar{2}$ 0) planes of different polytypes [Wes96].

Another form of nomenclature counts the steps necessary to complete one unit cell (the number of steps to the right, then to the left etc. until the unit cell is completed) as

with Zhadanov [Zha45], indicated in figure 4-5 (in brackets). Still other nomenclatures characterize the sequence of layers by cubic (c) or hexagonal (h) environment, as does Jagodzinsky [Jag49]. Different nomenclatures are discussed in [Izh00] [Pag90]. The cubic polytypes are known as β–SiC, and all non-cubic structures (hexagonal and rhombohedra) are called α–SiC. More than 250 polytypes are known to exist.

The RBS-C measurements required a major channel in a crystal, i.e. in 6H-SiC in our case. In the process of finding this channel, the c-axis is taken as the reference. Hence the major channel is searched with reference to the c-axis. In this study, the channel was searched by scanning the sample around a vertical axis perpendicular to the c-axis and around a horizontal axis perpendicular to the c-axis in steps of 0.2^{o}. This scanning was carried out between the Si and C edges to avoid the surface backscattering. This was achieved by setting the backscattering energy window between the Si and C edges using the single channel analyser (SCA) discussed in section 5.5. The yield/counts as a function of these angles on both axes are recorded. The minimum backscattered yields as a function of the angles are then plotted on graph paper. This minimum yield represents the crystallographic planes. The angular scan is then reduced until the directions of planes are determined by plotting the minimum yield as a function of the angles. The crossing point of planes indicates the position of the axis or the channel. After obtaining the channel the energy window is maximized to allow the collection of the full spectrum (in our case the spectrum of SiC with a silver implant).

In this study RBS-C is used to study damage retained in 6H-SiC after implantation and after annealing. The random spectrum is taken 5° off the channel and the target is continuously rotated about the incident c-axis to avoid channelling in the sample. A rough method of estimating an idea of how much damage was present in the sample was devised by comparing the ratio of the aligned spectrum yield/counts of the treated sample to its random spectrum. In this method, if the ratio of the aligned spectrum yield of the treated samples to the random spectrum is equal to 1, it may mean either amorphous or highly disordered or polycrystalline re-growth. The data acquisition of

RBS and RBS-C measurements is described in chapter 5 while results are presented and discussed in chapter 7.

4.3 SCANNING ELECTRON MICROSCOPY (SEM)

A scanning electron microscope (SEM) is a microscope that uses electrons rather than light to form an image of objects on a very fine scale. This kind of microscopy has a long history. The first SEM was built around 1938, with the first commercial instrument being made available around 1965. The electrons are produced in the electron gun by the electron beam source. The function of the electron gun is to provide a stable electron beam of adjustable energy. Older SEMs use tungsten or LaB_6 thermionic emitters while some of the new SEMs are equipped with cold, thermal or Schottky field emission sources. A field emission cathode is usually a wire shaped into a sharp tip (100 nm or less radius) supported by a tungsten hairpin. When the field at the tip reaches a magnitude of about 10V/nm, electrons are emitted. A cathode current density as high as 10^5 A/cm^2 may be obtained from a field emitter as compared with 3 A/cm^2 from a thermionic source [Gol03].

A cold field emitter (CFE) relies purely on the high applied field to cause the emission of electrons. Cold field emitters require an ultrahigh vacuum to ensure that the cathode surface is atomically clean. The tip is flushed clean by heating for a few seconds at about 2500K before the operation. This flushing shortens the lifetime of the emitter. The advantage of the CFE is the virtual probe of 3-5 nm that requires little demagnification to obtain a 1 nm diameter probe. A thermal field emitter (TFE) possesses the same properties as a CFE, but it is operated at elevated temperature. This helps to keep the tip clean, reducing noise and instability even in degraded vacuum conditions. In the Schottky field emitter (SFE) the work function is reduced by a ZrO_2 film deposited on the flattened tip from a small dispenser. An ultrahigh vacuum aids long-term stability, prevents poisoning of the ZrO_2 cathode and maximizes brightness.

The stability of an electron gun is a measure of how constant the electron emission is per unit time. The most stable sources are Schottky field emitters with a beam current stability of about 1%/h.

The electron beam energy spread is the spread in energies of electrons leaving the filament. For a tungsten hairpin gun it is 3 eV, for LaB_6 1.5 eV while it is 0.3-0.7 eV for field emitters. The electron beam is guided into the aperture by magnetic lenses. The aperture determines the current in the final probe of the sample. The probe is scanned across the sample, and the signal produced is detected and amplified before being displayed on the monitor.

Before we discuss this process in detail, we first need to understand the electron material interactions. Figure 4-6 depicts the particles that are produced when the electrons interact with the sample while figure 4-7 illustrates the different depth regimes of the emitted particles. These regimes can overlap for some of the rays; e.g. X-rays also originate from the surface regions. A backscattered electron (e^-) is the result of an elastic collision between an incoming electron and the nucleus of the target atom. The elements with higher atomic numbers produce more backscattered electrons. These electrons usually possess higher energies compared to the energies of the secondary electrons. The detected signal of the former electrons is used for contrast between areas with different chemical compositions, i.e. it is made use of to look at the atomic number contrast and topographical contrast. For example, in the image formed by these electrons, silver will appear brighter than Si and C of SiC because of higher Z. Backscattered electrons can also be used to form an electron backscatter diffraction (EBSD) image, which can be utilised to determine the crystallographic structure of the sample [Cha86].

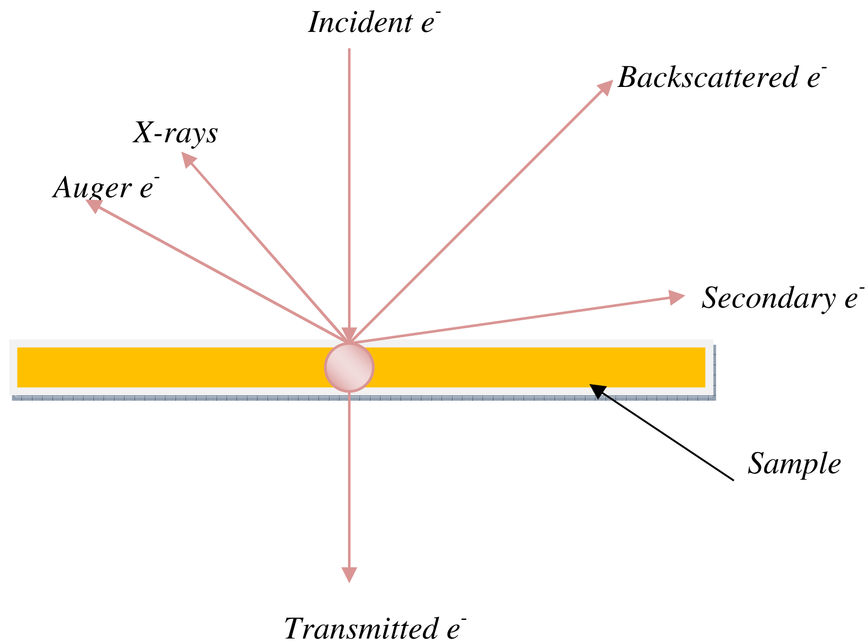

Figure 4-6: A schematic diagram showing what rays are emitted when an energetic electron (e^-) strikes the sample.

Secondary electrons are the results of the inelastic collisions between the incident electrons and the electrons of the target atoms. These electrons possess energy less than 50 eV [Gol03]. Their signal is used to study the surface topography of the sample. These electrons are generated along the incident electrons' trajectory but only those generated a few nano-meters underneath the sample surface are detected – the others are absorbed in the sample owing to their low energy.

Auger electrons are the results of outer shell electrons (higher energy level) filling inner shell holes (lower energy level) created by the excitation primary electron. The excess energy available may be carried away through the emission of low energy electrons (Auger electrons) or the production of X-rays. The signals that result from these Auger electrons can be used for chemical analysis of the sample surface. The X-ray signals can also be utilised for chemical characterization of the samples, i.e. for identifying the type and the concentration of the elements in the sample. The latter technique is called energy dispersive x-rays spectroscopy (EDS).

The volume at which all the discussed interactions occur in the sample depends on the following three factors: Atomic number of the material that is being analysed since a higher atomic number sample absorbs or stops more electrons and causes a smaller interaction volume. Electron energy: higher energy electrons penetrate further into the sample and generate a larger interaction volume. The angle of incidence for the electron beam: the greater the angle (further from normal), the smaller the interaction volume. By detecting the necessary signals, SEM is able to provide information on the following:

(i) Topography, which identifies the features of the surface of an object or sample.

(ii) Morphology, which furnishes information on the shape and the size of the particles making up the sample.

(iii) Composition, in other words the elements and compounds that the sample is composed of and the relative amounts of them (this is possible in some SEMs).

(iv) Crystallographic information, which shows how the atoms are arranged in the sample.

In this study, a Zeiss Ultra 55 field emission scanning electron microscope which uses SFE was used. This machine employs a field emission electron gun. The Zeiss Ultra 55 is equipped with SE (secondary electron) detectors, BE (backscattered electron) detectors and an in-lens SE detector. The last mentioned is a detector which is highly surface sensitive; its efficiency improves as the acceleration voltage drops lower. For most of our studies the in-lens SE detector was used to study the surface before and after annealing. The results are discussed in chapter 7.

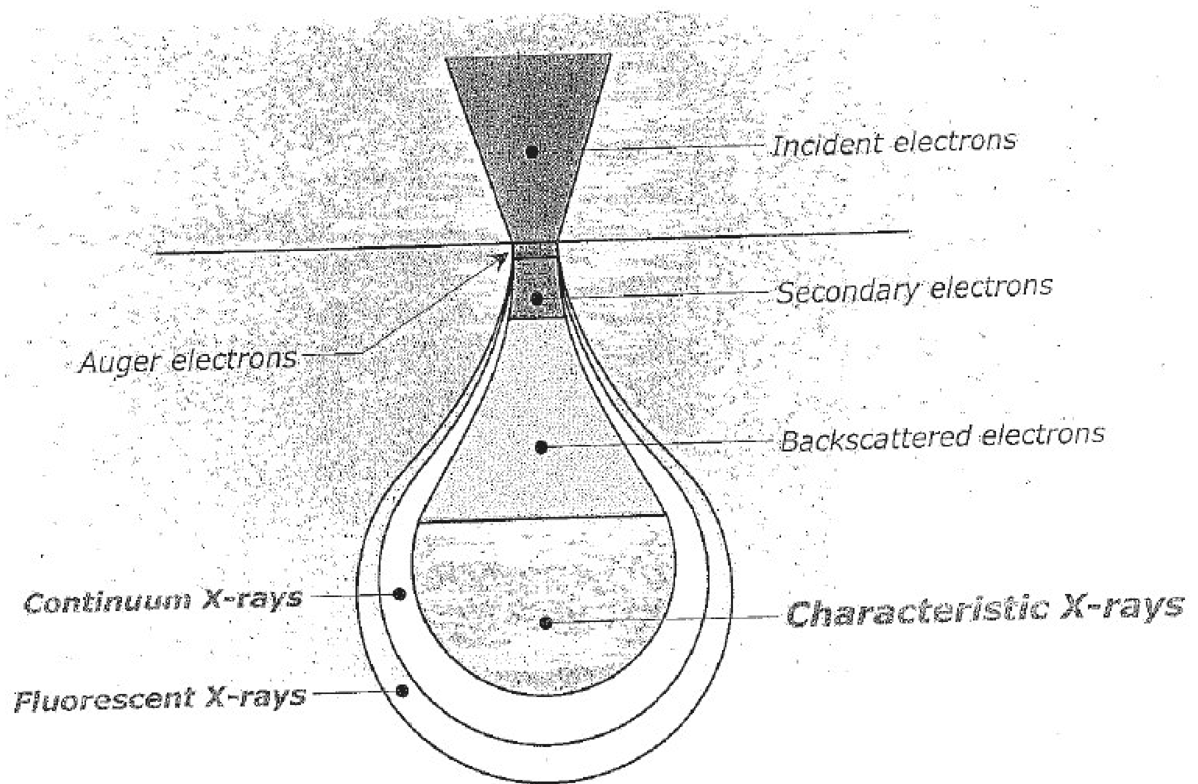

Figure 4-7: A schematic diagram showing that the particles emitted during electron-sample interaction are emitted at different depths [wwwi].

4.4 REFERENCES

[Cha86] S.K. Chapman, Working with an Electron Microscope, Lodge-marks Press (1986).

[Chu78] W. K. Chu, J. W. Mayer and M. A. Nicolet, Backscattering Spectrometry, Academic Press, New York (1978).

[Gär05] K. Gärtner, Nucl. Instr. and Meth. **B227** (2005) 522.

[Gär97] K. Gärtner, K. Hehl, G. Schlotzhauer, Nucl. Instr. and Meth. **B4** (1984) 55 und 63; K. Gärtner Nucl. Instr. and Meth. **B132** (1997) 147.

[Gol03] J. Goldstein, D. Newbury, D. Joy, C. Lyman, P. Echlin, E. Lifshin, L. Sawyer and J. Michael, Scanning Electron Microscopy and X-Ray Microanalysis, 3rd edition, Springer, USA (2003).

[Gra31] R. J. van de Graaff, Phys. Rev. **38** (1931) 1919.

[Izh00] V. A. Izhevskyi, L. A. Genova, J. C. Bressiani, A. H. A. Bressiani, Cerâmica vol.46 n.297, São Paulo Jan./Feb./Mar. 2000.

[Jag49] H. Jagodzinski, Acta Crystallog., **2** (1949) 201-207.

[Pag90] T. F. Page, The Physics and Chemistry of Carbides, Nitrides and Borides. Edited by R. Freer, Kluwer Acad. Publishers, Netherlands, (1990) 197.

[Ram47] R. S. Ramsdell, Am. Min., **32** (1947) 64.

[Tes95] J. R. Tesmer and M. Nastasi, Handbook of Modern Ion Beam Materials Analysis, MRS., Pittsburgh (1995).

[Wes96] W. Wesch, Nucl. Instr. and Meth. **B116** (1996) 305.

[www1] http://www.jeol.com,12, November, 2010.

[Zha45] G. R. Zhadanov, Compte Rende Acad. Sci. URSS, **48** (1945) 39.

CHAPTER 5 EXPERIMENTAL PROCEDURE

The in-diffusion behaviour of silver together with the production, annealing of radiation damage and diffusion behaviour of implanted silver in single crystalline 6H-SiC have been investigated, using RBS, RBS-C and SEM, from temperatures below the melting point of silver (960 ^{o}C) up to 1600 ^{o}C. This chapter discusses all the experimental details of this investigation.

5.1 SAMPLE PREPARATION

The starting materials for this study were single crystalline 6H-SiC wafers from Intrinsic Semiconductor in Dallas VA/USA, with a diameter of 50.8 mm, thickness of 368±25 μm and micropipes area density < 30 cm^{-2}. Before deposition or implantation the wafers were cut into halves using a diamond scriber. For silver deposition experiments, the halves were further cut into 5×5 mm^2 samples with a rotary diamond saw before being cleaned in an ultrasonic bath using acetone (10 min), trichloroethylene (10 min), 10% hydrochloric (HCl) acid (10 min) and 10% dilute hydrofluoric (HF) acid (10 min) successively, with rinsing by de-ionised water after each step. Finally the water was blown away using nitrogen gas. The cleaning procedure was employed to remove any contamination together with the natural oxide layer on the surface, which might have had negative effects on the experiment. The size of the samples was chosen to suit the RBS-C and SEM analyses experiments. For the deposition of silver (100 nm), the cleaned samples were mounted on a steel holder (which holds eight samples), then transferred into a vacuum. This was done to ensure that they were prepared under the same conditions. The deposition of silver of 100 nm thickness is discussed in section 5.2. After deposition some of the samples were encapsulated in a quartz ampoule together with a silver source to maintain a silver layer on the samples' surfaces and then annealed. The silver source was included to maintain a silver layer on these surfaces during annealing.

The other halves of the samples were cleaned four times in an ultrasonic bath with acetone (10 min) followed by de-ionised water rinsing at the end of the four cleaning steps and then sent for implantation. This procedure was followed to remove

contamination on the surfaces that was introduced during the cutting process. The oxygen layer on the surface does not affect implantation so negatively because the implants are inside the samples. After implantation, discussed in section 5.3, the samples were also cut into 5×5 mm^2 samples and cleaned with acetone for RBS-C, SEM and annealing experiments. Figure 5-1 depicts the typical processes of sample preparation.

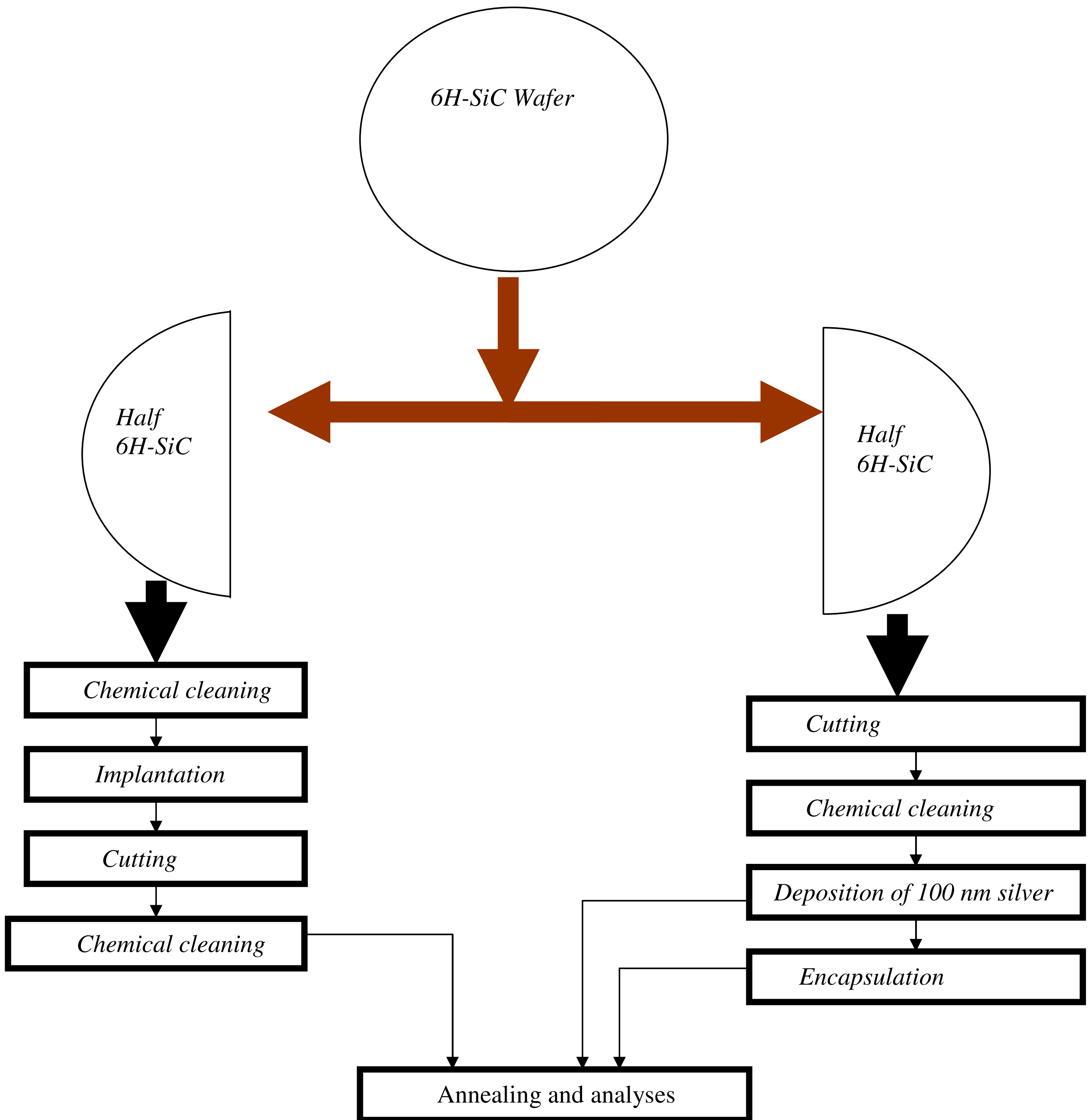

Figure 5-1: A diagram showing the typical process of sample preparation.

5.2 DEPOSITION

A thin silver film of 100 nm thickness was deposited on some 6H-SiC substrates mounted on the steel holder (capable of holding eight 5×5 mm^2 samples) using a resistive evaporation technique. This was performed under a vacuum of about 10^{-4} *Pa*. In this system, the substrates were placed in a high-vacuum chamber with a

molybdenum crucible containing the silver to be deposited, a shielding plate located between the crucible and substrates and a water cooled film thickness monitor (see figure 5-2).

For the deposition of silver, a current of about 4A was applied through the molybdenum crucible until it heated up beyond the boiling point of silver, thereby causing the latter to evaporate and condense on all the exposed cooled surfaces on the vacuum chamber. The deposition is only performed on the side facing the crucible as seen in figure 5-2, which illustrates the deposition process that is taking place in the vacuum chamber. After deposition some of the samples, together with a silver source, were vacuum-encapsulated to about 10^{-6} mbar with a quartz glass ampoule and then annealed. The silver source was included in the ampoule so that the silver vapour equilibrium was reached in a very short time, thus maintaining the silver layer on top of the samples.

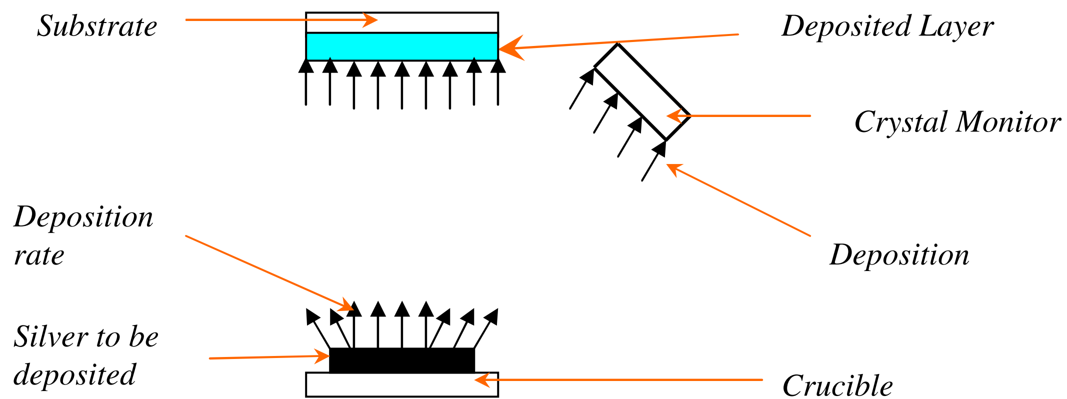

Figure 5-2: A schematic representation of the Ag deposition process in a vacuum chamber. The shielding plate is not shown.

5.3 IMPLANTATIONS

All the implantations for this thesis were performed in the Institut für Festkörperphysik, Friedrich-Schiller-Universität, Jena, Germany. The silver ions ($^{109}Ag^{+}$) were implanted at an energy of 360 keV with a fluence of 2×10^{16} cm^{-2} for all the samples.

For the study of radiation damage and its influence on silver diffusion, silver was implanted at different temperatures, i.e. room temperature, 350 ^{o}C and 600 ^{o}C. To avoid the channelling of silver ions during implantation in single crystalline silicon carbide (6H-SiC), samples were tilted 7° with respect to the normal incidence. All the implantations were performed at an average vacuum of 10^{-4} Pa. The flux was always kept below 10^{13} cm^{-2}s^{-1} to prevent beam induced target heating.

5.4 ANNEALING SYSTEMS

Two annealing systems were used in this study. For the in-diffusion experiments, the samples were vacuum annealed in a tube oven with a maximum temperature of 1000 ^{o}C. This maximum temperature is reached in the centre of the oven and slightly decreases towards the sides of the oven. A thermocouple with feedback to the control system regulates the temperature of the oven with an accuracy of ±5 ^{o}C. For the in-diffusion studies two experiments discussed in section 5.1 and 5.2 were performed: vacuum-encapsulated samples and un-encapsulated samples annealed in vacuum. For annealing, the samples were placed on a quartz glass supporting rod centred on the axis of a quartz tube attached to a turbo pump vacuum system. The quartz tube was then evacuated to about 10^{-6} mbar. The temperature of the sample was measured with a thermocouple near the sample. Before annealing was performed, the oven was allowed to stabilize at the preset temperature before shifting it to a position where the sample was centred in the middle of the oven for annealing. At the end of the annealing time, the oven was shifted back and the sample was then allowed to cool down to room temperature before samples were taken out for analyses. All the in-diffusion studies were conducted in this oven.

Implanted samples were annealed in vacuum using a computer controlled Webb 77 graphite furnace either for 10 hours (annealing cycles up to 80 hours or 30 minute annealing cycles up to 120 minutes), from 700 ^{o}C, a temperature below the melting point (962 ^{o}C) of silver, to 1600 ^{o}C. Three types of experiments were performed in this study: isochronal, sequential and isothermal annealing. During isochronal annealing different samples were subjected to different annealing

temperatures for the same time or annealing cycle while during isothermal annealing the samples were annealed at the same temperature, and the annealing time was incremented after analyzing the sample as *10h-analyses+10h = 20 hours-analyses+ 20 hours = 40 hours-analyses.* A similar procedure was followed with respect to isothermal annealing for 30 minute cycles. For sequential annealing experiments, samples were first annealed at a lower temperature, followed by analyses, and then taken to the next higher temperature, followed by analyses. The difference between sequential annealing and isochronal annealing is that in the former the time is not the same as in isochronal annealing. This was repeated until the highest temperature was reached.

The temperature is controlled by an Eurotherm 2704 controller connected to a thermocouple and a pyrometer. The temperature is measured by the thermocouple below 1475 °C and by the pyrometer above 1525°C. An average value of the thermocouple and pyrometer values is used between these temperatures. The temperature accuracy is ±15°C.

The silver implanted samples were sandwiched between two poly-crystalline silicon carbide slabs (see figure 5-3) and placed in a graphite crucible before annealing. This process was carried out to avoid contamination of the samples with any contaminants in the oven during annealing and to minimize the thermal etching of SiC in the sample of interest during annealing. Then the graphite crucible was put inside the oven. The system was subsequently evacuated to a pressure in the 10^{-6} mbar range and then degassed at 100 ^{o}C for 3 hours, annealed at the required temperature and time, finally being cooled down to room temperature - see figure 5-4. The aim of the degassing procedure was to ensure that the maximum pressure during annealing was in the 10^{-5} mbar range and to reduce the pumping time to attain a pressure lower than 5×10^{-6} mbar before annealing.

UNIVERSITEIT VAN PRETORIA
UNIVERSITY OF PRETORIA
YUNIBESITHI YA PRETORIA

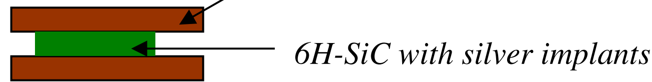

Figure 5-3: Diagram showing 6H-SiC with silver implants sandwiched between poly-silicon carbide.

A typical heating curve is depicted in figure 5-4 for a sample annealed at 1300 ^{o}C for 10 hours. Figure 5-4 portrays the time dependent relationships between (i), temperature and vacuum pressure (ii), vacuum pressure and heating current and (iii), cooling rates (^{o}C/min) and temperature during the degassing, heating up, annealing and cooling down processes. In figure 5-4, the repeated labels indicate the same process occurring.

If the heating element is switched on, a large current of 40A (G in figure 5-4(ii)) is used before the regulating process is started. After regulation, the current drops to 22A. The high heating rate (due to the large current) causes an initial high degassing rate of the heating element and nearby isolation material which results in an increase in the vacuum pressure from 10^{-6} mbar to about 10^{-5} mbar (J in figure 5-4). During this period the thermocouple in the oven is still at room temperature. During the heating up process, the pressure increases nearly linearly as a function of time to a maximum value of about 10^{-5} mbar at the start of the annealing dwell (E and C in the figure 5-4 (i)) while simultaneously the heating current increases (M in the figure 5-4(ii)) to about 40 A. This ensures a 20 °C/min heating rate. During the annealing dwell (C and D) the heating current stabilises at 22A while the pressure decreases to a minimum value of 10^{-6} mbar at the end of the dwell. This means that the pumping rate is larger than the degassing rate. The behaviour is identical during the degassing process - see A, B, J, E and F in figure 5-4(i). At the end of the annealing time, the heating current is switched off, causing a sharp drop in the vacuum pressure. The initial cooling rate is -19°C/min. In approximately 60 min the cooling rate increases to -4 °C/min (figure 5-4 (iii)). The duration of the heating ramp is 10 h and the heating rate is 20 °C/min; consequently the thermal stresses in the sample are greater during heating than during cooling. The system is allowed to cool down to a temperature below 100 °C and then flooded with argon gas, followed by vacuum pumping to increase the cooling rate until the temperature is below 40 °C

(where the samples are removed). Heat losses from the system occur by means of radiation and conduction in the isolation material and the container.

From the radiation law, the cooling of our oven is given by $T(t) = F\exp(-Zt)$.The cooling rate can be found by taking the derivative of the decrease in temperature with respect to time: $\frac{dT}{dt} = -FZ\exp(-Zt)$, where F and Z are constants and t is time. The values of F and Z were obtained by fitting the data of the cooling curve of temperature (^{o}C) versus time (h) as shown in figure 5-5 and were found to be 3.09×10^{6} ^{o}C and 2.79×10^{-1} h^{-1} respectively. The difference between the data and the fitted exponential curve is due to the fact that heat is not only lost via radiation and conduction as explained above. Figure 5-6 depicts the cooling curve for a sample annealed at 1300 ^{o}C for 10 hours compared to that for samples annealed at 1300 ^{o}C for 30 minutes. For a shorter annealing time, the cooling rate is very fast because the heat is not distributed to all parts of the oven, making cooling more rapid than that after a longer annealing time.

Figure 5-4: The typical heating curve as the function of time compared with pressure, current, heating and cooling rate during degassing (2h-10h), heating up (17h-30h), annealing (20h-30h) and cooling down (30h-40h).

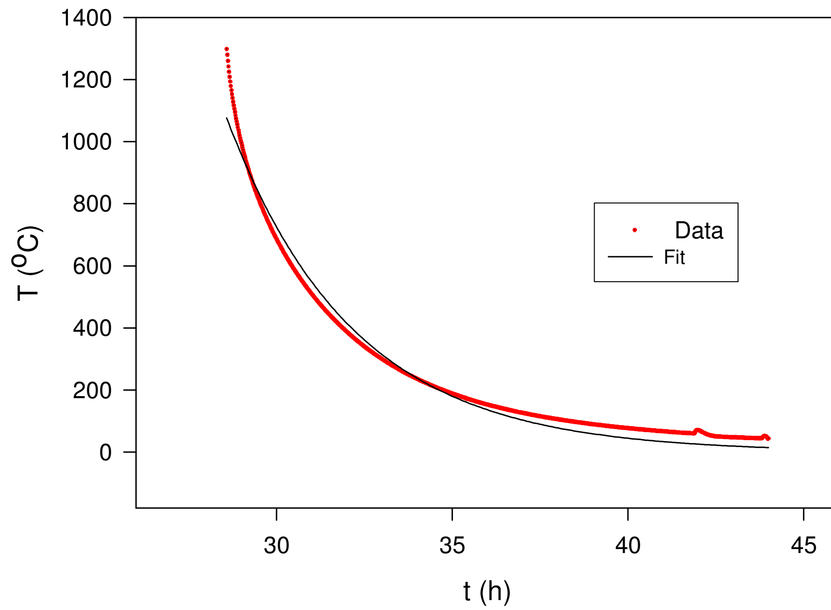

Figure 5-5: The cooling curve of the Webb oven as fitted to an exponential function to obtain constants.

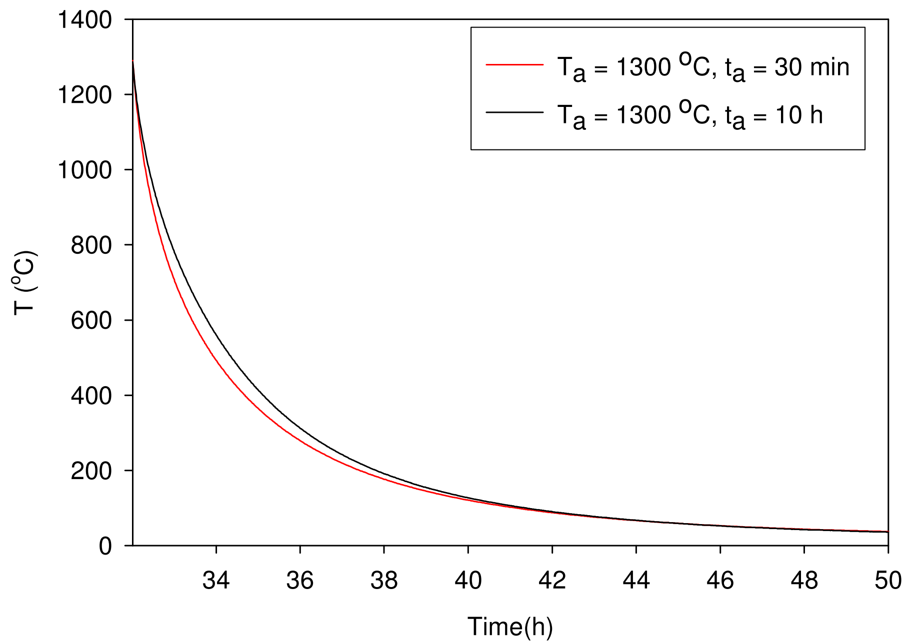

Figure 5-6: The cooling curve for a sample annealed at 1300 °C for 10 h compared to the cooling curve for a sample annealed at 1300 °C for 30 minutes.

5.5 DATA ACQUISITION

The block diagram of the apparatus used in the detection, amplification and collection of backscattered alpha particles is depicted in figure 5-7. These particles are detected by a Si-surface barrier detector. The signal produced was first amplified by the pre-amplifier Canberra 220 before being fed into the main amplifier, a Tennelec TC 243. This Si-surface barrier detector requires a biased voltage of 40 V.

The bipolar (bi) output signal from the amplifier is fed into the digital oscilloscope for beam monitoring purposes while the unipolar (Uni) signal is fed into the multi-channel analyzer (MCA). On the other hand, the current collected at the back of the target is fed into the current integrator, an Ortec 439, where it is digitized. The logic signal from the current integrator is sent into a charge counter where its output is fed to the MCA and the counter. The logic signal from this current orders the MCA when to start processing the unipolar signal from the amplifier and when to stop. It also instructs the counter when to start counting and when to stop doing so.

Inside the MCA there is a single channel analyser (SCA). This selects the energy window by adjusting the lower and the upper energy discriminators on the SCA. This is done to allow only the signals with the energies within the energy window to be further processed. The logic output from the SCA (inside MCA) is fed into charge counter and is used in RBS-C for channel direction searching, as explained in section 4.2. Finally the output of the MCA is fed into the computer where it is accessible while being collected. The MCA output consists of backscattered counts (or yield) vs. channel numbers. The channel numbers have a linear relationship with the backscattered energy of particles.

Backscattered α-beam

I (current)

Si-Surface Barrier Detector

40 V

Pre-Amp Canberra 220

Ortec 439 Current Integrator

Amplifier Tennelec TC 243

Bi-polar

Charge Counter

Counter

Oscilloscope

Uni-polar

Start/stop

MCA Multiport II Canberra

PC

Figure 5-7: Block diagram of the electronic circuit for RBS and RBS-C measurements.

5.6 DATA ANALYSES

Counts versus channel number were obtained by collecting a total charge of 8 μC per run for 10 runs per sample under investigation: the average of the runs was used for further analyses of the data. This process was carried out in order to reduce the statistical error. All the spectra were stored in the computer connected to the MCA before they were taken for further analyses. The energy calibration required for depth profile analyses was calculated from the RBS spectrum of glassy carbon with a 10 nm layer of silver on top using 1.6 MeV α-particles.

The energy calibration in keV/channel was converted into a depth calibration nm/channel using a computer program, STOP2 [Fri06], which makes use of the energy loss data in Ziegler [Zie77]. Assuming no loss of silver, the counts were converted into relative atomic density (%) by first calculating the silver density inside SiC. This was achieved by taking into consideration the implanted fluence (ϕ) in cm^{-2} unit, the total silver counts (N) in *counts* unit, count per channel (dn) in *counts* unit and the depth resolution (D) in *cm/channel* unit:

$$\rho_{Ag} = \frac{\phi dn}{ND} \text{(Ag-atoms/cm}^3\text{)} \qquad \ldots 5.1$$

Thereafter the relative atomic density (RAD) % was determined by taking the ratio:

$$RAD(\%) = \frac{\rho_{Ag}}{\rho_{SiC}} \times 100 \qquad \ldots 5.2$$

Where ρ_{Sic} is the atomic density of SiC in cm^{-3}. For this study the density of 6H-SiC was taken to be 3.21 $g.cm^{-3}$, equivalent to 9.641×10^{22} $atoms/cm^3$.

The spectra of RAD % versus depth or of counts versus depth were then fitted to an Edgeworth distribution using the Genplot fitting function program [www2] to obtain the first four moments of the silver distribution function i.e. projected range/mean depth (Rp), straggling/standard deviation (σ), skewness (γ), and kurtosis (β). These

are mathematically written as follows:

$$R_p = \frac{\sum_i x_i}{N},\ \sigma = \left[\frac{\sum_i x_i - R_p}{N}\right]^{\frac{1}{2}},\ \gamma = \frac{\sum_i (x_i - R_p)^3}{N\sigma^3} \text{ and } \beta = \frac{\sum_i (x_i - R_p)^4}{N\sigma^4}$$

where x_i is the distance from the surface to the implanted ions and N is the number of implanted ions. For a normal distribution or Gaussian distribution $\gamma = 0$ and $\beta = 3$. The Edgeworth distribution is shown below:

$$f(x) = g(x)p(x) \qquad \text{....5.3}$$

Where

$$g(x) = \frac{h}{\sqrt{2\pi}}\exp(\frac{-\arg(x)}{2})$$

and

$$p(x) = 1 + \frac{\gamma\arg(x)^3 - 3\arg(x)}{6} + \frac{(\beta-3)(\arg(x)^4 - 6\arg(x)^2 + 3)}{24},$$

with

$$\arg(x) = \frac{(x - R_p)}{\sigma}$$

and where h is the height fitting parameter.

Skewness characterizes the degree of asymmetry of a distribution. Positive skewness indicates a distribution with an asymmetric tail extending towards more positive values, while negative skewness indicates a distribution with an asymmetric tail extending towards more negative values. Our profiles show a positive skewness, indicating that our distributions are skewed towards the more positive value. Kurtosis measures how peaked or flat the distribution is with respect to the Gaussian function. The full width at half the maximum of the silver peak is given by: $FWHM = 2\sigma\sqrt{2\ln 2}$.

For our diffusion analyses the FWHMs of the depth profiles of the annealed samples were compared with the FWHMs of the as-implanted profiles. The depth profiles of SiC were calculated using the Si depth resolution from STOP2. The relative disorder was estimated by taking the ratio of the aligned/channelled spectrum to the random spectrum. The retained silver was calculated by working out the ratio of total silver

(as-implanted silver) to the total silver left behind (normalized to the as-implanted RBS spectrum).

5.7 ERROR ANALYSES

The errors for measurements given in this study were calculated from several uncertainties: statistical uncertainty σ_s, which was minimized by collecting a charge of 8 μC, the uncertainty from genplot, σ_g, 1% uncertainty of the analyzing beam energy, σ_b and 1% uncertainty of the scattering angle, σ_a. The total error was then calculated by summing the squares of the functions of these errors and taking the square root: $\sigma_t = \sqrt{f^2(\sigma_s) + f^2(\sigma_s) + f^2(\sigma_g) + f^2(\sigma^2)}$.

5.8 REFERENCES

[Zie77] J.F. Ziegler, The Stopping and Ranges of Ions in Matter, Pergamon Press, New York (1977).

[Fri06] E. Friedland, STOP2, Private communication, Department of Physics, University of Pretoria, 2006.

[www2] hhttp://www.genplot.com, 4 November 2009.

[www1] http://www.canbera.com/products/genie2000, 4 November 2009.

CHAPTER 6 REVIEW OF PREVIOUS RESULTS

Since the detection of silver in the primary circuit of the test reactors i.e. the Dragon Reactor in the United Kingdom, the Jülich Arbeitsgemeinschaft Versuchsreaktor (AVR) in Germany and the Peach Bottom in the United States, many studies have been carried out on the possible migration paths of FPs through the coating layers, especially SiC (which is the main barrier of fission products). Most of the previously reported investigations have been performed using the batch and individual inventory methods. Only a few have been carried out utilising the implantation and diffusion couple methods, which are the methods used in this thesis. However to obtain the full picture of the migration of silver in SiC one needs to understand the previous results on silver migration investigated by all the methods and all the assumptions made in arriving at their results.

In the batch method, large populations of either loose fuel particles or those in the fuel element are heated together and the total amounts of released FPs are measured. From the released FPs the diffusion coefficients are calculated using analytical and numerical solutions for diffusion and release from spherical shells. All the calculations are performed by assuming that the particles in the batch behave exactly the same. In the individual inventory experiments the FPs of each fuel particle are measured before and after annealing using gamma counting. The FPs release measurements on the batches of fuel elements which provide useful information on the overall performance, but these do not furnish enough information on the performance of the individual particle. Individual particle measurements provide a more detailed image of fission transport. This type of measurement is time consuming because more time is required to count each particle. For example, counting times up to 8h are required to obtain reliable counting statistics. The demand on resources limits the number of particles that can be individually counted to evaluate the release of fission products. Therefore, small populations of particles, sometimes just 10 to 25, are investigated and assumed to be representing much larger batches.

In ion implantation, the ion of interest (silver in this study) is implanted into one of the coating layers of interest (SiC in this study) and its migration is investigated by comparing the ion's depth profiles before and after treatment.

The majority of the previous results indicate that the migration path of silver is diffusion in SiC; however the reported diffusion coefficients differ by many orders of magnitude. The ion implantation method has just been described while in the diffusion couple method the substance of interest (silver in our case) is coated on the substrate; then annealed. The annealed couple is thereafter analysed for any in-diffusion. In this chapter some results of the previous studies are discussed according to their investigation methods.

6.1 BATCH MEASUREMENTS

In this section the previous results gathered from the batch method are discussed and their diffusion results are summarised in table 1.

Nabielek et al. annealed TRISO particles that were irradiated in a reactor (with neutrons) at 1500 ^{o}C: the total FPs released were measured every 10 days up to 210 days [Nab77]. The results after annealing indicated that the release of silver began after 10 days of annealing, with cesium and strontium still being retained. The silver release curve as a function of annealing time was plotted: its shape contradicted that of the silver diffusion in SiC. At the beginning of the annealing, the release of silver was equivalent to a diffusion coefficient of about 10^{-16} m^2s^{-1}, and as the annealing continued the silver release curve was equivalent to a diffusion coefficient of about 10^{-15} m^2s^{-1}. From these results Nabielek et al. concluded that the silicon carbide layer was slowly becoming transparent to silver as the annealing time lengthened, allowing an increase in the silver released. Therefore, the proposed physical mechanism for this change in the SiC properties during annealing indicated that silver migration did not entirely take place by a diffusion mechanism.

In another investigation, Nabielek et al. [Nab77] performed post irradiation annealing between 1140 ^{o}C and 1240 ^{o}C for both shorter and longer annealing times. A noticeable increase in the release of silver was observed. From these results it was

suggested that SiC was only an effective barrier below 1200 ^{o}C, and no diffusion coefficient was calculated by the authors [Nab77].

The FPs' release behaviour in BISO (this is a particle similar to the TRISO particle explained in chapter 1 although SiC is not its coating layer) and TRISO particles were investigated by Brown et al. [Bro76]. In this investigation both BISO and TRISO particles were annealed at 1500 ^{o}C and the FPs released were measured. The results indicated instant release of silver in BISO particles while, in the TRISO particles the release of silver began after 16 days of annealing. From the results the diffusion coefficient of silver in silicon carbide was calculated:

$$D_{SiC} (1500\ ^{o}C) = 1.5\times10^{-16}\ m^{2}s^{-1} \qquad \text{....6.1}$$

Amian et al. [Ami83] investigated the FPs release behaviour from the TRISO particles which were previously irradiated with fast neutrons fluences from< 0.5×10^{25} m^{-2} to 8.2×10^{25} m^{-2} at temperatures ranging from < 400 ^{o}C to <1055 ^{o}C: the burnup values for these particles ranged between 2.3% and 12.1% FIMA. In this investigation different particle types of fuel kernel materials with only slight variations in coating dimensions were used. Before the post irradiation, isothermal annealing at temperatures between 1000 ^{o}C and 1500 ^{o}C under vacuum was performed, and the FPs content of each particle was measured. After annealing was completed the particles' FPs were measured. By combining all the results a diffusion equation for silver in silicon carbide was derived [Ami83]:

$$D_{SiC} = 4.5\times10^{-9} \exp\ [-218\text{kJ mol}^{-1}/(RT)]\ m^{2}s^{-1} \qquad \text{....6.2}$$

The diffusion coefficients from different batch tests carried out by Amian et al. scattered over more than one order of magnitude at any annealing temperature. The large scatters in the diffusion coefficient data were suggested as resulting from the variations in the silicon carbide microstructure, which differ from coating to coating. Within the range of the burnup and fast fluence of the tested fuels, the dependence of silver diffusion on those variables within the scatter of data has not been found. From the experiments performed and the calculated diffusion coefficients, the authors concluded that the grain boundary diffusion was responsible for silver diffusion in

polycrystalline SiC, not the volume of diffusion through grains. Therefore, the scatter in the data was understood to be also the result of grain boundary diffusion, since such diffusion depends on the microstructure of the sample, which varies from sample to sample and from manufacturer to manufacturer.

Table 1: Pre-exponential factors and activation energies and diffusion coefficients of silver in silicon carbide (SiC) from different authors.

Type of Particle	Temperature (^oC)	$D_0(m^2s^{-1})$	E_a ($kJmol^{-1}$)	Diffusion Coefficient or Diffusion Equation (m^2s^{-1})	Source
TRISO	1500			10^{-16} and 10^{-15}	[Nab77]
TRISO	1140, 1240				[Nab77]
BISO and TRISO	1500			1.5×10^{-16}	[Bro76]
TRISO	1000:1500	4.5×10^{-9}	217.7	$D = 4.5\times10^{-9}\exp\left(\frac{-218kJ}{RT}\right)$	[Ami83]
TRISO	1200,1350 and 1500				[Bul84]
TRISO	1600 :1800				[Sch91]
TRISO	1400			8.0×10^{-17} to 2.0×10^{-16} and $9.9\times10^{-17}$to 7.3×10^{-17}	[For82]
TRISO	1600:1900				[Min93]

Bullock [Bul84] measured the release of silver and other FPs at 1200 ^oC, 1350 ^oC and 1500 ^oC. This was carried out by isothermal annealing (at these three temperatures) the previously irradiated TRISO particles (five different types, at 900 ^oC, to burnups in excess of 20% FIMA). The five TRISO particles investigated were undergoing three changes in the fuel kernel material and two changes in the coatings. The five

coated particle fuels were: UO_2; UC_2; UCO; and a mixture of UO_2 and UC_2; denoted as UC_2; UO_2 with solid ZrC over-coating on the kernel denoted as UO_2*(1); and UO_2 with ZrC dispersed in the buffer layer surrounding the kernel, denoted as UO_2*(2). The FPs released were measured up to an annealing time of about 10,000 hours [Bul84]. The results of this test revealed the strong temperature dependence of the breakthrough times, i.e. as the temperature increased, the fission product breakthrough times decreased dramatically. These breakthrough times also appeared to depend on the type of fuel particle tested. UO_2*(1) particles did not release any FPs during the annealing test while all the other types released silver with breakthrough times from about 30 h to 8,000 h. This long delay time before the release of silver was explained by the fact that no silver escaped during irradiation. This was based on the fact that, if silver had escaped during this process it would have been distributed throughout the particle and if that had been the case, silver escape during annealing would have occurred sooner than observed. No diffusion coefficient was calculated by the author.

Schenk et al. performed post-irradiation annealing of spherical fuel elements containing 16,400 fuel particles per element at temperatures between 1600°C and 1800 ^{o}C. The content of FPs before and after annealing was measured [Sch90]. The results indicated that the fuel elements released a greater fraction of their original silver than any other fission product. This high quantity of silver release was said to be indicating the mobility of silver in SiC and no diffusion coefficient was calculated from these results. The fractional release values were derived by comparing the total amount of silver released during annealing with the measured inventory before annealing and were found to become greater with higher annealing temperature [Sch90]. Since measurements of silver release from the collection of coated fuel particles inside an element do not provide any insight into the mechanism controlling silver transport through SiC, the diffusion coefficients were not calculated from the silver release data. Through calculating equivalent failures (broken SiC) from the fractional release values, it was found that a mechanism resulting in a complete silver loss could produce the same results regarding the release of silver. Hence no diffusion coefficient was calculated.

In another attempt at understanding the migration path of silver in SiC, Förthmann et al. measured the fractional release of silver from UO_2 TRISO-coated fuel particles.

This was performed during post-irradiation annealing of these particles at 1400 ^{o}C. In these investigations Förthmann et al. focused on the relationship between the calculated diffusion coefficients and SiC coating parameters. The said parameters, such as density, grain size, microstructure, and light reflectivity, indicated no clear relationship with the silver released. However, a range of diffusion coefficients corresponding to the range of deposition temperatures and carrier gas used during SiC deposition was reported [For82].

Förthmann et al. also annealed seven types of previously irradiated fuels, compressed with matrix graphite at 1400 ^{o}C, over different annealing times. The results indicated the unprompted release of silver. Its curve provided a steady contribution of silver before the general breakthrough of this FP. This was thought to be due to uranium contaminating the outside of the silicon carbide layer. This suggestion was based on the fact that silver produced outside the SiC layer would be released almost immediately, compared to that produced inside the SiC. In the SiC deposited in pure hydrogen, the diffusion coefficient increased with the deposition temperature from 8.0×10^{-17} m^2s^{-1} to 2.0×10^{-16} m^2s^{-1}, with deposition temperatures ranging from 1300 ^{o}C to 1550 ^{o}C [For82]. What was also observed was that the SiC microstructure consisted of a striated structure with free silicon when the deposition temperature was 1300 ^{o}C, a crystalline structure with small crystalline size when this temperature was 1400 ^{o}C, and large columnar crystals when the deposition temperature was 1500 ^{o}C.

The results reported by Förthmann et al. indicated no significant influence of the presence of free silicon in the SiC deposited at 1300 ^{o}C on silver diffusion as suggested by Nabielek et al. [Nab77]. In the SiC deposited in pure hydrogen, the silver diffusion coefficient appeared to increase as the SiC became more columnar. However, the total change in the diffusion coefficients on SiC deposition temperature was much smaller than the range observed in the literature. Hence a definite trend was not confirmed. What was also found from these results is that the residual stress within the SiC coatings was different for different SiC grain structures and that this may play a role in the performance of SiC as the main barrier to solid FPs.

The results of SiC deposited in a mixture of argon and hydrogen indicated a decrease in diffusion coefficient from 9.9×10^{-17} m^2s^{-1} to 7.3×10^{-17} m^2s^{-1} as the deposition

temperature increased from 1300 °C to 1550 °C. In this type of deposition, the SiC deposited at 1300 °C consisted of a crystalline structure with small crystallite sizes, of small and uniformly distributed crystallite when the deposition temperature was 1400 °C and of coarse-grained but not columnar grains when this temperature was 1500 °C. The results of Förthmann et al. identified no relationship between microstructure and silver release [For82]. From the results, the authors found that the trend of diffusion coefficient was changing with respect to deposition temperature, especially for SiC deposited in pure hydrogen. The values of diffusion coefficients reported in these study [For82] were all within the range of diffusion coefficients reported by other authors. The small variations of these results relative to the literature suggested that the microstructure associated with the change in SiC deposition was not the primary contributor to silver transport in SiC.

Minato et al. conducted a post-irradiation annealing of TRISO particles in the temperature range 1600 °C to 1900 °C [Min93]. The burnups of the fuels were 3.6 % FIMA, which corresponded to the designed maximum burnup in the HTTR. The two samples A and B were irradiated at different average temperatures, i.e. 1250 °C and 1510 °C respectively. The results of these tests revealed no pressure vessel failure, no palladium attack or thermal decomposition of SiC. It was, however, found that ^{137}Cs, ^{134}Cs, ^{110m}Ag, ^{154}Eu and ^{155}Eu were released from the coated particles through the coating layers during post irradiation annealing. The diffusion coefficient of ^{137}Cs was calculated from the release curves based on the diffusion model, assuming a one layer coated fuel particle [Min93]. No silver diffusion coefficient was calculated from the fractional release but the measurements of fractional release suggested that the diffusion coefficient of ^{110m}Ag in SiC was larger than that of ^{137}Cs, which agreed with most results found in the literature.

In summary, the previous published batch results have suggested that silver migrates via diffusion through intact silicon carbide layers in the coated fuel particles. This suggestion has been justified by the fact that silver was released from the coated fuel particles while the volatile fission gases and cesium were retained. This suggestion has also been motivated by the results of coating failures, i.e. where both the pyrolytic carbon layers and the SiC layer have failed and the kernel is exposed. During coating failure cesium and silver escape from the fuel particles at typical operating

temperature. Therefore, all the published results have been interpreted as representing the diffusion-controlled release of silver through intact silicon carbide layers. Moreover, the calculated activation energies for diffusion coefficients in SiC fall in the same range as the activation energies for grain boundary diffusion of other fission products [Ami83]. Thus the current interpretation of silver migration indicates that silver diffuses along grain boundaries in intact silicon carbide at typical operating temperatures. However, the variations in the reported diffusion coefficients are not consistent with grain boundary diffusion and other observations, which has raised doubts about diffusion as the dominant mode of silver transport.

6.2 INDIVIDUAL INVENTORY MEASUREMENTS

In this section previous results on individual inventory measurements are discussed Nabielek et al. also measured the individual silver content of particles. The particles investigated appeared intact and retained all their cesium and other FPs but considerable changes in silver content were observed [Nab77]. The variation in silver release data was resulting from the availability and accessibility of free silicon on the SiC grain boundaries, which enhanced silver diffusion.

Bullock conducted a post isothermal annealing at temperatures of 1200 ^{o}C, 1350 ^{o}C and 1500 ^{o}C on coated particles with different fuels as discussed in section 6.1 [Bul84]. Ten particles from each of the five irradiated fuels were randomly selected for post isothermal annealing. From the selected particles, the individual contents of silver, cesium, europium and cerium were measured before and after annealing. These individual fission product inventories were then normalized to the ^{106}Ru inventory (a chemically stable fission product in the fuel particle) before annealing. The calculations of inventories were also performed after annealing. The results indicated close agreement between the experimental and theoretical values for ^{134}Cs and ^{137}Cs inventories. This indicated that cesium was not released during irradiation. However, about 25% less silver, 15% cerium and 25% more europium than predicted were found. The highly nonuniform release of silver per particle was also noted. The majority of the annealed particles released more than 50% of their original silver while one particle retained all of its original silver [Bul84]. Cesium was mostly retained, with about three particles from the two batches losing their entire original

silver. This behaviour, i.e. from completely retained silver to complete release did not agree with diffusion as the transport mechanism. If diffusion had been the transport mechanism, identical particles in the same test would have produced similar results. For example, at 1500 ^{o}C it was found that some particles retained their entire silver inventory, while others experienced total release of silver. This indicated that SiC was still a useful barrier up to 1500 ^{o}C.

The UO_2 particles that experienced the greatest silver release consisted of columnar, large-grained SiC. The UO_2*(1) particles that retained all silver and other FPs comprised laminar structured SiC but the ZrC coating on the fuel kernel may also have assisted the retention. The UCO particles also comprised laminar SiC and good silver retention. However, the UC_2 particles also consisted of laminar SiC timely released silver. This indicated that laminar SiC was not the only reason for silver retention. The results also demonstrated that silver breakthrough times increase significantly as the annealing temperature decreases. Measurements of the FPs before the annealing provided the total amount of the silver in each particle at the beginning of each test, but the exact location or distribution of this silver was not known. Silver not already released from the fuel kernel into the coating layers must diffuse through the kernel and coatings before it reaches the SiC. The particles irradiated under the same conditions should indicate the same location and distribution of silver. However the lack of knowledge of the initial location made it impossible to determine the contribution of the retention of silver because of the delay in the fuel kernel and the SiC layer. Bullock [Bul84] also found that SiC microstructures within a given batch of fuel particles were similar after etching but that silver release differed from particle to particle within a batch. Hence, the variations in microstructure may have contributed to the silver released between batches but did not by themselves explain the large variations in silver release within the batches. These variations were considered to be due to short-circuit paths or cracks in the SiC layers.

Pearson et al. [Pea80] [Pea82] performed a test on the interaction of silver in UO_2 TRISO-coated particles having 3.3 wt% of silver, which is 100 times more than the silver expected during the normal operation of medium-enriched UO_2 to 20% FIMA. This was done to ensure that silver was detectable after annealing, while taking into consideration the loss from the kernel during the coating process. In this test silver

was mixed with UO_2 during the manufacture of the fuel kernel before coating (standard TRISO coating). The silver-doped fuel particles were annealed on a graphite wafer in three different ranges of temperature: 1550 to 1900; 1400 to 1750 and 1250 to 1500 ^{o}C for 25; 260 and 3528 h respectively. After annealing the particles were mounted and then polished to the midplane. SEM identified several locations of silver interaction with the SiC in many of the particles, which was inconsistent with the diffusion process. On the colder side of the particle, silver was found along the PyC-SiC interface [Pea80].

Pearson et al. [Pea82] also investigated silver interaction with SiC in TRISO particles with 1.26 wt% silver mixed with UO_2 fuel kernel at the maximum temperature of 1500 ^{o}C. SEM results indicated no silver penetrating SiC but extensive swelling in the SiC was reported [Pea82]. TEM results after annealing for 2000 h indicated no microstructural changes either on the hot or the cold side of the particles, and also no second-phase nodules and no grain boundary films [Pea80]. Due to the lack of measurements of particle silver inventories, the release of silver was not mentioned. Hence, from the results, it was not clear whether silver was released or not.

Minato et al. performed a test on the particles that were deconsolidated from irradiated fuel elements [Min98] [Min00]. The fission product inventory of the individual particles before and after annealing was measured. The results of gamma measurements after irradiation indicated that gamma rays from ^{95}Zr, ^{106}Ru, ^{134}Cs, ^{137}Cs and ^{144}Ce were dominant. Using the activity ratios of mobile FPs (such as silver and cesium) to chemically stable FPs (such as ruthenium and zirconium), the comparisons between the fuel particles inventories were made while accounting for individual variations in fuel kernel size and burnup. In this investigation, during an accident condition test (ACT), solid FPs released from the particles were collected regularly and counted. The amount of ^{85}Kr release was monitored as an indication of through-coating particle failure during heating. In the first accident condition (ACT-1), 100 particles were annealed at 1600 ^{o}C for 73.6 h. This test was initially planned to run for 1000 h but it was stopped, owing to the high rate of particle failures and contamination caused by the release of FPs. The amount of ^{85}Kr indicated four through-coating particle failures during annealing at 1600 ^{o}C for 5h, 28 h, 44 h and 50 h [Min98] [Min00]. It was also found that five particles lost significant cesium during

annealing, while a total of about 22 particles lost part of their OPyC layer and three of the five particles that lost significant cesium also lost part of their OPyC layer or experienced cracks in their OPyC layers. Silver release was investigated on six particles (out of 100 particles); the results indicated that two out of six lost more silver than cesium. The fission product release curves evaluated from seven measurements during annealing revealed similar shapes for both silver and cesium, which indicated that silver and cesium were released within 5-20 h. Although this suggested that silver and cesium were released at the same time, most likely from the same particles, the long gap between deposition cup readings left uncertainty about the individual behaviour of silver and cesium.

Two other accident condition tests, i.e. ACT-3 and ACT-4, were conducted. Their aim was to measure the diffusion of silver through intact SiC layers. In these investigations, each test was limited to 25 particles to accommodate long counting times, i.e. 8 h, to measure silver inventories. During annealing the particle identities were maintained so that the fission product inventories measured could be compared before and after annealing. In ACT-3 25 particles were annealed at 1800 ^{o}C for 270 h. No significant fission gas release was detected during annealing by the gas monitoring system, which indicated no through-coating failure during this test. However, the total inventory measurements of the 25 particles before and after annealing indicated that the particles lost an average of about 47% of their silver compared to about 7% of their cesium.

In ACT-4 25 particles were annealed at 1800 ^{o}C for 222 h. The results also indicated the considerable variation in the retention of the fission products. The 25 particles released more silver than cesium, i.e. about 69% of their silver was lost compared to 16% of their cesium. Based to these results the authors concluded that silver diffuses faster than cesium in SiC. However, the variation in the fractional release was noted among 25 particles in ACT-3 and ACT-4, which raised a question as to whether diffusion was the silver transport mechanism [Min98] [Min00].

6.3 ION IMPLANTATION

Batch measurements and individual inventory measurements discussed in section 6.2 and section 6.3 do not furnish extensive information about the behaviour of FPs in each coating layer. In ion implantation, an ion of interest (silver in this study) is implanted into one of the coating layer of interest (SiC in this study) and its migration is investigated by comparing the ion's depth profiles before and after treatment. The treatment may be the annealing of the sample or irradiation of the sample after implanting. This method provides additional information on the behaviour of FPs in a specific coating layer. However, implantation creates a great deal of damage depending on the implantation temperature, which influences the migration behaviour of the fission products. This section discusses the previous diffusion results of silver implanted in SiC.

In addition to the study of total silver release from fuel particles, the migration of implanted silver into CVD-SiC has been studied by various researchers. Nabielek et al. [Nab77] investigated the migration of silver implanted in a silicon carbide disk. The silver was implanted with a peak concentration equivalent to a relative atomic percent of 1.8 % ^{109}Ag into SiC, positioned at about 80 nm underneath the SiC surface. After annealing the sample at 1180 ^{o}C for 30 minutes, it was reported that the mobility of silver was too small to be detectable [Nab77]. The SiC contained some pores and had a density of 3.18 gcm^{-3}, within the range of typically characterized SiC and close to the theoretical SiC density (3.21 gcm^{-3}). The implanted silver concentration was in the range of typical concentrations reached at 12% FIMA. Nabielek et al. suggested that the silver was trapped inside the SiC grains; hence the lack of migration was due to the extremely low silver diffusion rate within these grains. From the small movement of atoms in the ion implantation experiment, the upper limit for the diffusion coefficient of silver in SiC at 1180 ^{o}C was calculated:

$$D_{SiC}\ (1180\ ^{o}C) \ll 10^{-19}\ m^2s^{-1} \qquad \ldots 6.7$$

This value is much lower, approximately more than two orders of magnitude lower, than the other diffusion coefficients for silver in SiC reported in the literature.

MacLean et al. investigated the migration of implanted silver with energies between 93 MeV and 161 MeV (which correspond to silver's projected range of 9 µm and 12µm respectively) on a flat plate of SiC 0.3 cm thick. The SiC plate were chemically vapour deposited (CVD) by the Coorstek company: the reported density was 3.21 gcm^{-3} with grain sizes of the order of 3-10 µm, preferably oriented in a direction perpendicular to the SiC surface. XRD (X-ray diffraction) analyses on a polished SiC sample confirmed that the Coorsek CVD SiC contained crystalline β-SiC with a strong preferred orientation so that the (111) planes were parallel to the surface and long, dendritic SiC grains, perpendicular to the surface, were evident in AEM analyses [Mac04].

In order to encourage diffusion, the implanted samples were annealed at 1500 °C for longer times, i.e. between 200 h and 500 h, in a vacuum, using a Webb graphite furnace. The annealing conditions for selected samples are shown in table 2. Before and after annealing the samples were analysed using XPS to measure the silver concentration profile, and SEM and AEM to investigate silver distribution within SiC. The XPS results indicated no measurable change in the silver concentration profiles after annealing, while the SEM and AEM results showed that silver was forming precipitates after annealing. AEM analyses indicated that silver was residing in amorphous SiC after implantation and that the silver precipitates were located between recrystallized SiC grains after annealing. Therefore, the SEM and AEM results indicated that silver did not migrate out of its original deposition zone.

From these results MacLean et al. calculated the upper limit of the silver diffusion coefficient in SiC:

$$D_{SiC}\,(1500\ ^{o}C) = 5\times10^{-21}\ m^{2}s^{-1} \qquad \ldots6.8$$

which is a value that is of about 6 orders of magnitude smaller than the other values reported in the literature, even though the annealing had been performed at a higher temperature for a longer time.

Table 2. Annealing conditions of some of the samples studied by MacLean et al. [Mac04].

Sample ID	Implanted fluence(atoms/cm^2)	Temperature (°C)	Time(h)	Analysis techniques
2b	1.9×10^{21}	1500±15	210±0.25	XPS profiles
5a	2.1×10^{21}	1500±15	480±0.25	AEM
6a	2.6×10^{21}	N/A	N/A	AEM

Jiang et al. implanted 2 MeV Ag^{2+} ions on 0001- oriented 6H-SiC single crystalline wafers at -63 °C and 600 °C temperatures to a fluence of 5×10^{16} cm^{-2}. Complete amorphization occurred on the surface region, up to a depth of 748 nm for the implantation at -63 °C, while a highly crystalline structure was retained after implantation at 600 °C [Jia04]. To study the response of the implanted silver in crystalline and amorphous states of SiC, Jiang et al. irradiated the two wafers (implanted at 600 °C and at -63 °C) with 5.4 MeV Si^+ ions to a fluence of 5×10^{15} cm^{-2} at 600 °C. RBS-C was used to study the diffusion of silver and radiation damage respectively.

The results indicated that Ag implants were very immobile in SiC. Silver atoms did not diffuse in any phase of SiC (crystalline or amorphous) in the presence or absence of external ion irradiation at or below 600 °C. At 1300 °C, the implanted silver did not move in a single crystalline structure of SiC but appeared to migrate towards the surface in completely amorphised SiC. This behaviour was thought to be related to a less dense structure of fully amorphised material that provided diffusion paths for the implanted silver at a high temperature (1300 °C). No diffusion coefficient of silver was calculated in this study [Jia04]. However, these results are inconsistent with that of MacLean et al. which might be due to structural differences in the material studied, i.e. CVD-SiC for Maclean et al. and Nabielek et al. [Mac04][Nab76] and 6H-SiC for Jiang et al. [Jia04].

6.4 DIFFUSION COUPLE METHODS

The diffusion couple method is widely used in investigating the in-diffusion of a particular material into a substrate. In this method the substance of interest is coated on the substrate to form a diffusion couple. For in-diffusion investigation the diffusion couple is then post annealed to a temperature below the substance's melting point in order to avoid evaporation of the substance, or the diffusion couple is manufactured in such a way that silver would remain in the substrate surface above its melting point (for example, encapsulation is used in this thesis). This section discusses the results of previous silver-SiC diffusion couple methods.

The normal diffusion couple consisting of a diffusing metal and the substrate is not applicable to a silver diffusion experiment owing to the low melting point of silver, which will cause silver on SiC to evaporate from the surface or escape through any open edges rather than diffusing into SiC at temperatures near or above 960 ^{o}C. These factors have hindered silver-SiC diffusion couple studies.

In addition to the study of migration of implanted silver in silicon carbide, MacLean et al. investigated the migration of silver using the diffusion couple [Mac04]. MacLean's diffusion couples were hollow shells fabricated from either graphite or SiC. Two half shells were fabricated with an overlapping seam, coupled together to form a 1.9 cm hollow sphere with 0.076 cm thick walls. Silver powder (99.9995% purity) was placed inside one half and enclosed inside the shell to form the diffusion couple. Another coating was deposited on the outside of the joined half shells.

The diffusion couples were annealed at temperatures between 1050 ^{o}C and 1700 ^{o}C for periods between 2h and 1760 h. Mass loss measurements after annealing indicated silver had been released from the diffusion couples, but no silver was detected during concentration profile measurements in SiC. However, leak test results indicated the presence of cracks in many of the SiC coatings, which were assumed to have provided pathways for silver. The crack sizes were estimated by means of the vapour flow model.

A detailed summary of most of the work done on the release of silver in a high temperature reactor can be found in [Han04][Pet04] while summaries of the FPs released in the Jülich AVR reactor are contained in [Nab08].

Most of the results reported here stem from the batch and individual inventory measurements. Only a few result from ion implantation, which is used in our study. The only study that is directly related to ours is that by Jiang et al [Jia04]. Therefore, our results will be compared to it.

6.5 REFERENCES

[Ami83] W. Amian, D. Stöver, Nucl. Tech. **61** (1983) 475.

[Bro76] P. E. Brown, R. L. Faircloth. J. Nucl. Mater. **59** (1976) 29.

[Bul84] R.E. Bullock. J. Nucl. Mater. **125** (1984) 304.

[För82] R. Förthmann, E. Gyarmati, J. Linke, E. Wallura, High Temp.-High Press. **14** (1982) 477.

[Han04] D. Hanson, A Review of Radionuclide Release from HTGR Core During Normal Operation, EPRI, Palo Alto, CA:**1009382** (2004).

[Jia04] W. Jiang, W.J. Weber, V. Shutthanandan, L. Li, S. Thevuthasan, Nucl. Instr. and Meth. B **219-220** (2004) 642.

[Mac04] H. J. MacLean. SiC," PhD Thesis, Massachusetts Institute of Technology (2004).

[Min00] K. Minato, K. Sawa, T. Koya, T. Tomita and A. Ishikawa, Nucl. Tech. **131** (2000)36

[Min93] K. Minato, T. Ogawa, K. Fukuda, H. Sekino, H. Miyanishi, S. Kado, I. Takahashi J. Nucl. Mater. **202** (1993) 47.

[Min98] K. Minato, T. Ogawa, K. Fukuda, H. Sekino, H. Miyanishi, S. Kado, I. Takahashi, HRB-22 Capsule Irradiation Test for HTGR Fuel (JAERI/USDOSE Collaborative Irradiation Test), JAERI-Research **98-021** (1998).

[Nab08] H. Nabielek, K. Verfondern, M. Kania, Jülich AVR Pebble-Bed Reactor, 4th International Topic Meeting on High Temperature Reactor Technology, Washington D.C, USA, Sep. (2008).

[Nab77] H. Nabielek, P.E. Brown, P. Offermann, Nucl. Tech. **45** (1977) 483.

[Pea80] R. L. Pearson, R. J. Lauf, T. B. Lindemer, Simulated Fission Product-SiC Interaction in TRISO-Coated LEU or MEU HTGR Fuel Particles, ORNL/TM-**8059** (1980).

[Pea82] R. L. Pearson, R. J. Lauf, T. B. Lindemer. The Interaction of Palladium, the Rare Earths, and Silver with Silicon Carbide in HTGR Fuel Particles, ORNL /TM-**8059** (1982).

[Pet04] D. Petti, P. Martin, R. Ballinger, Development of Improved Models and Designs for Coated-Particle Gas Reactor Fuels, I-NERI, INEEL/EXT-**05- 02615** (2004).

[Sch91] W. Schenk, H. Nabielek. Nucl. Tech. **96** (1991) 323.

CHAPTER 7 RESULTS AND DISCUSSION

Diffusion of silver into single crystalline 6H-SiC was investigated using the two methods discussed in Chapter 5. With first method surface layer diffusion was examined. For this a silver layer was deposited onto clean single crystal 6H-SiC samples. These were then annealed under vacuum to temperatures below the melting point of silver. The results of the post annealing Rutherford backscattering spectroscopy (RBS) and SEM analyses indicated no in-diffusion of silver and an absence of silver on and in the SiC at these temperatures. This was hypothesized to be the result of a wetting problem between silver and SiC. Further, the layer in-diffusion of silver was investigated by encapsulation. SiC samples were encapsulated in a quartz ampoule together with a silver source to maintain a silver vapour layer on the samples' surface during annealing. The encapsulated samples were annealed at temperatures below the quartz softening temperature (1200 ^{o}C). The post annealing RBS and SEM analyses results indicated no in-diffusion of silver into 6H-SiC and an absence of silver on 6H-SiC surfaces.

Due to the negative results of the layer in-diffusion of silver into 6H-SiC, further research was undertaken into silver diffusion in 6H-SiC by ion implantation. Silver was implanted in 6H-SiC at different temperatures (i.e. room temperature (23 ^{o}C), 350 ^{o}C and 600 ^{o}C) at a fluence of 2×10^{16} cm^{-2}. The samples were then annealed from 700 ^{o}C up to 1600 ^{o}C for different annealing times. Using RBS the silver depth profiles after implantation and after annealing were compared to calculate diffusion coefficients. RBS-C was employed to investigate the production of radiation damage and also the annealing out of radiation damage during annealing. SEM was utilised to investigate the changes occurring on the sample surfaces during annealing.

This chapter presents and discusses the results of this study and is organised as follows: section 7.1 discusses the layer in-diffusion results and 7.2 the implantation results.

7.1 LAYER IN-DIFFUSION

The in-diffusion of a vacuum deposited layer of naturally-occurring silver into 6H-SiC was investigated using RBS and SEM at temperatures below the melting point of silver (T_m= 960 ^{o}C). Due to the extremely low diffusion in this temperature range [Jia04], samples with silver deposited on their surfaces had to be kept in the vacuum furnace for very long periods (100 hours or more). Even then a direct determination of the silver diffusion profile near the surface was not guaranteed. Therefore, silver was to be chemically removed after annealing so as to analyse the exposed SiC surface for any penetration of silver, exploiting the higher depth resolution resulting from the much reduced energy straggling from the top surface silver layer.

The samples were then annealed at 800 ^{o}C for 10 hours, which is a temperature well below the melting point of silver (960 ^{o}C). The RBS and SEM analyses indicated that the deposited silver disappeared without diffusing into SiC. At first we believed this was due to the sublimation of silver at that temperature. However, the vapour pressure calculation at 1000 ^{o}C in Appendix A does not confirm our initial belief.

Owing to this problem, the samples with 100 nm of silver on their surface were vacuum encapsulated together with a silver source in a quartz ampoule, as explained in chapter 5. The purpose of the said source was to maintain a silver layer or silver vapour on the samples' surface. The encapsulated samples were thereafter annealed in a vacuum at 800 ^{o}C, 900 ^{o}C and 1000 ^{o}C for 10 h. The RBS analyses of the annealed samples indicated that no silver was left on the surfaces and also discovered no trace of diffused silver beyond the silicon carbide surfaces. These results were confirmed by SEM in conjunction with EDS. However, silver was found on the walls of the quartz glass ampoule. At first we thought this to be supporting the suggestion of the sublimation of silver. No further annealing was performed at temperatures above 1000 ^{o}C to avoid the softening of quartz glass, which at occurs around 1200 ^{o}C.

The disappearance of the silver layer from the SiC surface was investigated further at temperatures from 200 ^{o}C to 700 ^{o}C. This was undertaken by isochronal annealing

(for 30 minutes) at temperatures from 200 ^{o}C to 700 ^{o}C. The SEM results depicted in Figure 7-1 show that the as-deposited silver layer is fairly smooth and possesses a homogenous structure. Silver islands start to form at 200 ^{o}C and become larger and more visible as the annealing temperature increases up to 400 ^{o}C. At the lower temperatures (200 to 400 ^{o}C), facet formation indicates the polycrystalline nature of these islands which is clearly visible in the SEM images. At the higher temperatures these long facets islands break into bigger and smaller facets islands. This is due to the coalescence of the smaller islands into bigger islands along with increasing drop formation. The black spots in the SEM image of the sample annealed at 200 ^{o}C are cavities (indicated by C) in the Ag layer. Defects in the Ag layer, such as grain boundaries, internal stresses, and local weak bonding between Ag and SiC, could trigger cavity formation. In the same SEM image the straight lines inside the large crystals could be micro twins, indicated by T. Some of the larger silver islands also exhibit grain grooving or steps on the surface. The islands that are formed at higher temperatures, e.g. at 700 ^{o}C, are composed of small islands clustered together and bigger islands with openings between them - see the low magnification image in figure 7-1 (the un-labelled image).

The formation of islands is the result of weaker binding forces between silver atoms and SiC as compared to the binding forces between silver atoms and such islands constitute the proof that silver does not wet SiC. Therefore, the disappearance of silver is caused by the formation of silver islands on the SiC surface and their coalescence into droplets, which run off the samples' surface in longer duration annealing.

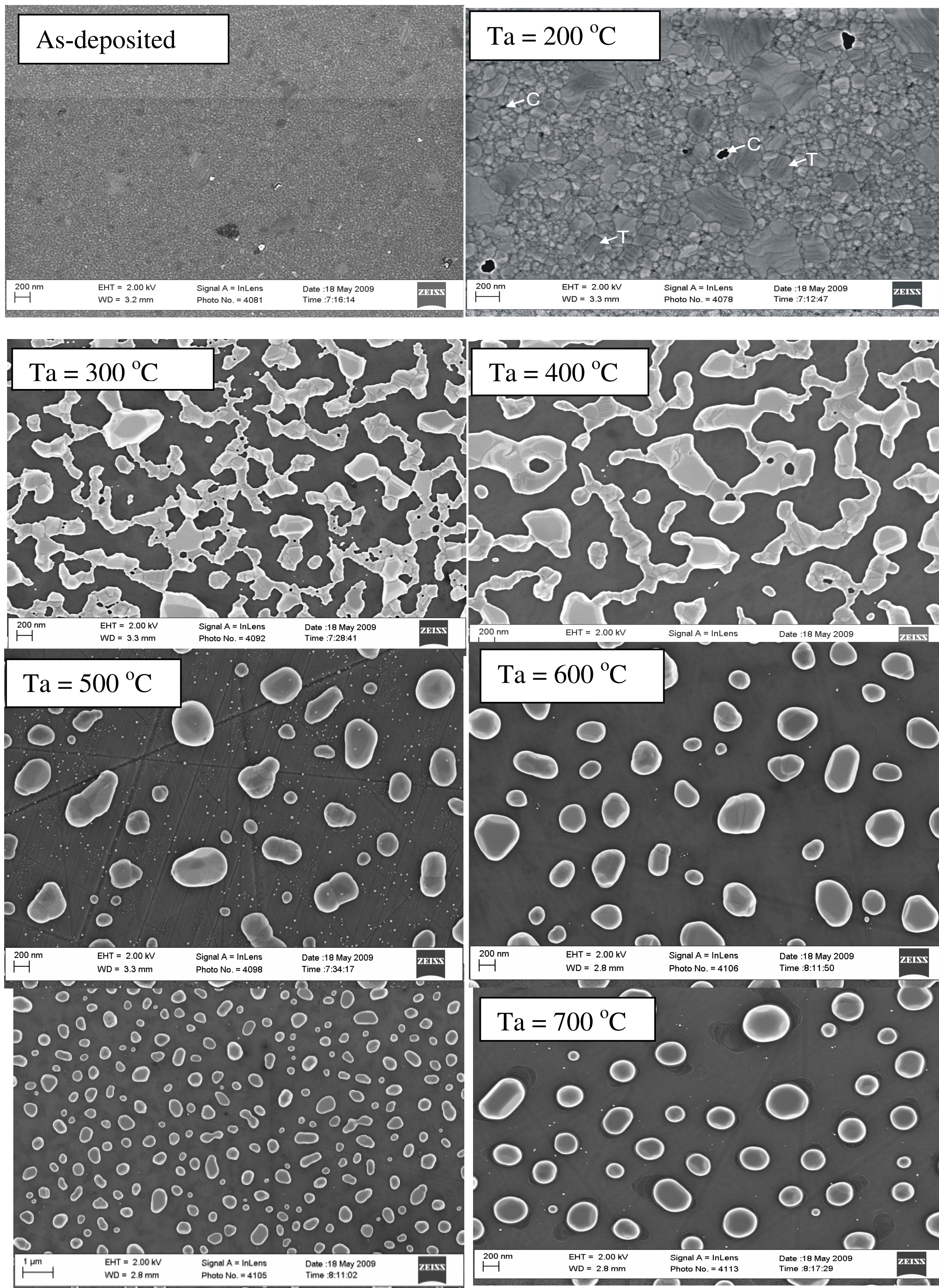

Figure 7-1: SEM images of a 100 nm silver layer vacuum deposited on 6H-SiC after isochronal annealing at temperatures from 200 °C to 700 °C for 30 minutes compared with the as-deposited sample. A low magnification image of the sample annealed at 700 °C is included and is the un-labelled image in the above set of images.

7.2 IMPLANTATION RESULTS

Due to the negative results of layer in-diffusion of silver into silicon carbide as discussed above, further studies were performed to try and elucidate the diffusion mechanism. In these experiments, silver was implanted into SiC. For this purpose 360 keV $^{109}Ag^+$ with a fluence of 2×10^{16} cm^{-2} was implanted in single crystal 6H SiC wafers at room temperature (23 ^{o}C), at 350 ^{o}C and at 600 ^{o}C. To reduce channelling during implantation, a tilt angle of 7° relative to the normal was used. To avoid excessive beam induced target heating, the flux was kept below 10^{-13} cm^{-2}s^{-1}.

To investigate the diffusion behaviour of silver and annealing of radiation damage, the implanted samples were vacuum annealed in a computer controlled *Webb 77 Vacuum Furnace* for different annealing time cycles, i.e. 10 h cycles and 30 minute (min) cycles from temperatures below the melting point of silver (960 ^{o}C) up to 1600 ^{o}C.

The diffusion behaviour, production, and annealing of radiation damage results are discussed as follows: 7.2.1 considers the room temperature implantation results while 7.2.2 discusses the high temperature (350 ^{o}C and 600 ^{o}C) implantation results.

7.2.1 ROOM TEMPERATURE IMPLANTATION

In this section the results of silver implanted into 6H-SiC at room temperature are discussed. They are organised into subsection 7.2.1.1, which considers the radiation damage and the annealing of radiation damage; and subsection 7.2.1.2 which discusses the results of the diffusion experiments.

7.2.1.1 RADIATION DAMAGE RESULTS

The channelled spectrum of the as-implanted silver at room temperature is illustrated in figure 7-2. Also depicted are the random spectrum and the spectrum of an unimplanted sample, with the channelled spectrum and unimplanted spectrum normalised to the random spectrum for comparison. The backscattered yield/counts in the as-implanted channelled spectrum of the implanted sample correspond to damage created during implantation. The region where the channelled spectrum overlaps with

the random spectrum is an amorphous one caused by implantation damage. The depth of this region is approximately 270 nm. Comparing this depth with the typical $R_p=109$ *nm* and $\Delta R_p = 39$ *nm* of silver profile, it becomes clear that implanted silver is embedded within the amorphous region. The amorphous width (or depth) of the amorphous layer is measured as the width between the half maximum of Si surface signal and the half maximum of the Si signal when it decreases at the end of the amorphous layer as illustrated in figure 7-2. Therefore, 6H-SiC implanted at room temperature consists of an amorphous region indicated by *width* - in Figure 7-2, the crystalline or bulk region indicated by *cr* and the interface labelled by *B* (the region between the amorphous layer and the bulk region).

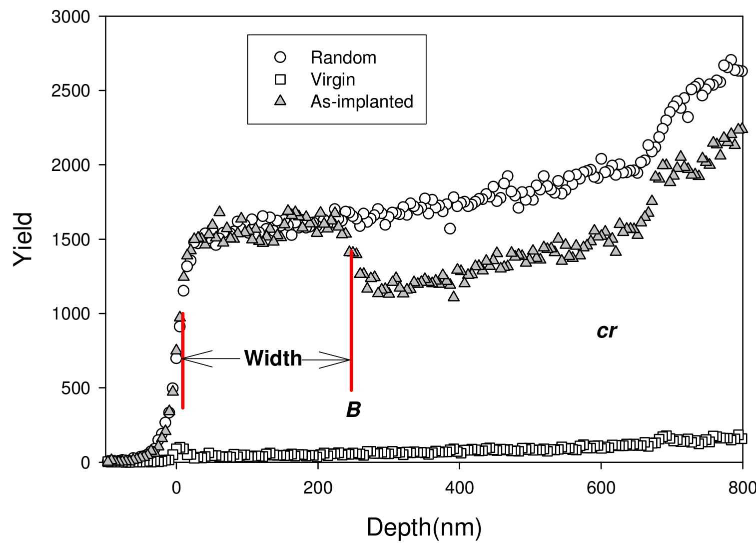

Figure 7-2: Random and aligned backscattering spectra of SiC from 6H-SiC implanted at room temperature with a fluence of 2×10^{16} cm^{-2} compared with the aligned/channelled spectrum of the virgin sample. The α–particle energy was 1.6 MeV and the scattering angle was 165°.

In the initial experiments, 6H-SiC samples implanted at room temperature were sequentially annealed at 960 °C for 2h, 1500 °C for 10 h and 1600 °C for 10 h. The results are shown in figure 7-3. Annealing at 960 °C for 2 h causes an epitaxial re-growth from the bulk to reduce the width of the amorphous region from 270 nm to about 265 nm while at 1500 °C for 10h it further reduces to approximately 220 nm. At 1600 °C for 10 h, the crystallinity of the amorphous region is nearly recovered with

some defects still remaining. The higher de-channelling in the spectrum of the sample annealed at 960 °C might be due to the variations in the crystal alignment.

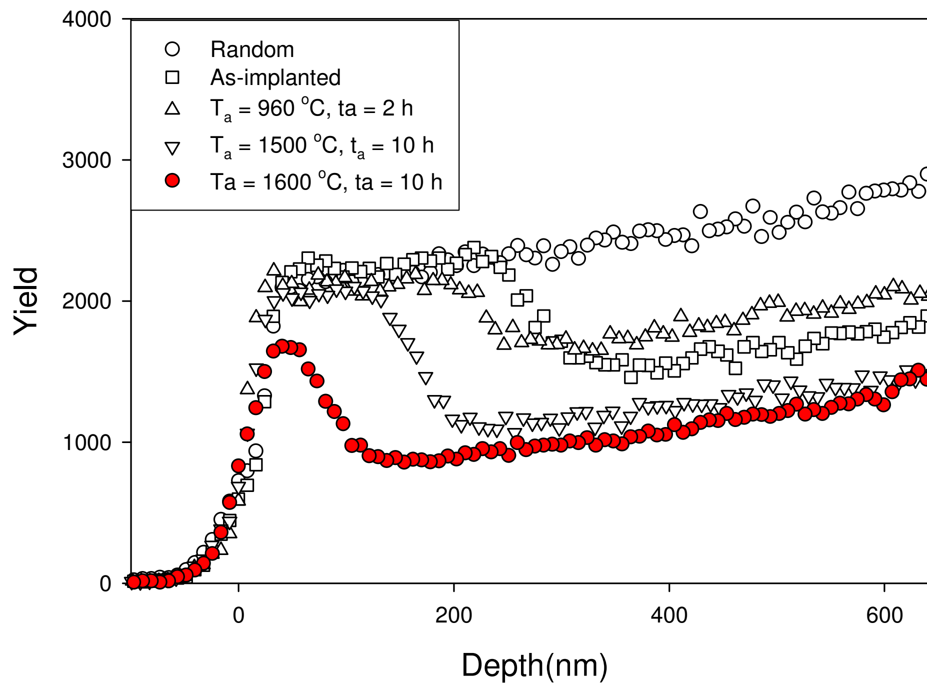

Figure 7-3: Random and aligned backscattering spectra of SiC from 6H-SiC implanted at room temperature (23 °C) and submitted to sequential annealing at 960 °C for 2 h, at 1500 °C for 10 h and at 1600 °C for 10 h.

For the isochronal study, new samples implanted at room temperature were annealed for 10 h at temperatures of 1100 °C, 1200 °C, 1300 °C and 1400°C. The results are to be seen in figure 7-4. Annealing of samples at 1100 °C and 1200 °C causes an epitaxial re-growth from the bulk to reduce the width of the amorphous region from 270 nm to about 240 nm, while annealing at 1300 °C and 1400 °C reduced the amorphous width to 180 nm and 92 nm respectively. These results imply that at 1100 °C and 1200 °C re-crystallization occurs at the same rate. The rate increases with temperatures above 1200 °C, displaying a further reduction of amorphous width at 1300 °C and 1400 °C.

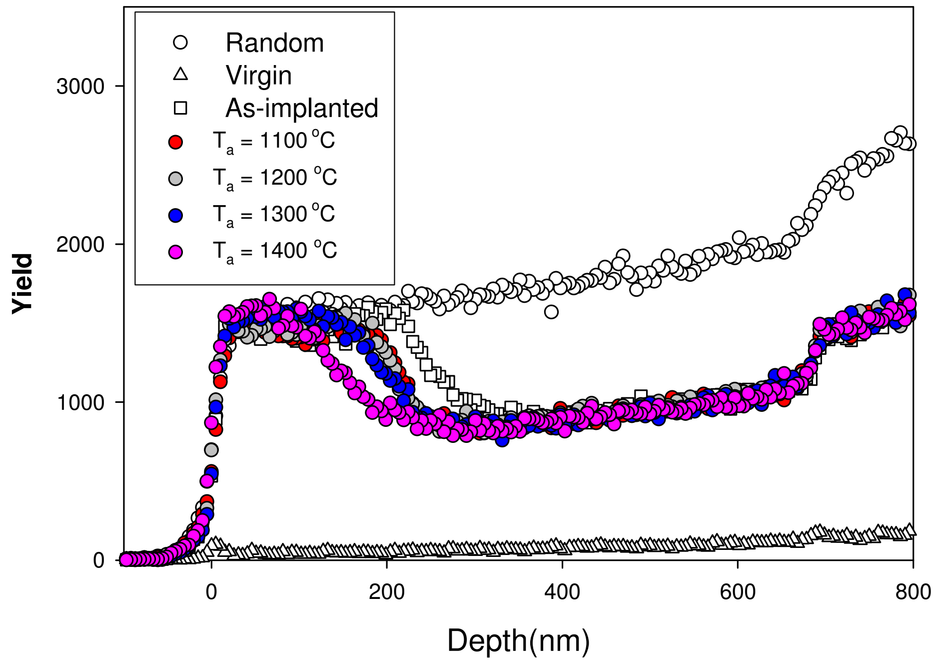

Figure 7-4: *Random and aligned backscattering spectra of SiC for new 6H-SiC implanted at room temperature (23 °C) and submitted to isochronal annealing at 1100 °C, 1200 °C, 1300 °C and 1400 °C for a 10 hours cycle compared with the virgin 6H-SiC aligned spectrum.*

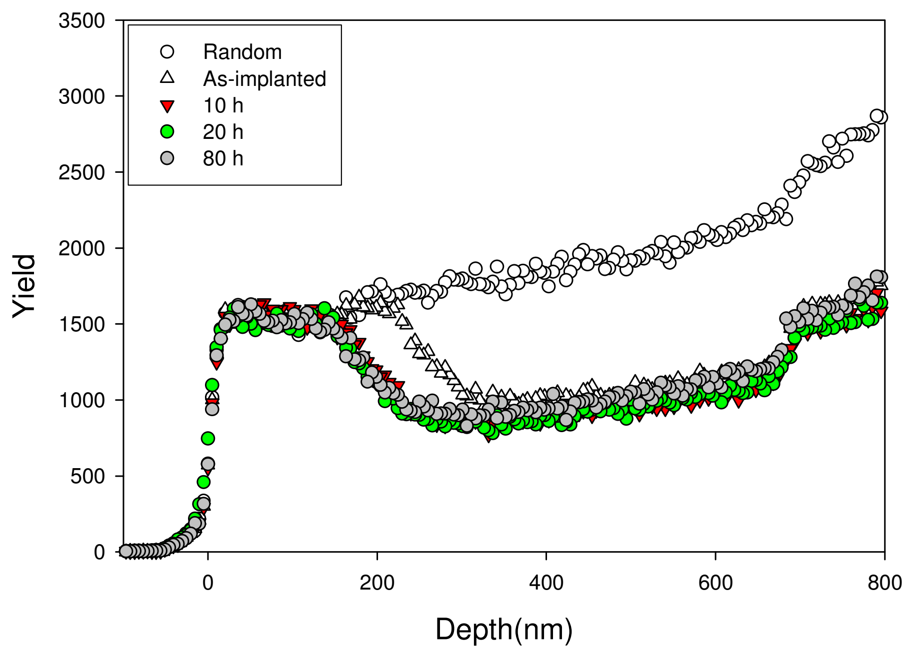

Figure 7-5: Random and aligned backscattering spectra of SiC from 6H-SiC implanted at room temperature (23 °C) and submitted to isothermal annealing at 1300 °C for 10 hours cycles up to 80 h; the 40 h aligned spectrum is not shown.

Isothermal annealing of the sample implanted at room temperature at 1300 °C for 10 h cycles up to 80 h demonstrates that the amorphous region is reduced from 270 to 180 nm during the first annealing cycle and does not decrease with further annealing at the same temperature (see figure 7-5). Isothermal annealing of the sample implanted at room temperature at 1350 °C for 30 minutes reduced the amorphous layer to about 220 nm. This depth remained constant with further annealing at 1350 °C (see figure 7-6). These results indicate that more re-crystallization occurs during a longer annealing time (10 h) compared to the shorter annealing period (30 min) since the difference in temperature between these cases is small.

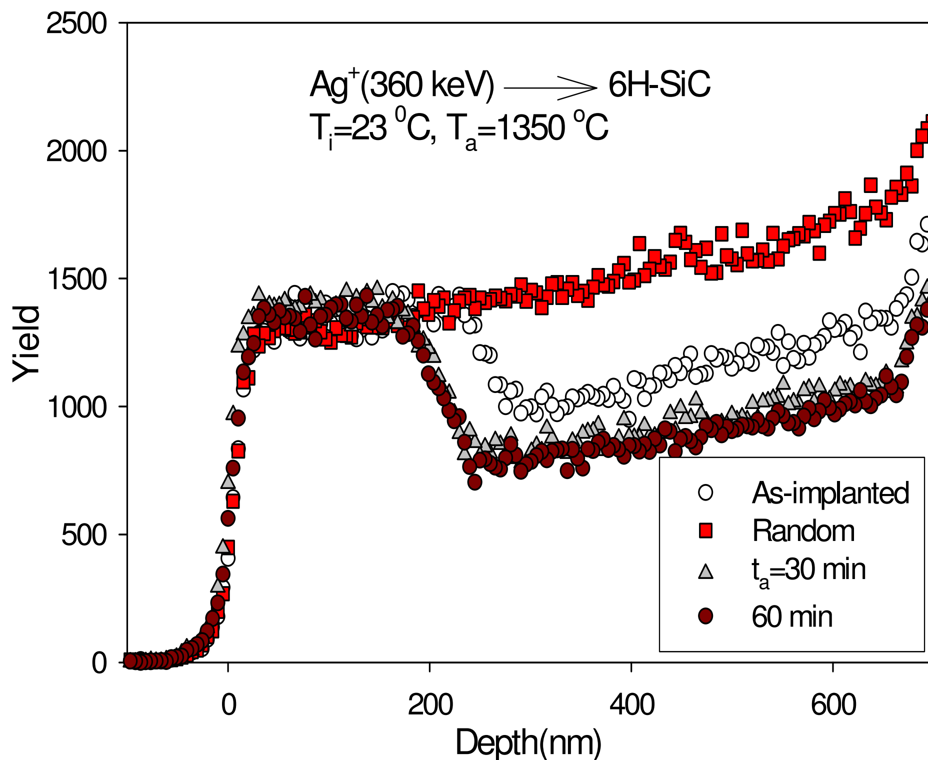

Figure 7-6: Random and aligned backscattering spectra of SiC from 6H-SiC implanted at room temperature (23 °C) and submitted for isothermal annealing at 1350 °C for a 30 minutes cycle.

Further investigation of the sample annealed at 1300 °C for 80 h was performed using Raman scattering spectroscopy to ascertain whether or not the sample was still amorphous (after the first annealing cycle) as suggested by the RBS channelling. This was performed by comparing its results with those of the other samples listed below.

Raman scattering at a visible wavelength (514.5 nm) was performed on the following 6H-SiC samples:

- unimplanted;
- implanted with silver at room temperature; and
- the sample implanted with silver which was annealed at 1300 ^{o}C for 80 h.

The Raman spectra are depicted in figure 7-7. The spectrum for unimplanted 6H-SiC exhibited the characteristic Raman modes for perfect 6H-SiC [Fen99]. After silver implantation at room temperature, three broad Raman bands appeared, with the bands centred around 500, 800 and 1420 cm^{-1}. These broad peaks are caused by Si-Si, Si-C and C-C vibrations, respectively [Fen99]. These bands indicate a loss of 6H-SiC crystallinity and the formation of an amorphous phase as a result of ion implantation. During the amorphization, bonds are formed between Si-Si and C-C, in contrast with crystalline SiC where only Si-C bonds occur. After annealing at 1300 ^{o}C for 80 h the broad peaks disappeared while the Raman spectrum for 6H-SiC reappears. This indicates the recovery of the SiC crystalline structure due to annealing at 1300 ^{o}C for 80 h. A comparison of the Raman intensity of the virgin sample with the Raman intensity of the sample annealed at 1300 ^{o}C for 80 h in figure 7-7 shows that defects are still present in the annealed sample (the lower relative Raman intensity means defects in SiC).

From the Raman results of samples implanted at room temperature and annealed at 1300 ^{o}C for 80 h, it is evident that the sample is no longer amorphous but that defects are still present. However, these results contradict the channelling results of the sample-see figure 7-5. This contradiction could be due to the fact that during the first annealing cycle the amorphous layer was annealed into smaller crystals or crystallites that are randomly orientated or misoriented to the substrate, which resulted in the seemingly amorphous layer in channelling results. The same channelling results could be achieved if, during the first cycles, the amorphous layers re-crystallized to other polytypes of SiC such as 3C-SiC, as suggested by Nakamura et al. [Nak02]. Nakamura et al. found that the annealing of amorphised 6H-SiC leads to the re-growth of the micro-twinned 3C-SiC crystals.

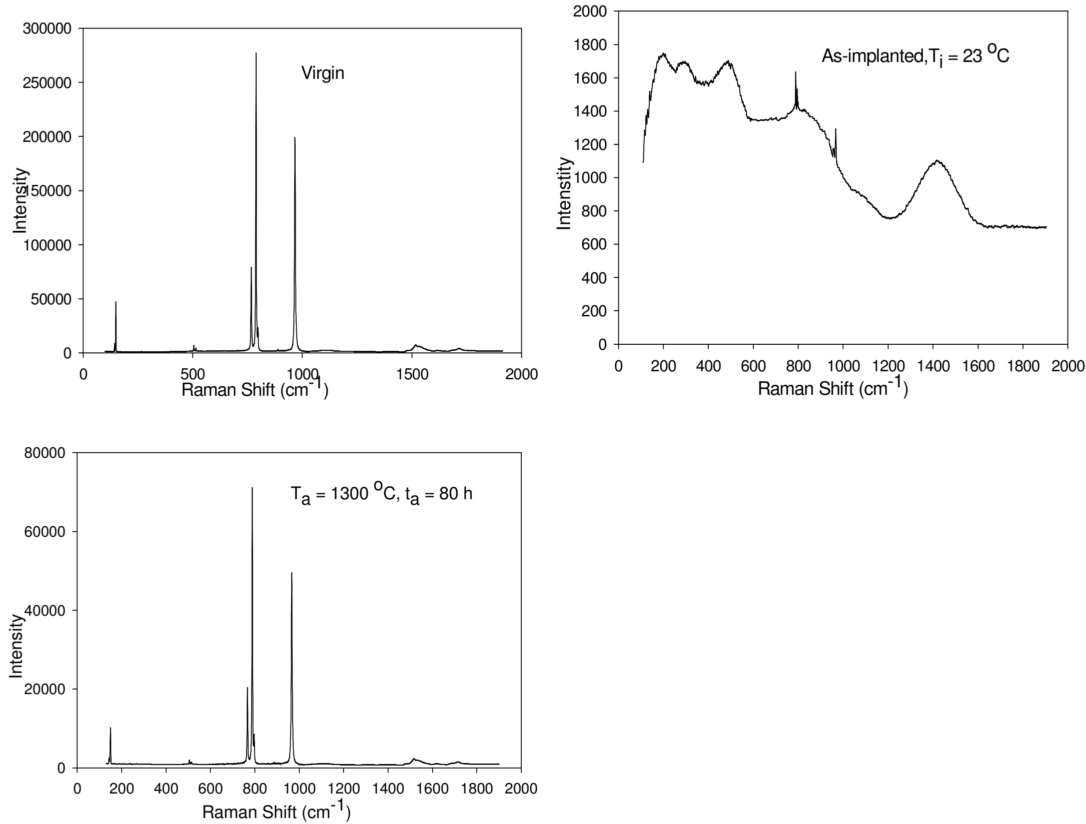

Figure 7-7: Comparative Raman spectra from un-implanted (virgin) 6H-SiC, silver implanted into 6H-SiC at room temperature (23 ^oC) and after annealing at 1300 ^oC for 80 h.

Sequential isochronal annealing (for 30 minute cycles) of samples implanted at room temperature at the temperatures 700 ^oC, 800 ^oC, 900 ^oC, 1000 ^oC, 1100 ^oC, 1200 ^oC, 1300 ^oC, 1400 ^oC, 1500 ^oC and 1600 ^oC indicates that epitaxial re-growth is already taking place at 700 ^oC (see figure 7-8(a) and figure 7-8(b)). The widths of the amorphous layer (measured as shown in figure 7-2) were plotted as functions of the annealing temperatures in figure 7-8(b). Annealing of the sample at 700 ^oC decreases the width of the amorphous layer from 270 to about 250 nm. This amorphous width remains at about 250 nm up to 1400 ^oC where it further decreases to about 204 nm. At 1500 ^oC it decreases to about 170 nm. The crystal structure appears to be recovered after annealing at 1600 ^oC but with more carbon being detected at this temperature. This might be due to decomposition of SiC at this temperature, which allows Si to evaporate since this temperature is well above the melting point (1411 ^oC) of Si. No signal from the implanted Ag was observed in the RBS spectrum. This could indicate that the top amorphous layer is thermally etched away or sublimated during annealing, as was suggested by Wendler et al. and Rao [Wen98][Rao03]. Therefore, the decrease

in the width of the amorphous layer at low temperatures might be due either to an epitaxial re-growth from the amorphous/bulk interface as can be seen in figure 7-8(a) or to the sublimation of the (top) amorphous layer during annealing. At the temperatures where epitaxial re-growth did not occur as observed by channelling, this result might imply that the amorphous layer re-crystallised to other polytypes as explained above, while the thermal etching was negligible at those temperatures.

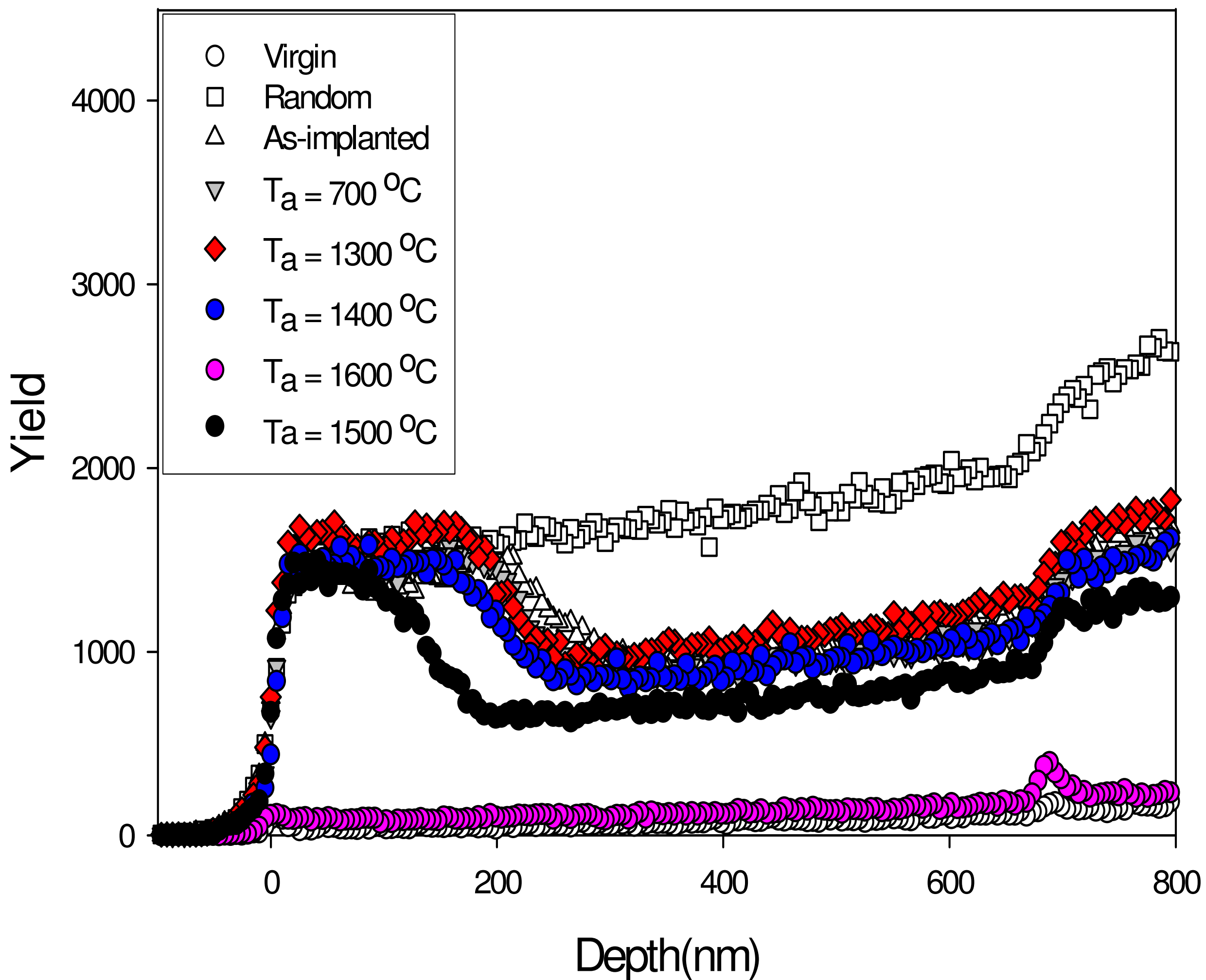

Figure 7-8(a): Random and aligned backscattering spectra of SiC from 6H-SiC implanted at room temperature (23 °C) and isochronally annealed at temperatures from 700 °C to 1600 °C for 30 minutes cycles.

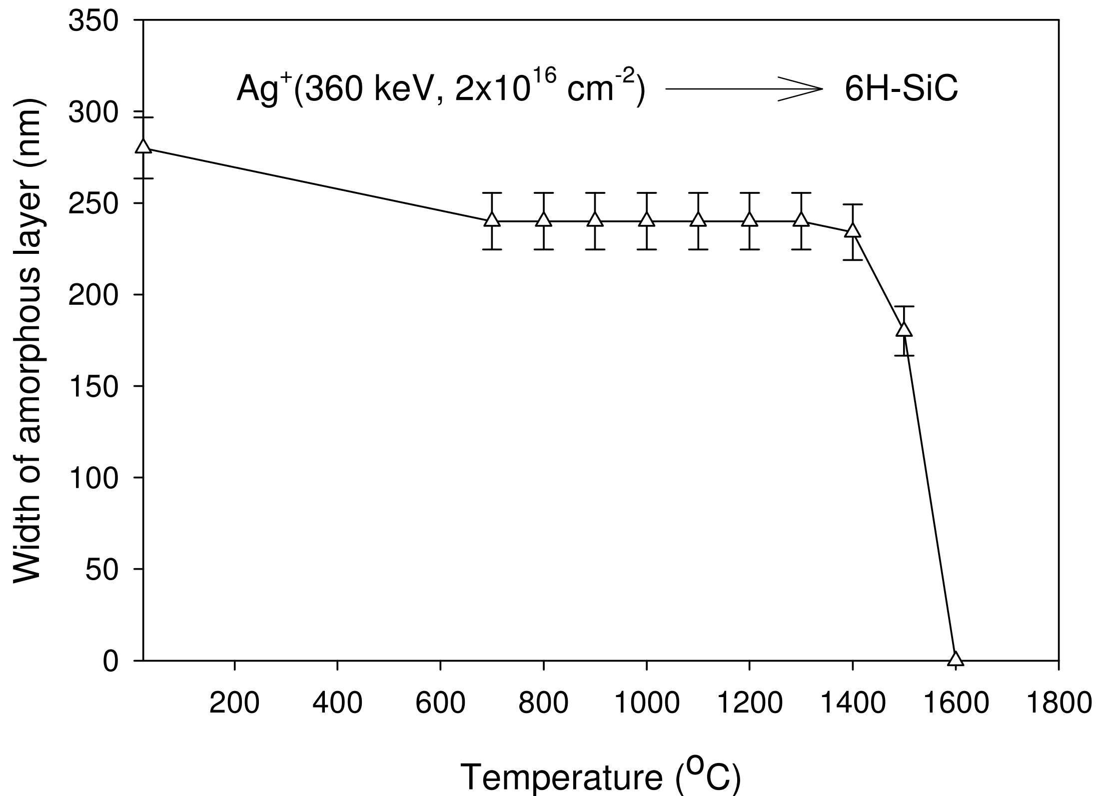

Figure 7-8(b): The width of the amorphous layer as a function of annealing temperatures during the isochronal sequential annealing from 700 °C to 1600 °C for 30 minute cycles.

In summary, our production of radiation damage during the implantation results of this study is in agreement with the results of Wendler et al. [Wen98]. Wendler et al. have shown that for high energy ion damage, amorphization is not achieved for implantation temperatures above 250 °C. Furthermore, the annealing of radiation damage produced during implantation results is in agreement with Bohn et al. [Boh87] and Pacaud et al. [Pac96]. Bohn et al. found that the amorphous layers re-grew epitaxially from the underlying undamaged material up to 1500 °C, above which the damage annealed rapidly in a narrow temperature interval while Pacaud et al. showed that annealing of the amorphous layer cannot be achieved at the temperature of 1500 °C. Decomposition of SiC, resulting in the excess of carbon on the SiC, is found to be taking place at 1600 °C. This is caused by silicon evaporating at 1600 °C, leaving excess carbon and thus causing lager carbon peak on the SiC RBS spectrum.

7.2.1.2 IMPLANTED LAYER DIFFUSION RESULTS

Measurements to determine silver diffusion in 6H-SiC were performed simultaneously with the annealing of radiation damage discussed above, using random spectra from the RBS. A typical profile of silver implanted at room temperature as compared with TRIM 98 prediction is depicted in figure 7-9, where the fluence (ϕ), experimental and TRIM 98 moments are also shown. By comparing the experimental moments with TRIM 98 ones, it became quite clear that the measured projected range of silver peak is about 2% deeper, which is within TRIM calculation error of 5 %. The typical FWHM of silver peak is about 63 % wider as compared to the TRIM 98 results but the concentration is the same in both peaks. This difference in FWHM causes the silver concentration of the TRIM simulation to be higher than the measured one around the projected range (see figure 7-9). This discrepancy is caused by the fact that TRIM does not take into account the crystal structure or dynamic composition changes in the material that occur when the ion penetrates materials; however, approximations are used in this program. These include the following:

- binary collision (i.e. the influence of neighbouring atoms is neglected);
- recombination of knocked off atoms (interstitials) with the vacancies is neglected;
- the electronic stopping power is an averaging fit to a large number of experiments;
- the interatomic potential as a universal form which is an averaging fit to quantum mechanical calculations;
- the target atom which reaches the surface is able to leave the surface (be sputtered) if it has sufficient momentum and energy to pass the surface barrier.

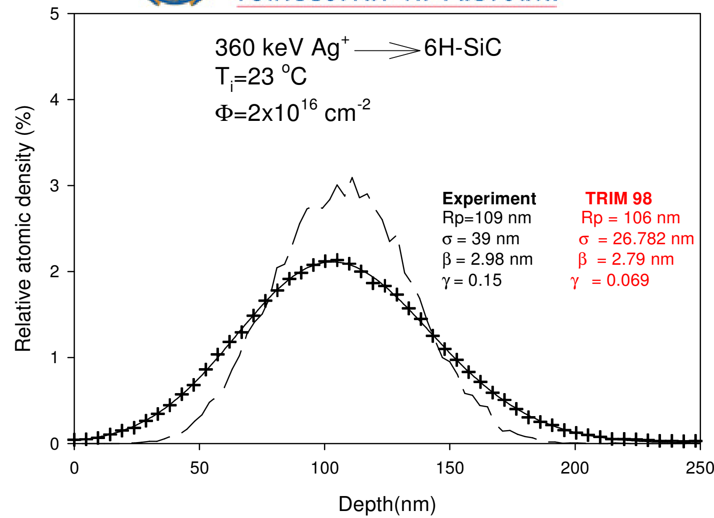

Figure7-9: Silver depth profile in 6H-SiC implanted at room temperature as determined by RBS. The broken line is the theoretical distribution obtained with the TRIM-98 code.

The silver depth profiles in 6H-SiC implanted at room temperature after sequentially annealed at 960 °C for 2 hours, 1500 °C for 10 hours and 1600 °C for 10 hours as compared with the as-implanted profile are illustrated in figure 7-10. Annealing at 960 °C narrows the silver profile's width, causing the concentration to be greater at the centre compared to that of the as-implanted profile (see figure 7-10). Similar results could be achieved if the silver were to form a precipitate at this temperature. If the same sample (that was annealed at 960 °C) is further sequentially annealed at 1500 °C and 1600 °C for 10 hours, the silver profile tends to shift without any broadening toward the surface at 1500 °C with 2 % of silver loss from the surface (the amount of silver detectable by RBS is proportional to the area under the silver curve.). At 1600 °C more than 50% of the silver is lost from the surface. From the shape of the distribution and from fitting the profile to an Edgeworth function, as discussed in section 5.6, it is clear that no detectable Fickian-type diffusion into the bulk or towards the surface is taking place. The shift of silver profile towards the surface and subsequent loss at higher temperatures might be due to material (SiC) being removed from the surface during annealing at these temperatures. This will be discussed as this section progresses. These diffusion results seem to be supporting the suggestion that the ion bombardment-induced amorphous SiC layer is no longer amorphous (after annealing at 1300 °C for 80 h) as discussed in section 7.2.1.1, but re-crystallized to other polytypes of SiC such as 3C-SiC through which silver does not diffuse.

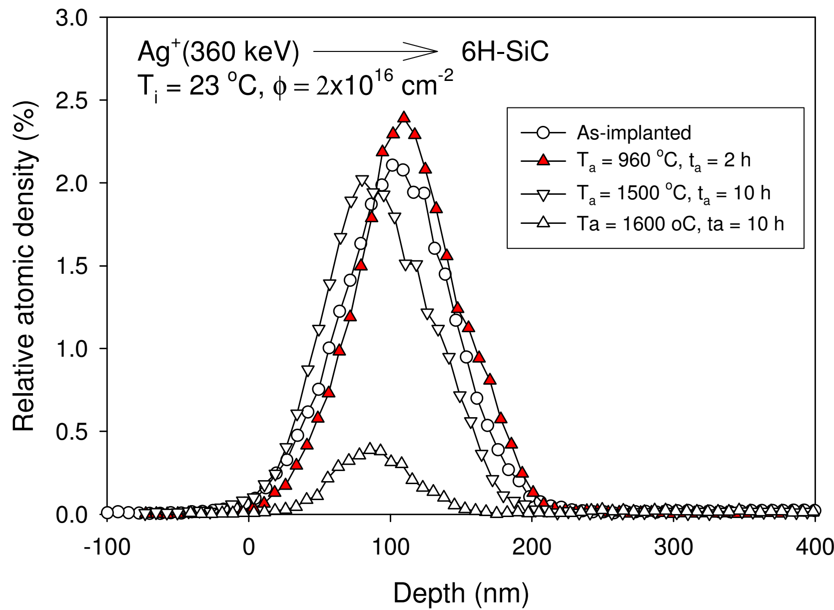

Figure 7-10: Silver depth profiles of 6H-SiC implanted at room temperature after annealing at 960 °C for 2 hours, 1500 °C for 10 hours and 1600 °C for 10 hours.

Owing to the unexpected results of our initial diffusion experiments, silver diffusion in single crystal 6H-silicon carbide was investigated further by isochronal annealing of new samples at 1100 °C, 1200 °C, 1300 °C and 1400 °C for 10 hours, so that the results of annealing at higher annealing temperatures are not influenced by lower annealing temperatures as in our previous experiments. Therefore, in these experiments all samples were initially amorphised SiC while in the former experiments the samples were only amorphous during annealing at a lower temperature, i.e. 960 °C. The results of the isochronal annealing experiments are illustrated in figures 7-11 to 7-13. Silver loss starts at 1100 °C (see figure 7-12), while silver diffusion in amorphous SiC accompanied by silver loss from the surface begins at 1300 °C (figure 7-11). The silver profile maintains a symmetrical shape with less than 30% of silver lost from the surface. The silver retained ratio was calculated from the total counts/yield of silver after annealing, divided by the counts of the as-implanted silver peaks. At 1400 °C silver diffuses significantly, with the silver profile shifting towards the surface and becoming asymmetric (see figure 7-11). 50% of silver is lost from the surface at 1400 °C. At temperatures below 1300 °C the widths of the silver profiles become narrower and their counts decrease. This is the result of some of the implanted silver forming precipitates, and some silver being lost at these temperatures. The silver precipitates can be seen in the cross sectional SEM image for

a sample implanted at room temperature and then annealed at 1250 °C for 30 minutes (figure 7-14). This sample in figure 7-14 was prepared by standard TEM sample preparation, i.e. glued on a poly crystalline SiC, together with chemical polishing and ion milling. In figure 7-14, the surface from which implantation was performed is indicated as S, while Ag represents the silver precipitates and Poly SiC represents polycrystalline SiC. This is the proof that below 1300 °C silver forms precipitates, as has been suggested above in this section.

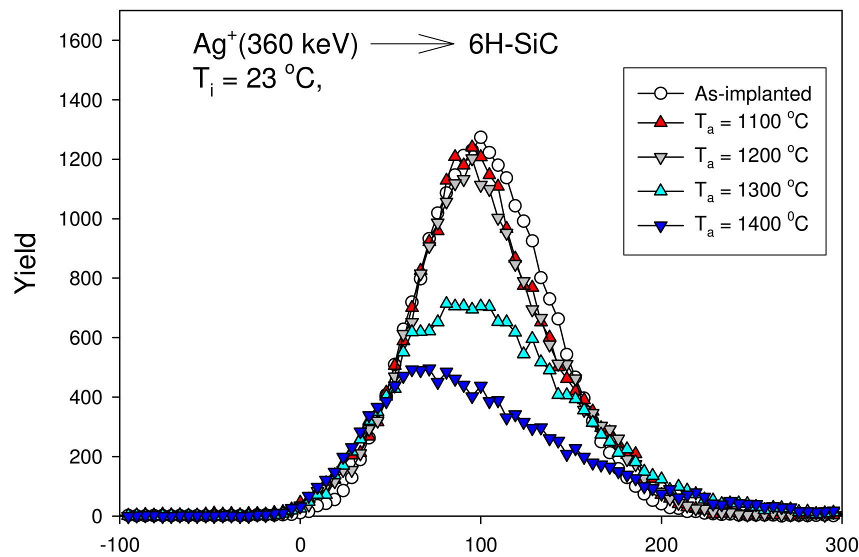

Figure 7-11: Silver depth profiles of 6H-SiC implanted at room temperature after isochronal annealing at 1100 °C, 1200 °C, 1300 °C and 1400 °C for a 10 hours cycle.

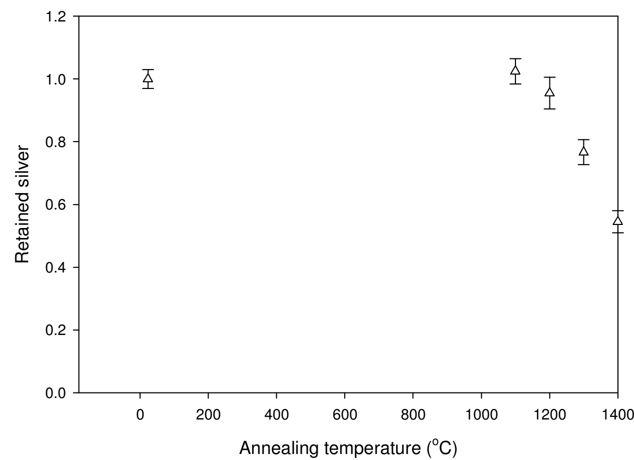

Figure 7-12: Fraction of retained silver in 6H- SiC implanted at room temperature after isochronal annealing at 1100 °C, 1200 °C, 1300 °C and 1400 °C for 10 hours.

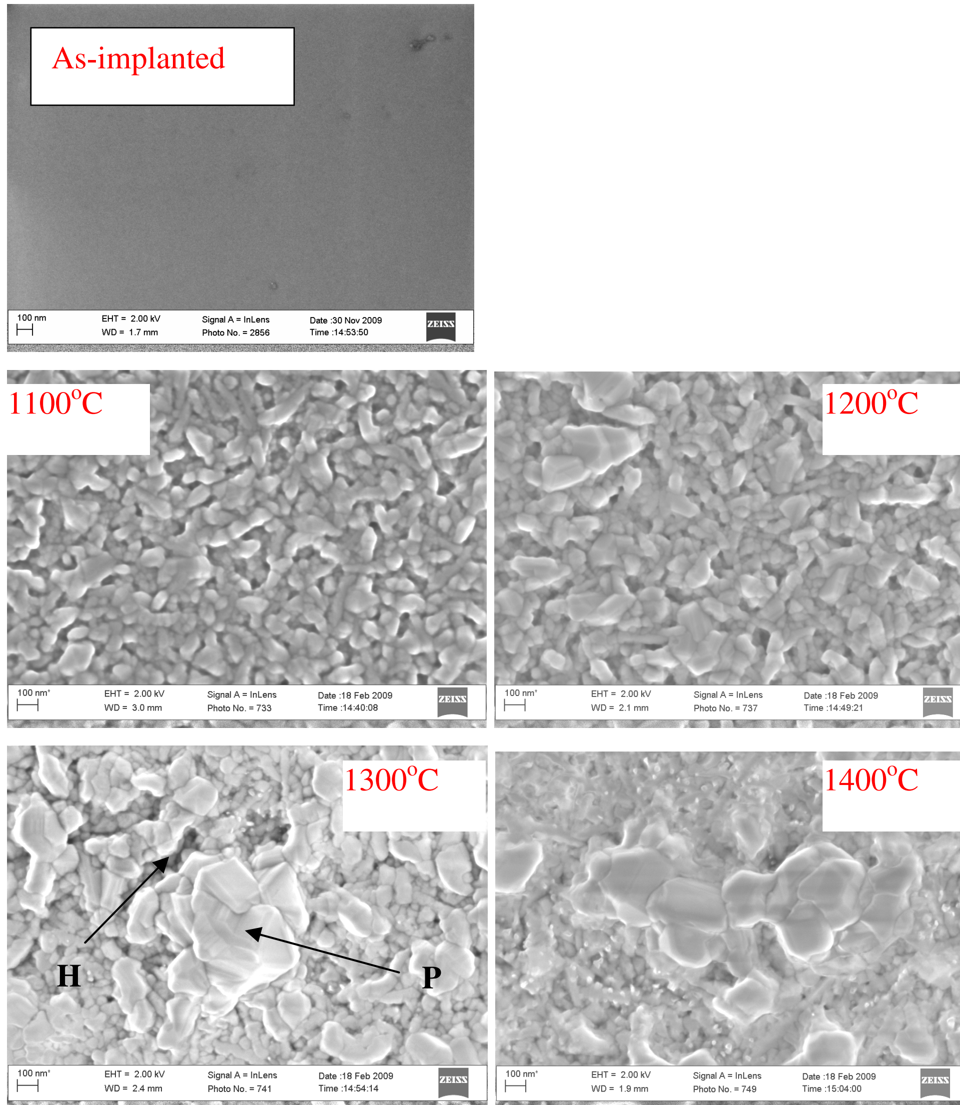

Figure 7-13: SEM images of 6H- SiC implanted at room temperature after isochronal annealing at 1100 °C, 1200 °C, 1300 °C and 1400 °C for 10 hours as compared with as-implanted; the magnification bar is 100 nm in all the images.

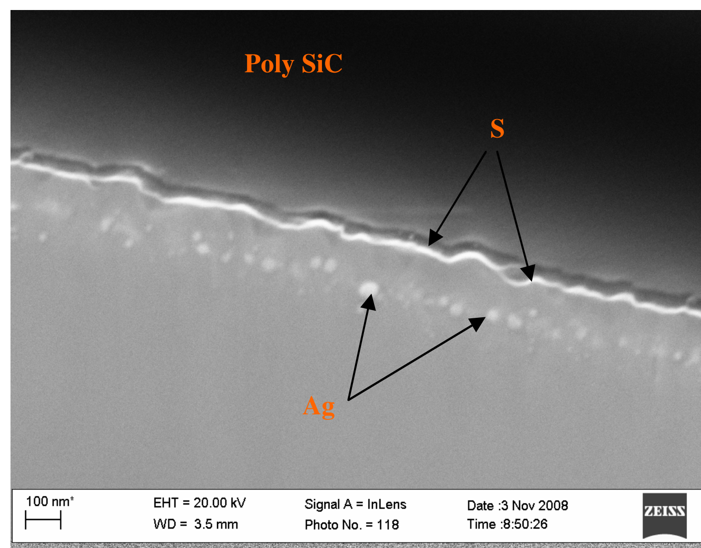

Figure 7-14: The cross sectional image of 6H-SiC implanted with silver at room temperature after annealed at 1250 °C for 30 minutes. This sample is glued to poly-SiC.

The asymmetry of the silver profile at 1400 ^{o}C is due to silver loss from the surface accompanied by diffusion and some changes on the silicon carbide surfaces occurring during annealing as seen in figure 7-13. Figure 7-13 depicts SEM images of samples after isochronal annealing at 1100 ^{o}C, 1200 ^{o}C, 1300 ^{o}C and 1400 ^{o}C for a 10 hours cycle as compared to an as-implanted sample.

The surface of the SiC implanted at room temperature was fairly smooth and amorphous compared to the SiC after annealing as perceived from Figure 7-2 and 7-13. Annealing of the amorphised SiC at 1100 ^{o}C causes the formation of silicon carbide crystals on the surface. These crystals increase in size together with increasing annealing temperature up to 1300 ^{o}C. Some large protrusions (P) also appear at this temperature. Holes (H) are also visible on the silicon carbide surface after annealing. These holes become larger at 1300 ^{o}C where the loss of silver is noticeable. Thus, the silver escapes through these holes, thereby explaining the loss of the implanted silver through the surface without showing the expected diffusion broadening of the implanted profile. (Note that the projected range of the implanted silver is approximately 100 nm – the size of the scale bar in the SEM images.) At 1400 ^{o}C, the larger protrusions are thermally etched and the implanted silver becomes closer to the surface (figure 7-11). This thermal etching could explain the shift of silver towards the surface at 1400 ^{o}C (figure 7-11) and at 1500 ^{o}C (figure 7-10). The discrepancy in broadening of silver peak and silver lost between the two results, i.e. those in figure 7-10 and figure 7-11, is caused by the conditions of the annealing experiments as explained earlier in this section. For the figure 7-10 results the sample was no longer amorphous during annealing at higher temperatures while in the results of figure 7-11 the samples were amorphous during annealing at all the temperatures.

To further investigate the diffusion of silver in 6H-SiC implanted at room temperature, a temperature of 1300 ^{o}C was chosen for the isothermal annealing investigation because the rate of profile broadening was reasonably large and silver loss (less than 30%) from the surface was still acceptable. Silver profiles and their measured widths after annealing between 10 to 80 hours are depicted in figures 7-15 and 7-16. An increase of the width of the silver profile occurred after the first annealing cycle of 10 hours. Further annealing did not alter the width of the silver profile any further. This indicates that the diffusion of silver only took place during

the initial stages of annealing. This could be due to radiation damage-induced diffusion, since implantation at room temperature resulted in the silver being initially embedded in amorphous SiC. The fact that the measured widths remain constant for annealing times longer than 10 hours at 1300 ^{o}C suggests that the amorphous state which allows diffusion of silver is no longer available. This seems to contradict the channelling results which indicate that the damage density was the same as that in the initial amorphous layer (see figure 7-5). However, if the amorphous SiC layer is annealed during this first annealing cycle to form small crystals or crystallites that are randomly orientated or misorientated to the substrate, the channelling spectrum will be similar to that of an amorphous layer. The silver diffusion mechanism will nevertheless alter dramatically between these two substrates, thereby explaining the above results. This explanation is fully supported by the Raman results (see figure 7-6) and is in line with the asymmetric shape of the room temperature implanted silver profile after annealing at 1400 ^{o}C, compared to the symmetric profiles obtained after annealing for 10 h at much higher temperatures, viz. 1500 and 1600 ^{o}C: see Figure 7-10. The asymmetric RBS profile of the sample annealed at 1400 ^{o}C (see Figure 7-11) is caused by silver loss accompanied by diffusion in amorphous SiC since the sample was directly annealed at this temperature while the symmetric profiles at 1500 and 1600 ^{o}C are due to the fact that the sample was sequentially annealed from lower temperatures. This hinders diffusion of silver at these higher temperatures as explained in the section above. At the higher annealing temperatures there is a substantial loss of silver from the SiC substrate through the surface. This will reduce the concentration on the surface side of the silver profile, resulting in a more symmetric profile at these higher temperatures. However, an alternative investigating technique such as TEM is necessary to clarify the nature of the damage after the first annealing step and either prove or disprove this explanation. Based on the RBS and Raman results and the above discussion it can be assumed that this initial diffusion of implanted silver is due to the amorphous SiC layer.

The diffusion coefficient obtained from fitting the experimental data for t > 10 hours to a straight line as a function of time yields an upper limit of: $D < 10^{-21}\ m^2 s^{-1}$ at 1300 ^{o}C, which is in the same range as that obtained by MacLean et al [Mac06], who found a value of $D < 5\times 10^{-21}\ m^2 s^{-1}$ at 1500 ^{o}C.

From the initial slopes of FWHM squares as a function of annealing time, effective diffusion coefficients of silver could be calculated but this would require detailed knowledge of the structural evolution of the SiC during the first annealing cycle (10 hours cycle). Due to the lack of knowledge regarding this evolution the annealing cycle was reduced to obtain the diffusion during the first cycle, thereby avoiding annealing of the radiation damage which would cause silver diffusion to stop.

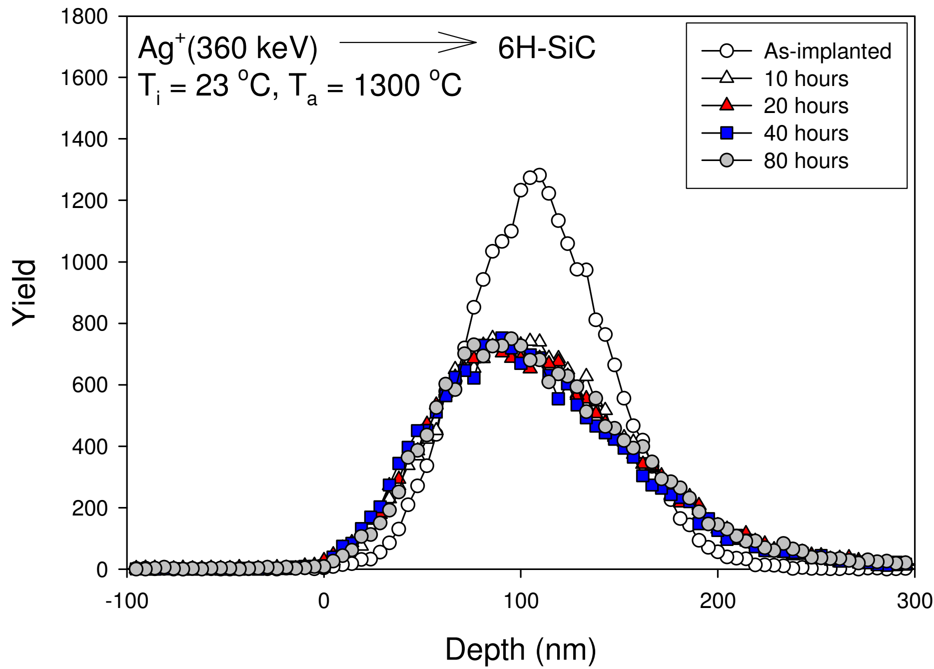

Figure 7-15: Silver depth profiles of 6H-SiC implanted at room temperature after isothermal annealing at 1300 °C for sequential 10 hours cycles up to 80 hours.

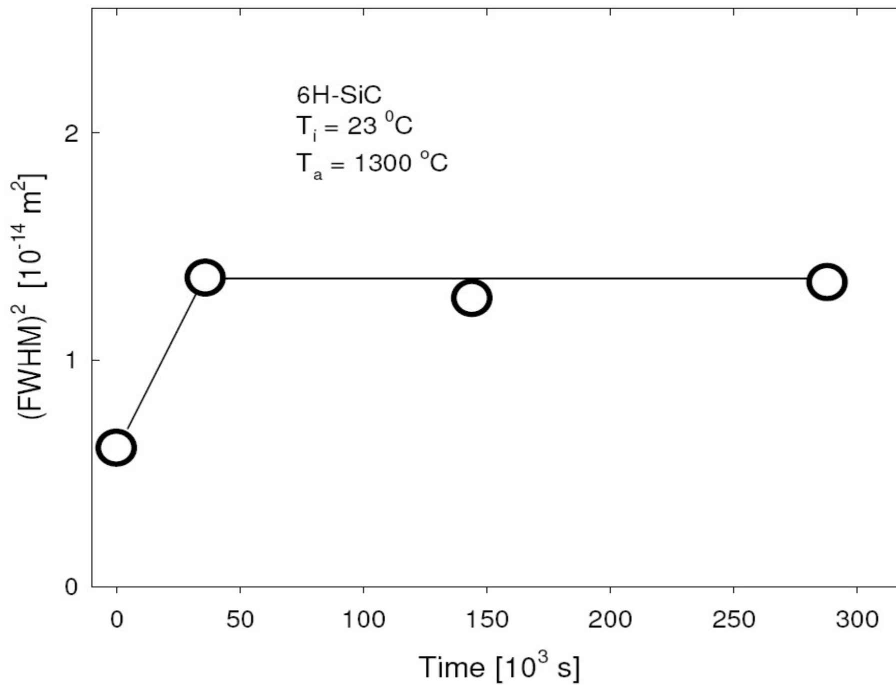

Figure7-16: Square of the full width at half maximum (FWHM) of the silver profile in 6H-SiC as function of isothermal annealing time at Ta=1300 ^{o}C for sequential 10 hours cycles up to 80 hours.

The time at which silver diffusion stops or at which most of the annealing of the damage occurred was investigated by performing an isothermal annealing at 1300 ^{o}C and 1350 ^{o}C for 30 minute cycles up to 120 minutes. The results of the experiments are portrayed in figures 7-17 to 7-19. A relative increase of the FWHM of silver profiles during the first annealing cycles together with a lower increase in width in the second cycles was observed. The sharp increase during the first annealing cycle is without a doubt due to diffusion of the silver in amorphous SiC, while the lower second increase is due to a reduction in the damage, causing less diffusion to occur after the first annealing cycle. For the third cycle the widths at both temperatures remain unchanged, indicating that all the damage which led to the diffusion has been annealed during the first and the second cycles.

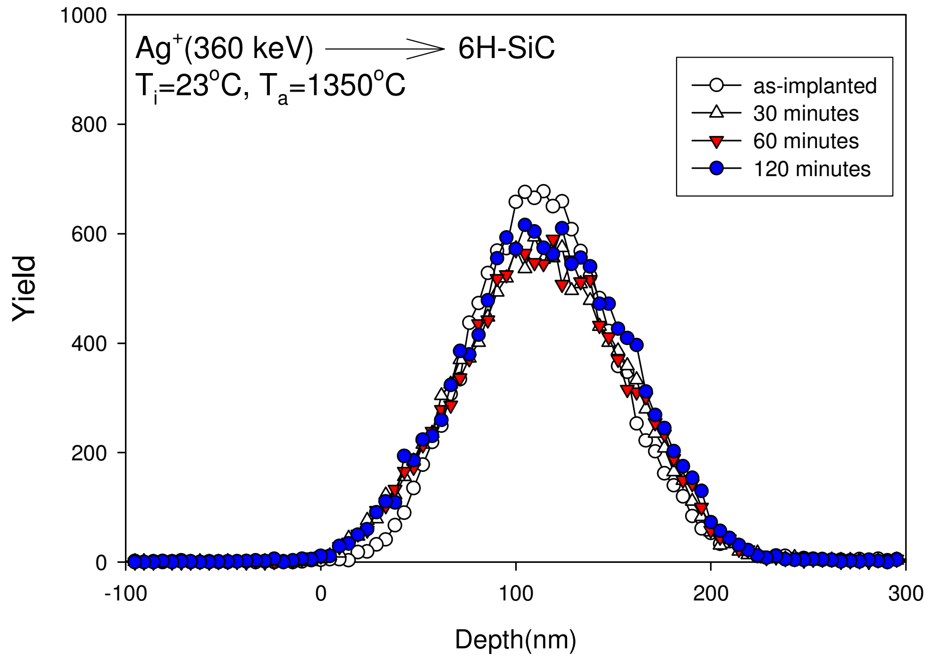

Figure 7-17: Silver depth profiles of 6H-SiC implanted at room temperature after isothermal annealing at 1300 °C for a 30 minutes cycle up to 120 minutes.

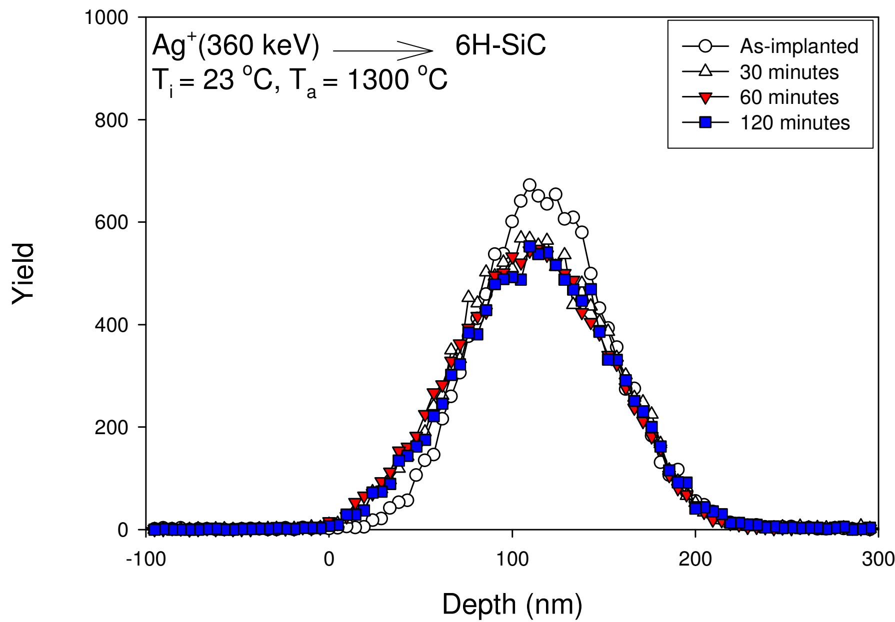

Figure 7-18: Silver depth profiles of 6H-SiC implanted at room temperature after isothermal annealing at 1300 °C for a 30 minutes cycle up to 120 minutes.

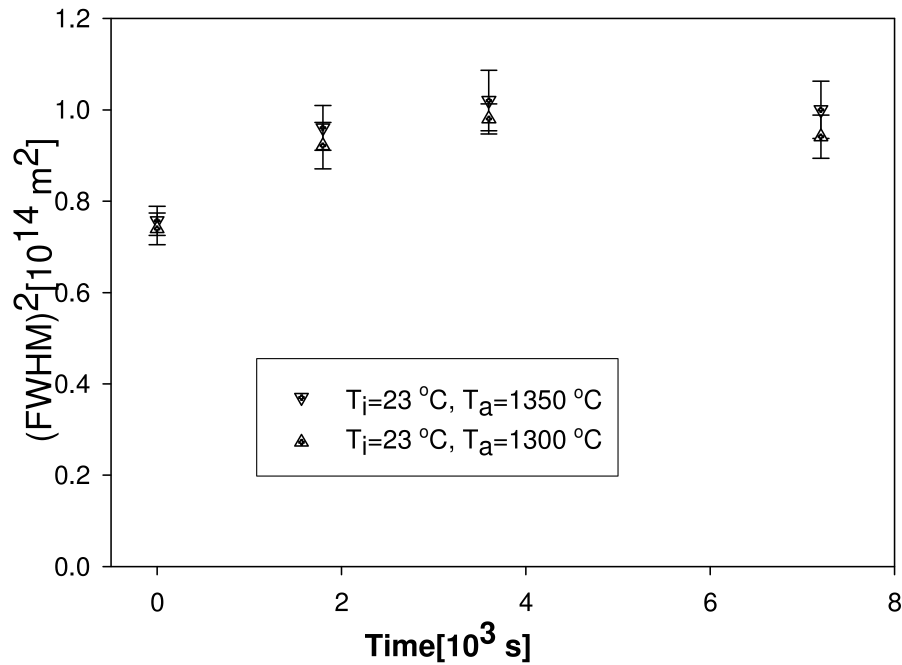

Figure 7-19: Square of the full width at half maximum (FWHM) of the silver profile in 6H-SiC as function of isothermal annealing time (30 minutes) at Ta=1300 °C and 1350 °C.

We have investigated silver diffusion in amorphous SiC for the temperatures where diffusion occurs, viz. between 1300 °C and 1400 °C. This has been carried out by annealing the as-implanted 6H-SiC samples (implanted at room temperature) at 1300 °C, 1315 °C, 1325 °C, 1350 °C, 1365 °C, 1375 °C and 1385 °C for 30 minutes. The silver depth profile results are illustrated in figure 7-20. At these temperatures the profiles are asymmetric due to silver loss accompanied by diffusion. The amount of silver lost during annealing is very small because of the short annealing cycle of 30 minutes. The squares of FWHMs as a function of temperature in the selected range i.e. 1300 °C < 1400 °C are portrayed in figure 7-21. Because of the narrow range of temperature and overshooting of oven temperature during annealing at these temperatures, there are large errors in the measurements.

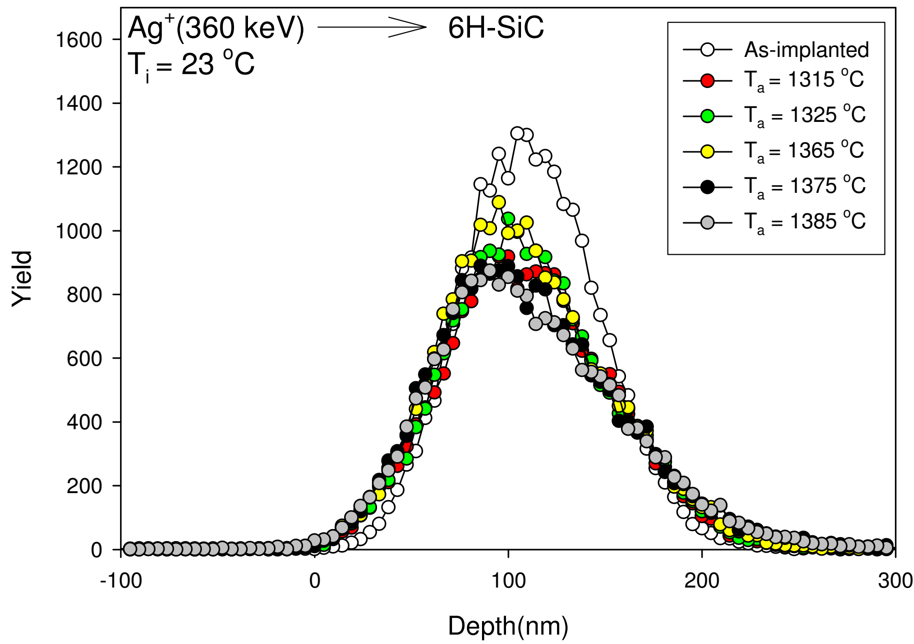

Figure 7-20: Silver depth profiles of 6H-SiC implanted at room temperature after isochronal annealing at 1315 °C, 1325 °C 1365 °C 1375 °C and 1385 °C for a 30 minutes cycle as compared to the as-implanted profile.

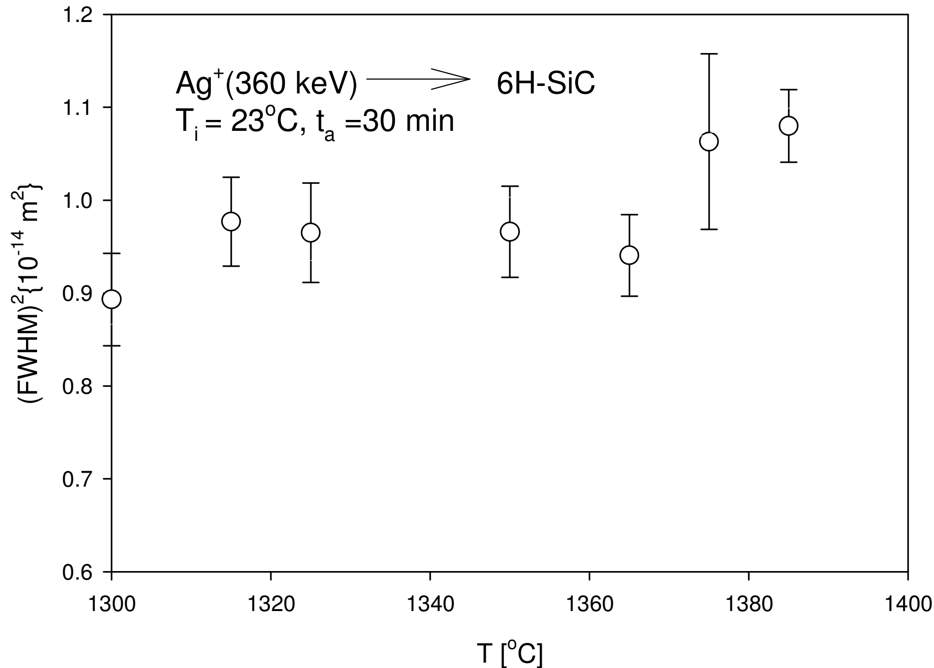

Figure 7-21: Square of the full width at half maximum $(FWHM)^2$ of the silver profile in 6H-SiC as a function of isothermal annealing time (30 minutes) at Ta=1300 °C to 1385 °C.

By comparing the squares of the FWHM of the silver depth profiles after annealing plotted in figure 7-21, with the as-implanted FWHM square, the diffusion coefficients were calculated: they are depicted in figure 7-22. Assuming that the diffusion follows

an Arrhenius type mechanism, the activation energy and pre-exponential factor of silver diffusion in amorphous silicon carbide were determined from an Arrhenius plot. The activation energy E_a and pre-exponential factor (D_o) were calculated from the slope and the y-intercept, respectively. The Arrhenius plot is displayed in figure 7-22. The following values were found: $D_o = 6.6 \times 10^{-12}$ m^2s^{-1} and $E_a = 3.7\times 10^{-19} J$. These are in agreement with the results of silver diffusion in polycrystalline CVD-SiC found by Friedland et al. [Fri09]. These results imply that the diffusion associated with the less dense structure of fully amorphized SiC due to volume swelling is approximately the same as the diffusion of silver via grain boundary diffusion.

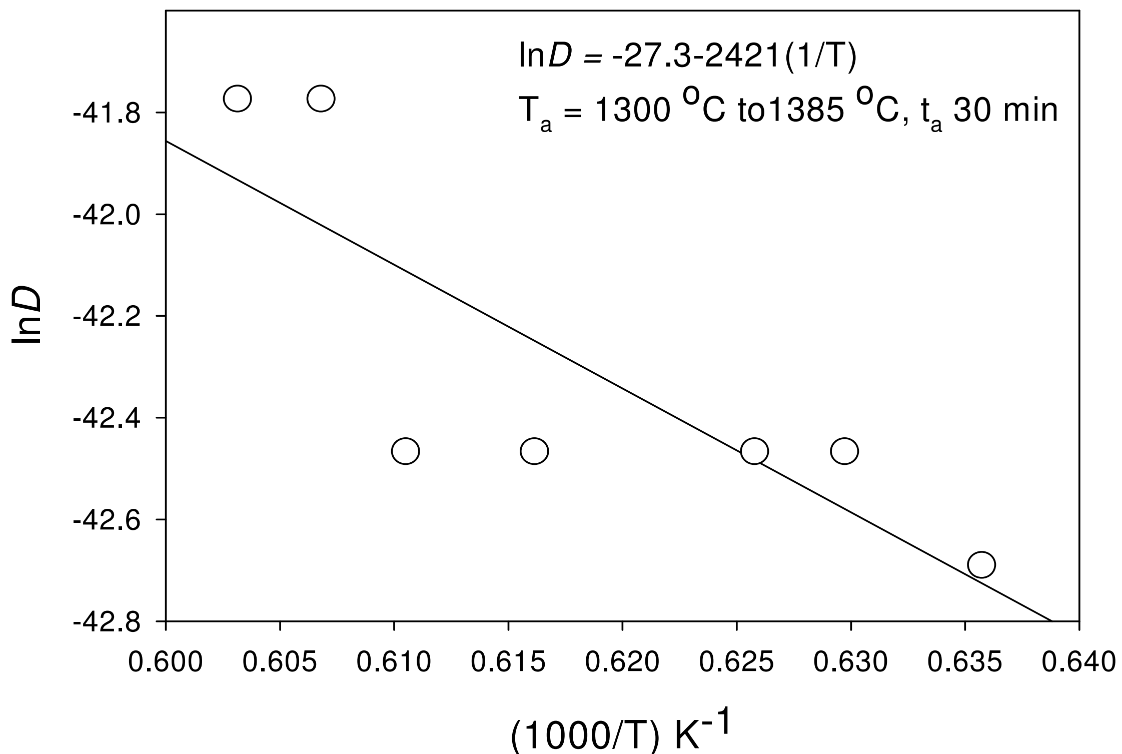

Figure 7-22: Experimental silver diffusion coefficients in amorphous SiC measured in this study from which $D_o = 6.5602 \times 10^{-12}$ m^2s^{-1} and $E_a = 3.69671\times 10^{-19} J$.

Finally, the silver depth profiles collected during the study of annealing of radiation damage by sequential isochronal annealing of the same sample at temperatures between 700 °C and 1600 °C, in 100°C steps, for 30 minutes (subsection 7.2.1.1), also show that diffusion of silver is accompanied by a loss of silver from the surface which

starts at 1300 °C while silver loss begins at lower temperatures (see figures 7-23 to 7-25). The rest of the results are similar to the isochronal results of the 10 hours cycle except that the amount of silver lost at 1300 °C for 30 minutes is less than that at 1300 °C for 10 hours. This is due to the shorter annealing time and the sequential annealing at low temperatures. The silver profiles indicate the decrease in widths at the temperatures below 1300 °C, due to silver forming some precipitates as explained earlier in this section. The silver profile seems to maintain its symmetric shape with the sample annealed at 1400 °C for 30 minutes. This is due to the recrystallization during annealing at the temperatures below 1300 °C for a 30 minutes cycle and the shorter annealing time at 1300 °C since the same sample was sequentially annealed from 700 °C.

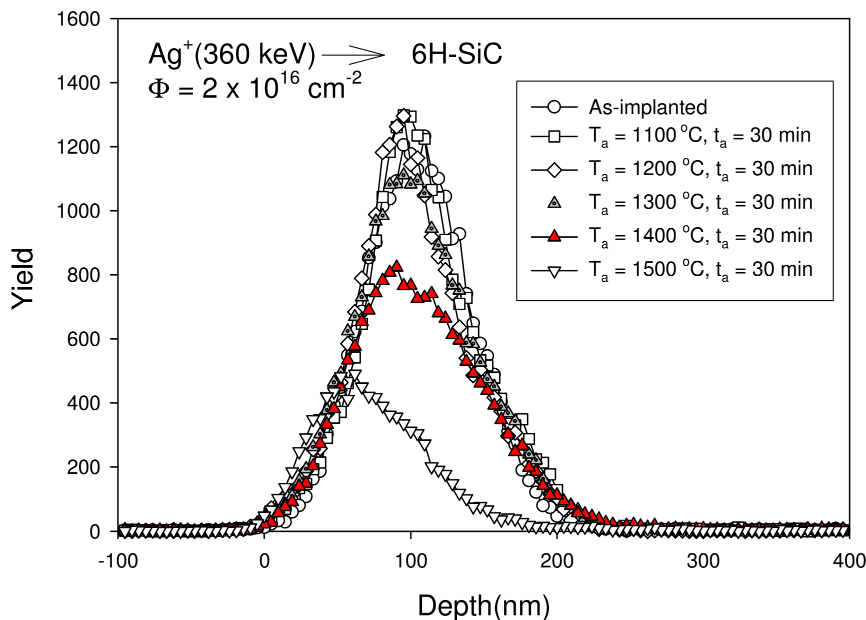

Figure 7-23: Silver depth profiles of 6H-SiC implanted at room temperature after isochronal annealing at 1100 °C, 1200 °C, 1300 °C, 1400 °C and 1500 °C for a 30 minute cycle.

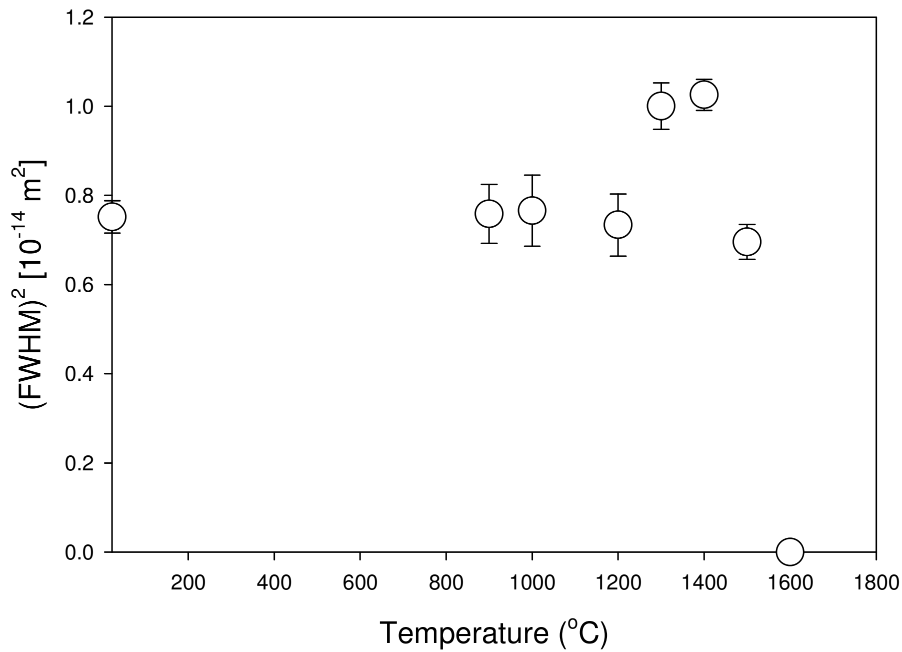

Figure7-24: Square of the full width at half maximum (FWHM) of the silver profile in 6H-SiC as a function of isothermal annealing at temperature 900 °C, 1000 °C, 1200 °C, 1300 °C, 1400 °C, 1500 °C and 1600 °C for 30 minute cycles.

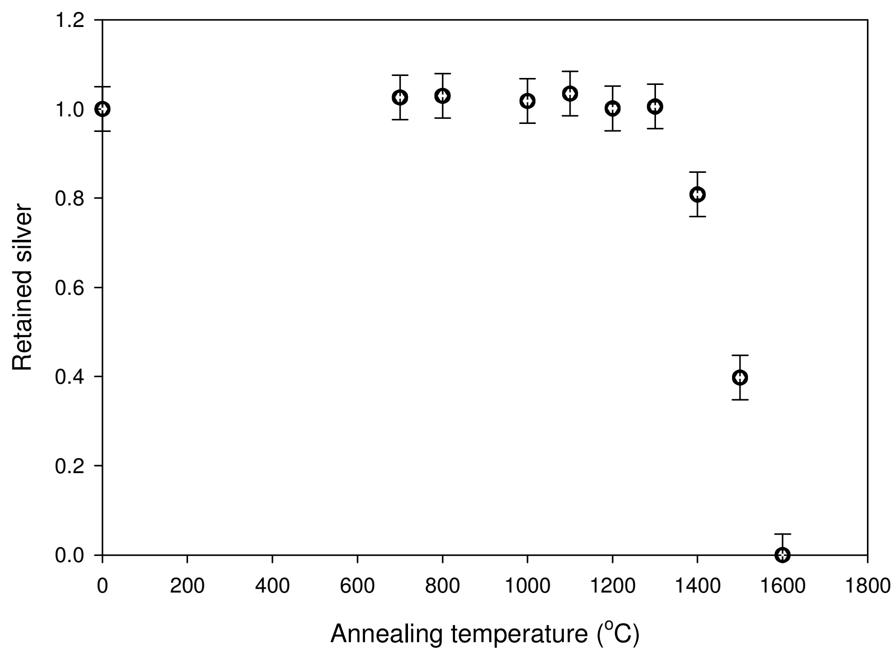

Figure 7-25: Fraction of retained silver in 6H- SiC implanted at room temperature after isochronal annealing at a temperature from 700 °C to 1600 °C for 30 minutes.

7.2.2 HIGH TEMPERATURE IMPLANTATIONS

In this section the results of silver implanted into 6H-SiC at 350 °C and 600 °C are discussed. In subsection 7.2.2.1 the radiation damage results are considered while in subsection 7.2.2.2 the diffusion results are discussed.

7.2.2.1 RADIATION DAMAGE RESULTS

Rutherford Backscattering Spectroscopy combined with channelling of alpha particles was used to examine the annealing of radiation damage of silver implanted in 6H-SiC at 350 °C and 600 °C. These spectra are compared with the spectrum from an unimplanted sample as shown in figure 7-26. Implantation of silver at 600 °C retains crystallinity although distortions occur in the implanted region. This is evident from the broad peak around 180 nm in figure 7-26. This damage peak is deeper than the typical projected range R_p= 102 *nm* of the silver peak measured and that predicted by TRIM 98 R_p= 106*nm*. The damage peak predicted by TRIM 98 is at a depth of about 90 nm (see figure 3.10). The discrepancy has already been explained in subsection 7.2.1.2.

Implantation at 350 °C also retains crystallinity but with more distortions created when compared to silver implanted at 600 °C. This is caused by the fact that at 600 °C, the displaced atoms are more mobile because of their higher thermal energy than at 350 °C. The greater energy increases the probability of the displaced atoms returning to their original lattice sites. These implantation results indicate the irradiation hardness of SiC during implantation at these two temperatures. Similar radiation hardness of SiC above 300 °C has been reported for other heavy ions [Wen98].

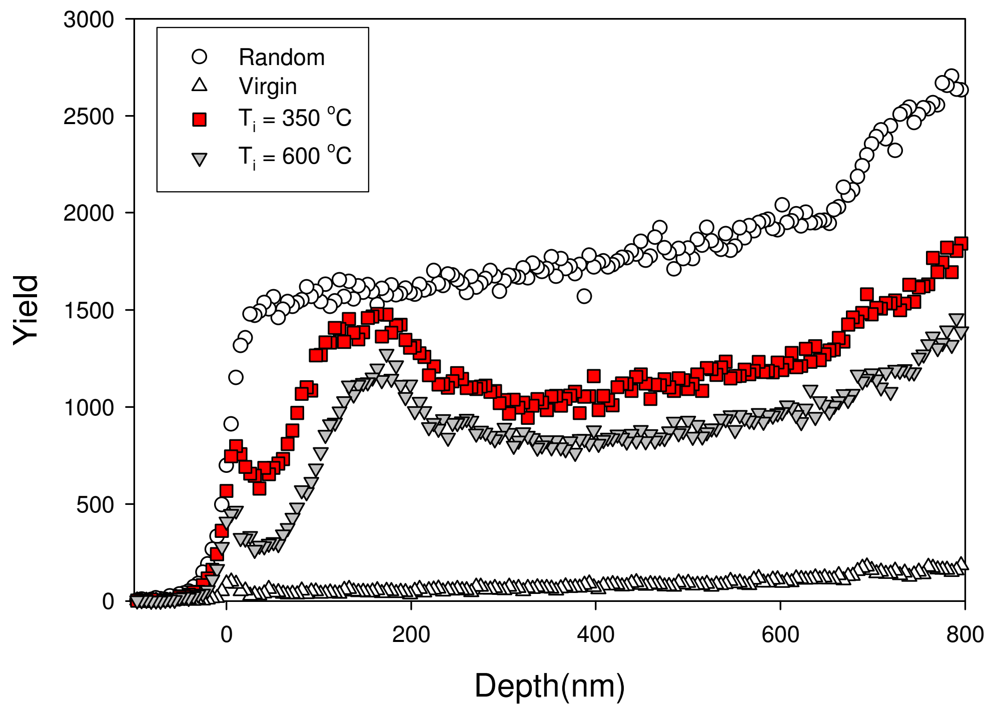

Figure 7-26: Random and aligned backscattering spectra of targets implanted at 350 °C and 600 °C with a fluence of 2×10^{16} $Ag^{+}cm^{-2}$ compared with an unimplanted sample. The α–particles' energy was 1.6 MeV and the scattering angle was 165°.

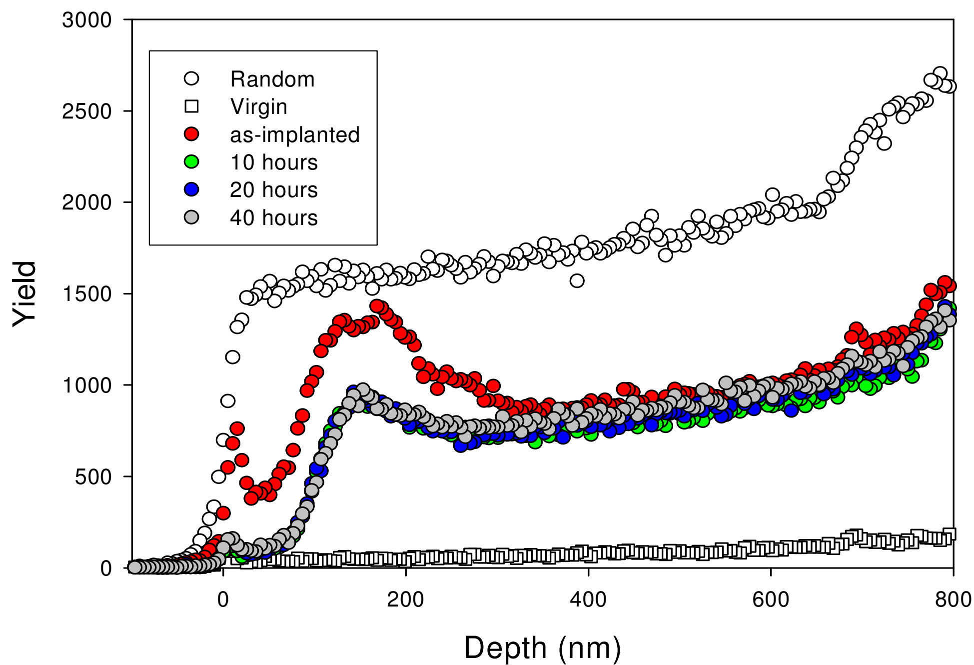

Figure 7-27: Random and aligned backscattering spectra from targets implanted at 350 °C with a fluence of 2×10^{16} $Ag^{+}cm^{-2}$ and subjected to isothermal annealing at 1300 °C for 10 hour cycles up to 40 hours.

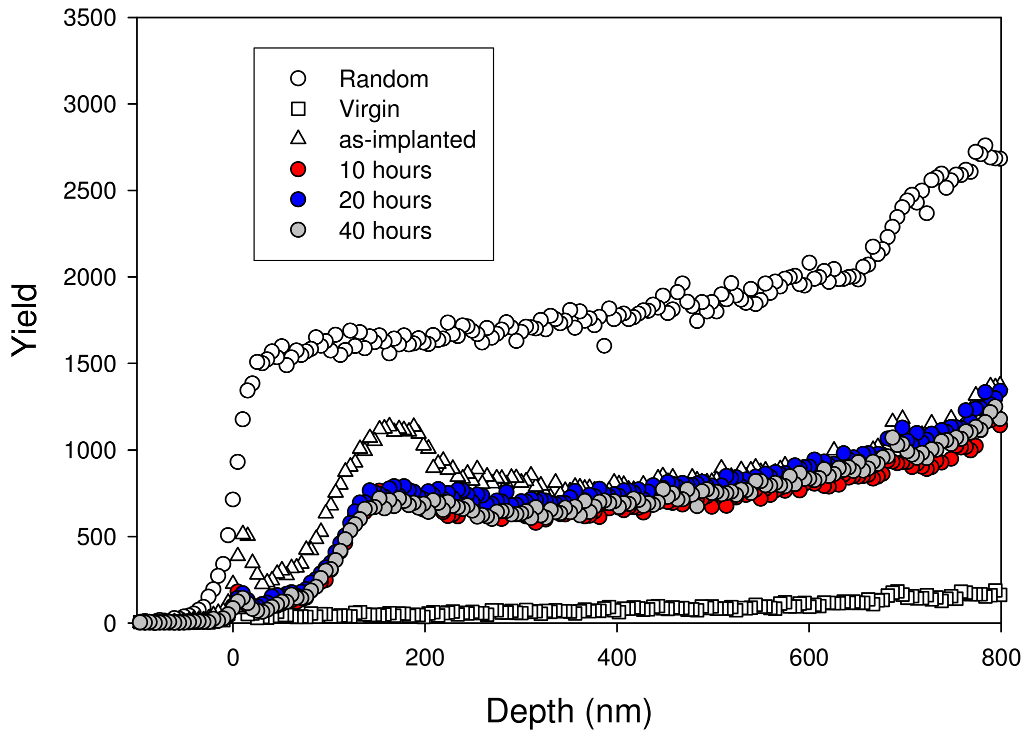

Figure 7-28: Random and aligned backscattering spectra from targets implanted at 600 °C with a fluence of 2×10^{16} Ag^{+}cm^{-2} and subjected to isothermal annealing at 1350 °C for 10 hour cycles up to 40 hours.

Isothermal annealing of samples at 1300 °C for 10 hour cycles up to 40 hours (implanted at 350 °C and at 600 °C) caused some annealing of radiation damage created during implantation but a number of defects remained as shown in figure 7-27 and 7-28. Similar results were observed for isothermal annealing at 1300 °C and 1350 °C for 30 minutes, while isothermal annealing at 1500 °C of the same samples implanted at 600 °C for 30 minutes, 3 hours and 6 hours caused some defect removal as is clear from the reduction of the defect peaks around 180 nm; see figure 7-29. This defect annealing is greater during the first annealing cycle, i.e. 30 minutes (see the damage peak around 180 nm), but defects are still retained after annealing for 6 hours at 1500 °C. This is the result of defects annealing into dislocation networks (during the first annealing cycle) that are very difficult to anneal out during the first annealing cycle.

Our results are in disagreement with the results of Pacaud et al. [Pac96]. Pacaud et al. annealed the highly defective single crystalline of 6H-SiC at 500 °C, 950 °C and

1500 °C for 10 minutes. Their results showed that at 1500 °C all the defects were annealed out. The discrepancy in our results could be explained by the fact that in the case of Pacaud et al. the annealing of defects also took place from the low temperature annealing up to 1500 °C for a shorter period, while in our study it was only the isothermal annealing of the same samples at 1500 °C. Hence in our case the samples experienced the same thermal stresses during cooling to room temperature as in the experiments by Pacaud et al.

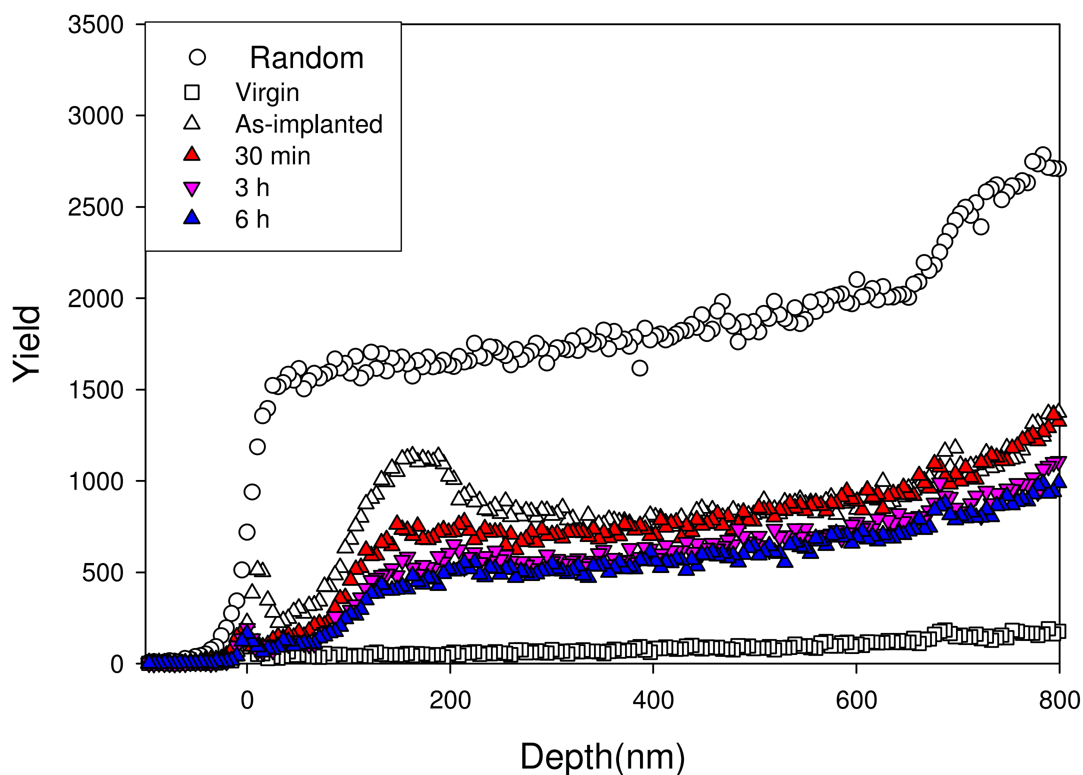

Figure 7-29: Random and aligned backscattering spectra from targets implanted at 600 °C with a fluence of 2×10^{16} $Ag^{+}cm^{-2}$ and submitted to isothermal annealing at 1500 °C for 30 minutes, 3 hours and 6 hours.

7.2.2.2 IMPLANTED LAYER DIFFUSION RESULTS

The typical depth profiles of silver implanted in 6H-SiC at room temperature, 350 °C and 600 °C were compared with TRIM 98 predictions and are shown in figure 7-30. Their moments are as follows: room temperature implantation (R_p = 109 nm σ = 39 nm, β = 2.98, γ = 0.15), 350 °C implantation (R_p = 102 nm, σ = 38.69 nm,

β = 2.83 and γ = 0.42), 600 °C implantation (R_p =102nm, σ = 40.2 nm, β = 3.03 and γ = 0.4) and TRIM98 (R_p =106 nm, σ = 26.78 nm, β = 2.78 nm and γ = 0.069).The projected range of silver implanted at room temperature is 2% deeper compared to those implanted at 350 °C and 600 °C. This is within experimental error and might also be due to the differences in stopping power between amorphous and crystalline SiC. The broader silver peaks in the measurements are due to the reasons discussed in section 7.2.1.2.

The depth profiles of silver implanted in 6H-SiC at 350 °C and at 600 °C after isothermal annealing at 1300 °C for 10 hour cycles up to 40 hours compared to the as-implanted profiles are displayed in figures 7-31 and 7-32. Their corresponding full widths at half maximum square $(FWHM)^2$'s are depicted in figure 7-33 and figure 7-34. From these results it is evident that no detectable diffusion of silver either into the bulk or towards the surface is taking place and that silver loss is almost zero for both samples at this annealing temperature. These results are in agreement with the results of Jiang et al. who found no diffusion of silver in crystalline SiC [Jia04].

The diffusion coefficient obtained from fitting the experimental data (for t_a =10 h to t_a= 40 h) to a straight line yields an upper limit of: $D_{6H} < 10^{-21}\ m^2s^{-1}$ at 1300 °C for 600 °C implanted samples. This result is of the same order of magnitude as the results of MacLean et al. [Mac06], who established an upper limit of: $D < 5\times10^{-21}\ m^2s^{-1}$ at 1500 °C even though our temperature is 200 °C less. This implies that our technique (RBS) exhibits a better depth resolution than the XPS used by MacLean et al. [Mac04]. Hence, if the diffusion coefficient is $D \sim 5\times10^{-21}\ m^2s^{-1}$ our RBS measurements should have detected it.

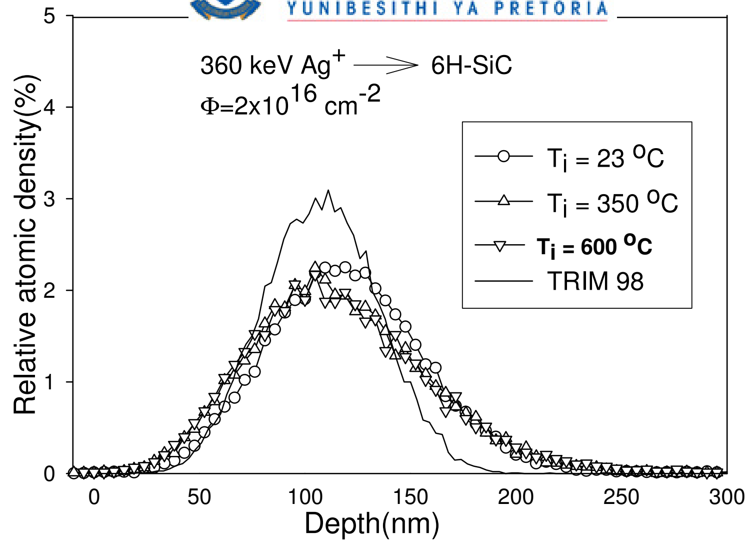

Figure 7-30: Depth profiles of silver implanted in 6H-SiC at room temperature, 350 °C and at 600 °C as compared with TRIM98 prediction.

Isothermal annealing of samples (implanted at 350 °C and 600 °C) at 1300 °C and 1350 °C for 30 minutes up to 120 minutes caused no diffusion of silver as can be observed from figure 7-35 and figure 7-36.

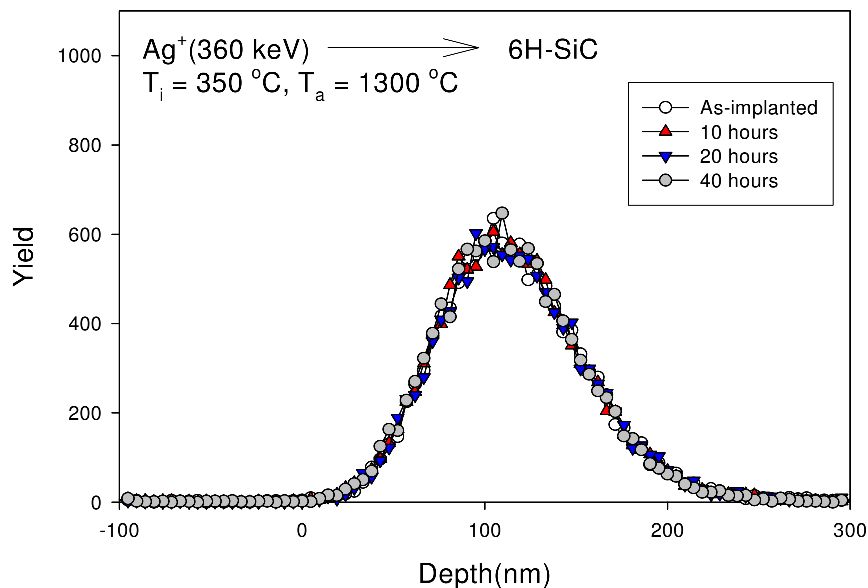

Figure 7-31: Depth profiles of silver implanted in 6H-SiC at 350 °C and isothermally annealed at 1300 °C for a 10 hour cycle up to 40 hours as compared with the as-implanted silver profile.

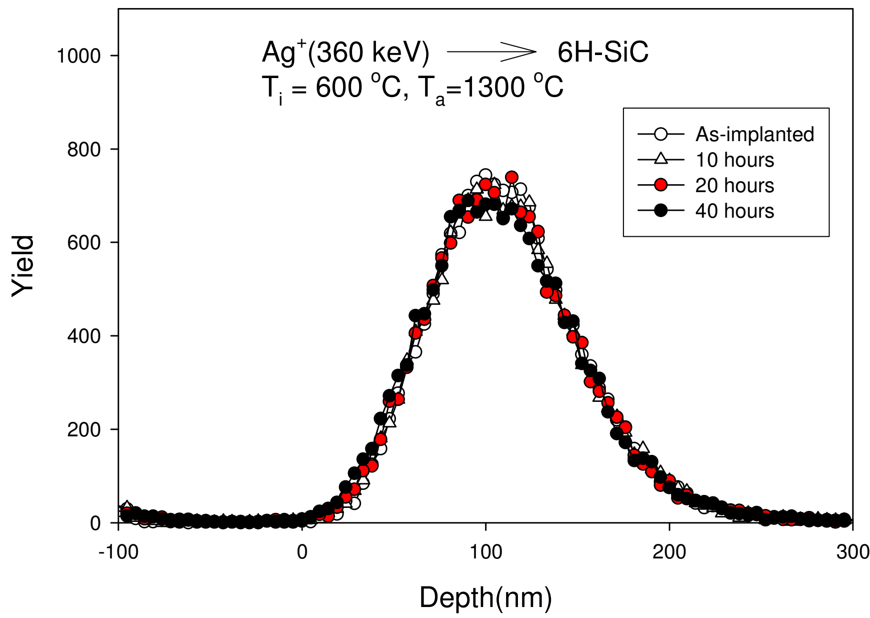

Figure 7-32: Depth profiles of silver implanted in 6H-SiC at 600 °C and isothermally annealed at 1300 °C for a 10 hour cycle up to 40 hours as compared with the as-implanted silver profile.

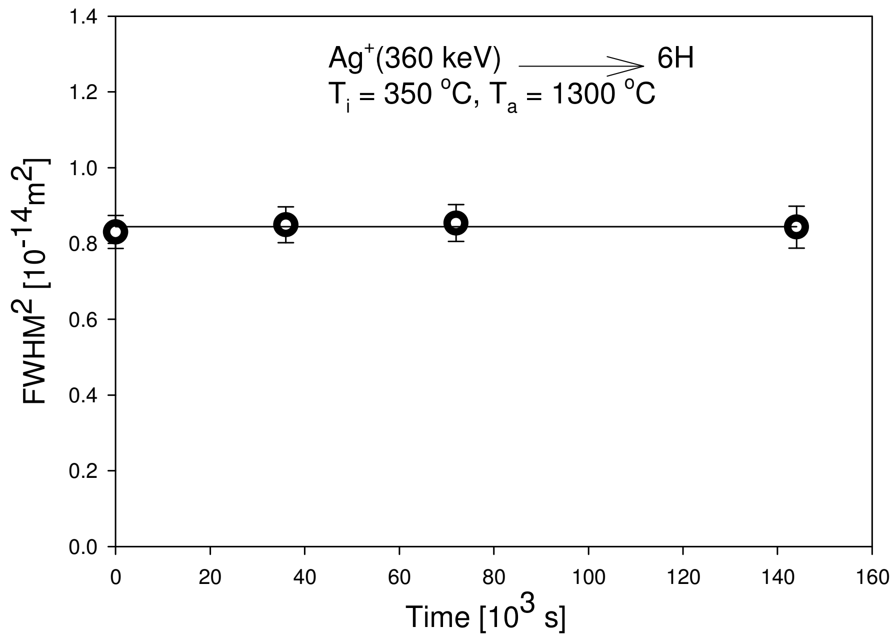

Figure 7-33: Square of the full width at half maximum (FWHM) of the silver profile in 6H-SiC as a function of isothermal annealing time at T_a=1300 °C for a 10 hour cycle up to 40 hours.

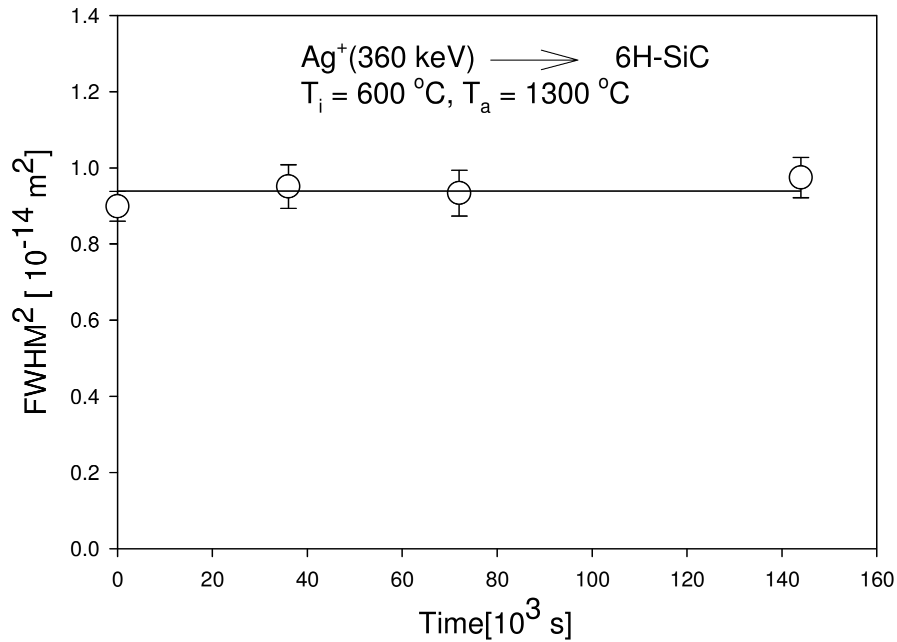

Figure 7-34: Square of the full width at half maximum (FWHM) of the silver profile in 6H-SiC as a function of isothermal annealing time at T_a=1300 °C for a 10 hour cycle up to 40 hours.

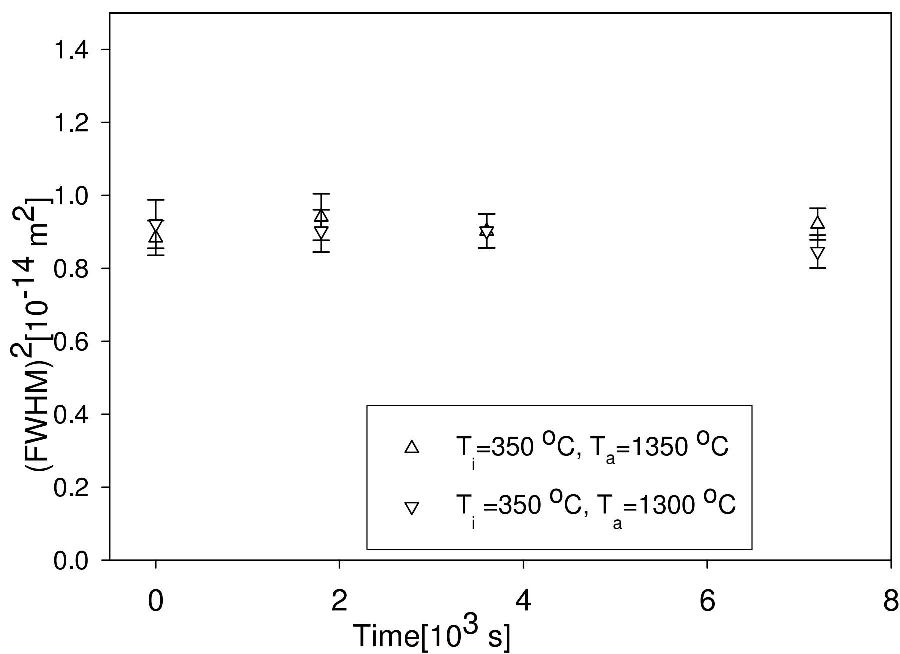

Figure 7-35: Square of the full width at half maximum $(FWHM)^2$ of the silver profiles implanted in 6H-SiC at 350 °C as a function of annealing time at Ta=1300 °C and Ta=1350 °C for a 30 minutes cycle up to 120 minutes.

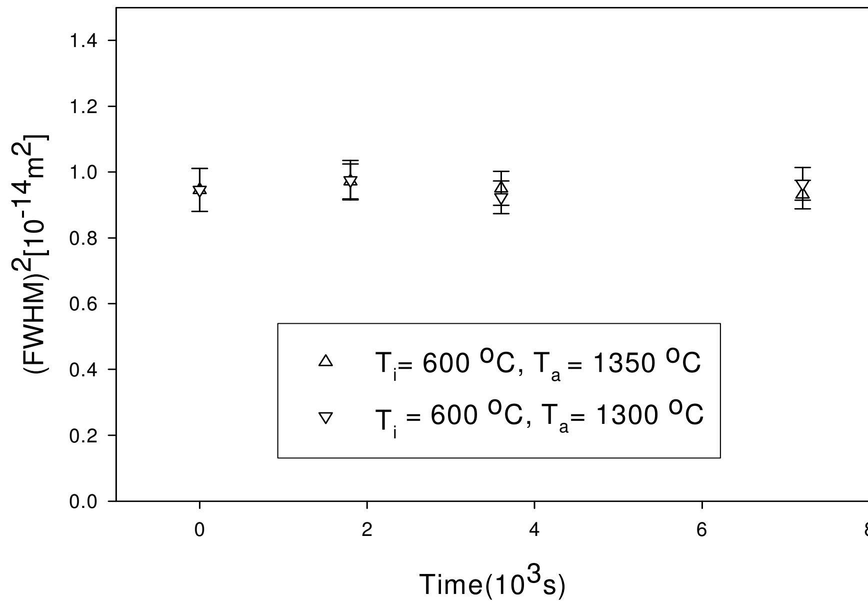

Figure 7-36: Square of the full width at half maximum (FWHM)^2 of the silver profiles implanted in 6H-SiC at 600 °C as a function of annealing time at T_a=1300 °C and T_a=1350 °C for a 30 minute cycle up to 120 minutes.

The immobility and negligible loss of silver at 1300 °C and 1350 °C in the samples implanted at 600 °C allowed further investigation of silver diffusion at temperatures higher than 1300 °C. Isothermal annealing of the sample (implanted at 600 °C) at 1500 °C was performed for different cycles. The results are illustrated in figures 7-37 to 7-40. RBS results showed that annealing at 1500 °C caused no broadening in the silver profiles, but the shift towards the surface was observed for annealing times as short as 30 minutes and was more pronounced at longer annealing times. SEM analyses of the SiC surface indicated the deterioration of the surface, which was probably due to the thermal etching of material during annealing [Cap98][Cap99]. This is evident from the formation of the steps in figure 7-40. These steps indicate that the etching rate is not uniform over the whole surface due to the damage created during implantation. Therefore, the shift of the silver peak towards the surface at 1500 °C is due to thermal etching (see figure 7-37 and figure 7-38). These results also explain the shift of the silver peak towards the surface observed at 1500 °C for 10 hours.

The slope of the silver peak position versus the annealing time (see figure 7-38) is steep during the first annealing cycle, indicating more thermal etching, but reduces as

the annealing cycle lengthens, indicating less thermal etching. This is because of the damage created during implantation, which results in weaker bonds in the SiC, thereby causing atoms to need less energy to escape. The amount of SiC etched was calculated by taking the difference between the as-implanted silver peak position and the silver peak position after annealing. For example, after annealing at 1500 ^oC for 6 hours, about 12 nm of SiC was etched away.

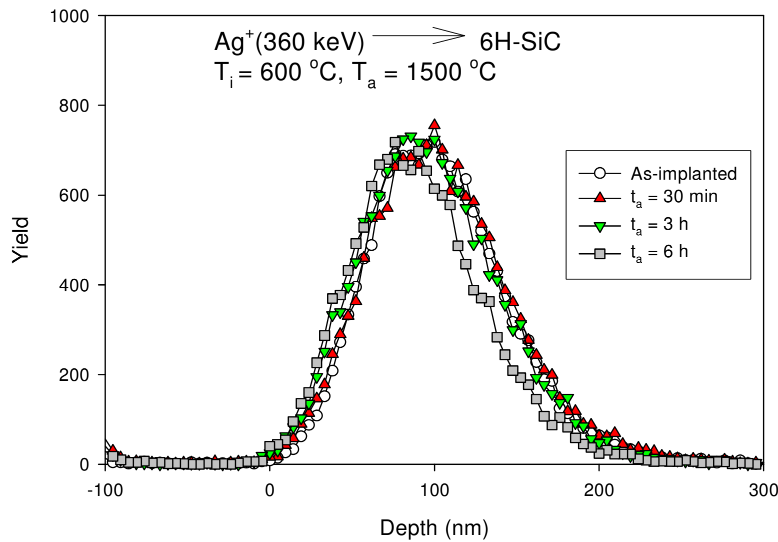

Figure 7-37: Depth profiles of silver implanted in 6H-SiC at 600 ^oC and isothermally annealed at 1500 ^oC from 30 minutes up to 6 hours compared with the as-implanted silver

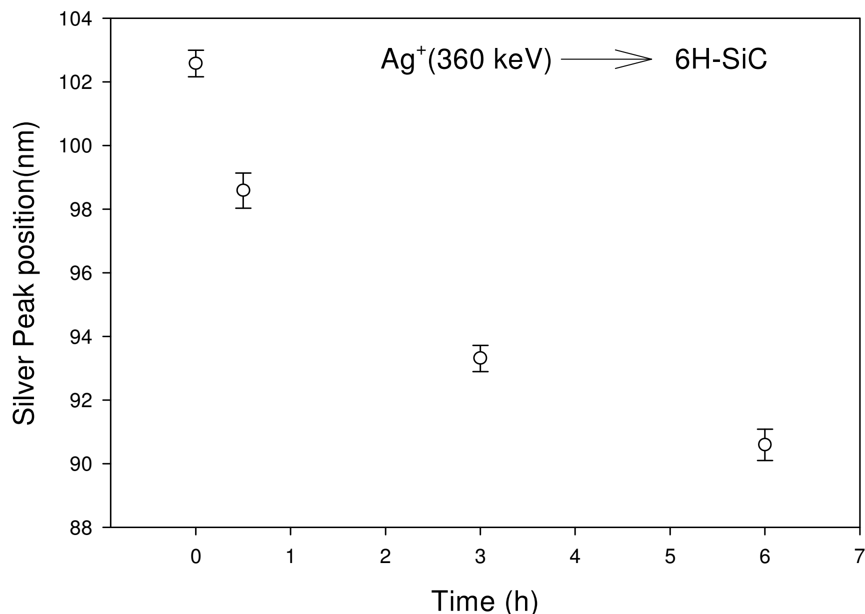

Figure 7-38: Peak position of silver implanted in 6H-SiC at 600 ^oC after isothermal annealing at 1500 ^oC up to 6 hours.

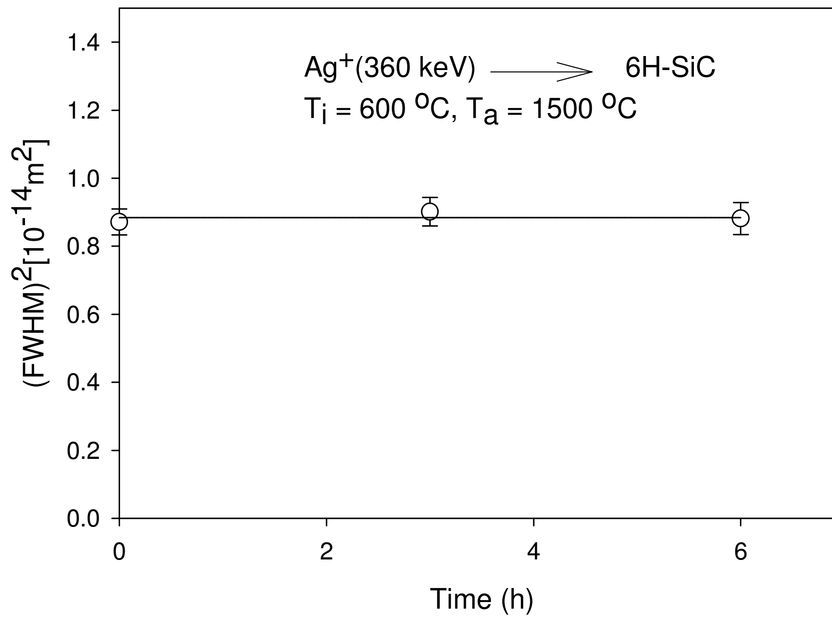

Figure 7-39: Square of the full width at half maximum square $(FWHM)^2$ of the silver profiles implanted in 6H-SiC at 600 ^oC as a function of isothermal annealing time up to 6 hours at Ta = 1500 ^oC.

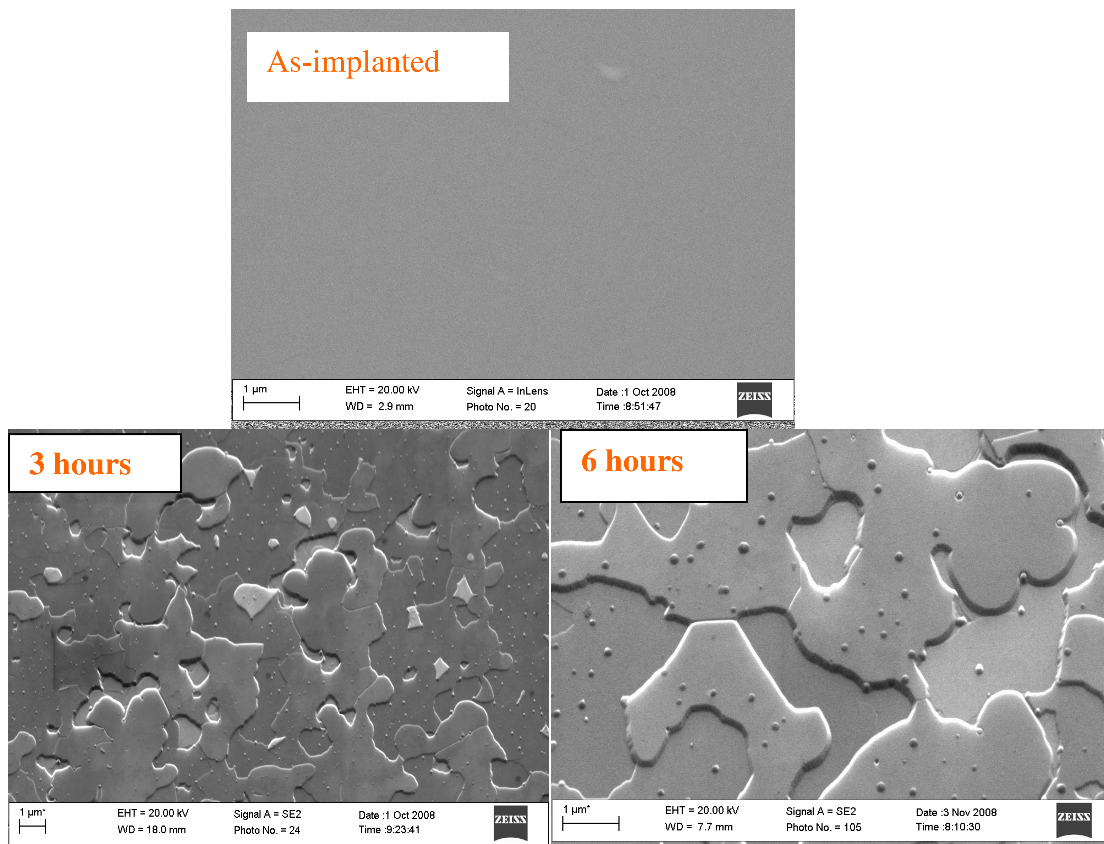

Figure 7-40: SEM images of 6H-SiC implanted at 600 ^oC after isothermal annealing at 1500 ^oC for different annealing cycles up to 6 hours.

7.2.2.3 EFFECT OF NEUTRON IRRADIATION

The effect of neutron irradiation was investigated on the samples implanted at higher temperatures (350 °C and 600 °C). This was performed because no diffusion was observed on these samples. Samples were irradiated by placing them in an experimental nuclear reactor (SAFARI-1) for 278 h, with a neutron flux of 1.46×10^{14} $cm^{-2}s^{-1}$; the reactor power was about 20 MW. The temperature of the samples during irradiation was approximately 300 °C. The samples were found to be radioactive after irradiation while the gamma ray spectrum was found to be that of ^{110m}Ag (see figure 7-41) with a half life of 253 days. ^{110m}Ag resulted from the implanted ^{109}Ag capturing neutrons during irradiation. Before analysing the samples with RBS, the maximum activity was estimated in each sample, by multiplying the maximum activity of ^{110m}Ag which is 4.7×10^{3} Ci/g by the mass of implanted silver. The mass of silver was calculated from the fluence of implanted ^{109}Ag ($2\times10^{16}cm^{-2}$) and the average area of the SiC samples (0.2 cm^2); it was found to be 7.2 $\times10^{-7}$ g. Hence the maximum activity in one sample (A) was established as 3.4 mCi. To limit the exposure time during the RBS measurements, channelling was not performed on post irradiated samples.

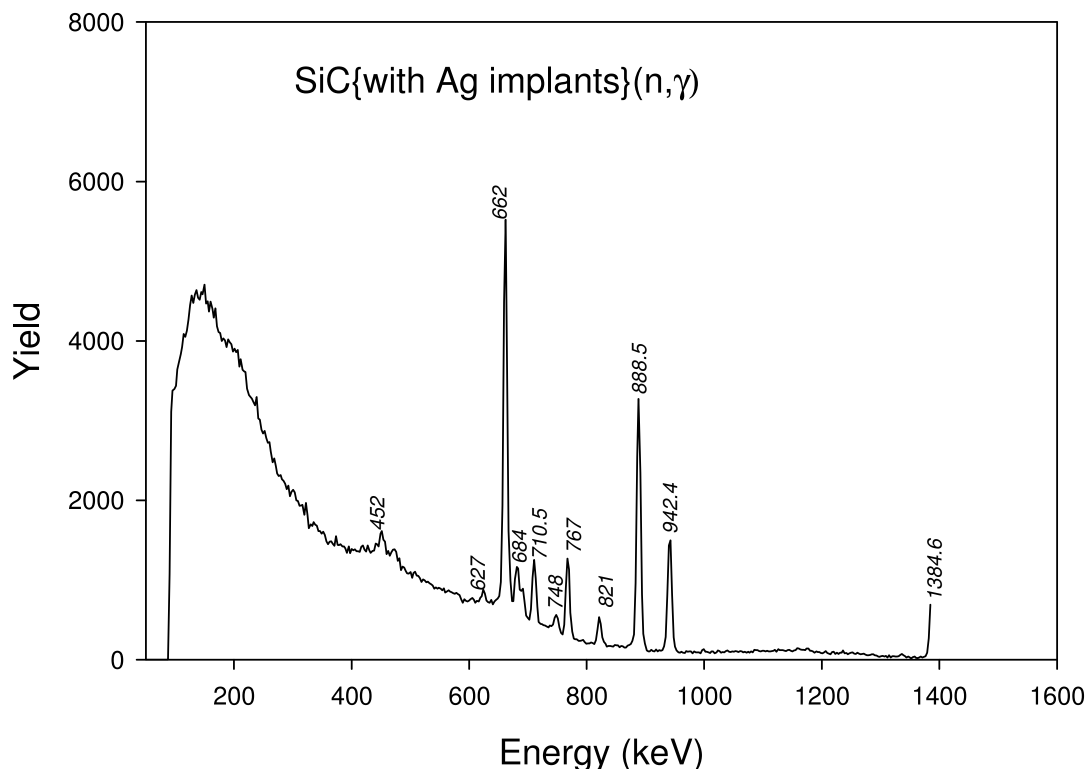

Figure 7-41: Gamma-rays measured on samples implanted with silver at 350 °C and 600 °C after neutron irradiation.

The silver profiles of the neutron irradiated sample which was implanted with Ag at 350 ^{o}C compared with the as-implanted silver profile are illustrated in figure 7-42. The as-implanted silver profile and the silver profile of the neutron irradiated profile are identical because RBS is unable to resolve the difference between ^{109}Ag and ^{110m}Ag. This is caused by the insufficient mass resolution of the RBS at high masses. The identical profiles indicate that neutron irradiation caused no diffusion of silver through SiC at room temperature. Similar results were observed in the samples implanted at 600 ^{o}C. No annealing was performed on these samples because any ^{110m}Ag release would contaminate the furnace which would endanger the personnel involved.

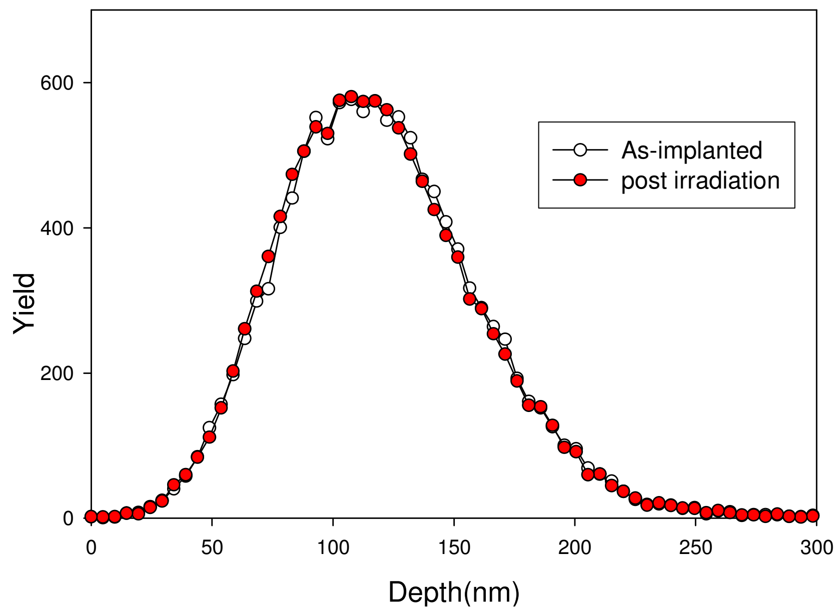

Figure 7-42: Silver depth profiles of the post irradiated SiC implanted (at 350 ^{o}C) compared with the as-implanted profiles.

7.3 REFERENCES

[Boh87] H. G. Bohn, J.M. Williams, C.J. McHargue, G.M. Begun, J. Mat. Res. **2** (1987) 106.

[Cap98] M. A. Capano, S. Ryu, M.R. Melloch, J. A. Jr. Cooper, M. R. Buss, J. Elec. Mat. **27** (1998) 370.

[Cap99] M. A. Capano, S. Ryu, J.A. Jr., Cooper, M. R. Melloch, K. Rottner, S. Karlsson, et al. J. Elec. Mat. **28** (1999) 214.

[Fel68] D.W. Feldmann, J. H. Parker, W. J. Choyke, L. Patrick, Phys. Rev. **170** (1968) 698.

[Fen99] Z. C. Feng, S. T. Chua, K. Tone, J. H. Zhao, Appl. Phys. Lett. 75 (199) 472

[Fri09] E. Friedland, J.B. Malherbe, N.G. van der Berg , T. Hlatshwayo, A.J. Botha, E. Wendler , W. Wesch, J.Nucl.Mat. **389** (2009) 326.

[Jia04] W. Jiang, W.J. Weber, V. Shutthanandan, L. Li, S. Thevuthasan, Nucl. Instr. and Meth. **219/220** (2004) 642.

[Mac06] H.J. MacLean, R.G. Ballinger, L.E. Kolaya, S.A. Simonson, N. Lewis, M.E. Hanson, J. Nucl. Mater. **357** (2006) 31.

[Nab77] H. Nabielek, P.E. Brown, P. Offermann, Nucl. Tech. **35** (1977) 483.

[Nak02] T. Nakamura, S. Matsumoto and M. Satoh, J. Cryst. Grow. **237-239** (2002) 1264.

[Pac96] Y. Pacaud, J. Stoemenos, G. Brauer, R.A. Yonkov, V. Heera, M. Voelskow, R. Kögler, W. Skorupa, Nucl. Instr. and Meth. **B120** (1996) 177.

[Rao03] M. V. Rao, Solid-State Electronics, **47** (2003) 213.

[Shu69] F.A. Shunk, *Constitution of Binary Alloys,* McGraw-Hill Company, New York (1969).

[Tes95] J. R. Tesmer, M. Nastasi, Handbook of Modern Ion Beam Materials Analysis, Mat. Res. Soc. Pittsburgh, Pennsylvania (1995)

[Wen98] E. Wendler, A. Heft, W. Wesch, Nucl. Instr. and Meth. **B141** (1998) 105.

CHAPTER 8 SUMMARY OF RESULTS

The following topics: in-diffusion, radiation enhanced diffusion of silver, retained radiation damage and annealing of radiation damage in single crystalline 6H-SiC were investigated by RBS, RBS-C and SEM. For in-diffusion investigation two methods were used. In the first, thin silver films (100 nm) were deposited onto the samples followed by annealing while in the second, the samples with silver thin films deposited on their surface were encapsulated followed by annealing. For investigations into radiation enhanced diffusion of silver, retained damage and annealing of radiation damage, silver was implanted into samples at room temperature, 350 ^{o}C and 600 ^{o}C followed by subsequent annealing. This chapter summarises the results of this study.

8.1 SILVER IN-DIFFUSION RESULTS

In-diffusion of silver into 6H-SiC was first investigated at a temperature below the melting point of silver (960 ^{o}C) using un-encapsulated 6H-SiC samples with 100 nm deposited silver. No silver in-diffusion was observed at 800 ^{o}C but disappearance of silver occurred at this temperature. For the encapsulated samples, no in-diffusion of silver was observed at 800 ^{o}C, 900 ^{o}C and 1000 ^{o}C but silver disappeared from the samples' surfaces and was found on the walls of the quartz glass ampoule. The disappearance of the silver layer from the SiC surface was investigated at temperatures from 200 ^{o}C to 700 ^{o}C in steps of 100 ^{o}C. This phenomenon was found to be due to the wetting problem between silver and SiC.

8.2 ROOM TEMPERATURE IMPLANTATION

Radiation enhanced diffusion in 6H-SiC was investigated after silver implantation at room temperature by studies of annealing at temperatures from below the melting point (960 ^{o}C) of silver up to 1600 ^{o}C. This was performed by both isochronal annealing and isothermal annealing. The radiation enhanced diffusion was observed by comparing the FWHM of silver implanted depth profiles at different temperatures with those of the post annealing samples.

The room temperature implantation resulted in a completely amorphous surface layer of approximately 270 nm thick. Epitaxial re-growth from the bulk was already taking place during annealing at 700 ^{o}C and the crystalline structure seemed to be fully recovered at 1600 ^{o}C, as regards samples that were sequentially isochronally annealed from 700 ^{o}C in steps of 100 ^{o}C up to 1600 ^{o}C. However, no silver signal was detected at this temperature which left some doubts as to the crystalline structure of the samples at this temperature. It was speculated to be due to thermal etching of the top original amorphous layer while the damage consisted of epitaxial re-growth from the bulk. The decomposition of SiC, giving rise to carbon peaks in the RBS spectra due to the evaporation of Si, was clearly observed on the same samples at 1600 ^{o}C. Isothermal annealing at 1300 ^{o}C for 10 h cycles up to 80 h caused epixatial re-growth from the bulk during the first annealing cycle (10 h). No further epitaxial re-growth from the bulk was observed up to 80 h. This was believed to be due to the amorphous layer re-crystallising into crystals that were randomly oriented to the 6H-SiC. These crystals could be other crystalline forms of SiC such as 3C, 4H, etc. These results were confirmed by Raman spectroscopy but transmission electron microscopy is necessary to further confirm them.

No diffusion of silver was observed at temperatures below 1300 ^{o}C but silver seemed to form precipitates at these temperatures. Diffusion of silver towards the surface accompanied by silver loss from the surface began at 1300 ^{o}C and was very high at 1400 ^{o}C, with silver profiles becoming asymmetric and closer to the surface. The loss of silver was already taking place at 1100 ^{o}C. By means of SEM and RBS analyses, silver loss was found to be due to the following:

- Diffusion of silver towards the surface.
- The mass flow of silver via holes that were observed to be growing larger with higher annealing temperatures on SiC surfaces.
- Thermal etching of SiC.

Isothermal annealing at 1300 ^{o}C for 10 h up to 80 h caused diffusion of silver during the first annealing cycle whereas no further diffusion was observed for any further annealing at the same temperature up to 80 h. The diffusion coefficient was not calculated due to the lack of information on the structural evolution of SiC during the first annealing cycle. Isothermal annealing at 1300 ^{o}C and 1350 ^{o}C for 30 minute

cycles up to 120 minutes caused high diffusion during the first cycle and reduced diffusion during the second cycle, while no diffusion was observed for any further annealing longer than the second cycle. The higher diffusion during the first 30 minutes was due to ion induced amorphazation. The diffusion of silver in the amorphised SiC was measured at different temperatures in the range 1300 ºC to 1385 ºC and yielded to $D_o \sim 1.4 \times 10^{-12}$ m^{2}s^{-1} and $E_a \sim 3.3 \times 10^{-19}$ J. These values were found to be approximately the same as the values of silver diffusion in polycrystalline CVD-grown SiC found by our group, stemming from grain boundary diffusion: $D_o \sim 4\times10^{-12}$ m^2 s^{-1} and $E_a \sim 4\times10^{-19}$ J.

To clearly understand silver diffusion in 6H-SiC especially in the amorphised 6H-SiC, the following still need to be further investigated.

- The diffusion of silver in the amorphised 6H-SiC allows further in-diffusion studies of silver into amorphised 6H-SiC. This would be carried out by performing encapsulated in-diffusion experiments in the amorphised 6H-SiC that is available. If these experiments succeed, the same experiments will be performed on the 6H-SiC amorphised by Si implantation to reduce the complication of measuring the diffusing silver. Since there will be no implanted silver in the amorphous 6H-SiC, it will be easier to measure the silver that is present in-diffusion to amorphised 6H-SiC.
- The annealing of amorphised 6H-SiC after the first cycle needs to be further investigated by Transmission Electron Microscopy (TEM) to verify our suggestion that amorphous SiC re-crystallizes into other SiC polytypes such as 3C-SiC.

8.3 HIGH TEMPERATURE IMPLANTATIONS

Implantation of silver at 600 ºC retained crystallinity, although distortions occurred in the implanted region, while implantation at 350 ºC also retained crystallinity, but a larger number of distortions occurred as compared to silver implanted at 600 ºC. This was caused by the fact that, at 600 ºC, the displaced atoms were more mobile because of their higher thermal energy than at 350 ºC. The greater energy increased the probability that the displaced atoms would combine with their original lattice sites. Annealing of these samples at 1300 ºC, 1350 ºC and 1500 ºC caused some annihilation of defects but a number of defects were retained.

No diffusion of silver was observed during annealing of the samples (implanted at 350 ^{o}C and at 600 ^{o}C) at 1300 ^{o}C, 1350 ^{o}C and 1500 ^{o}C but silver moved towards the surface at 1500 ^{o}C. The upper limit of diffusion coefficient of $D<10^{-21}\ m^2s^{-1}$ was obtained at 1300 ^{o}C which was of the same order of magnitude as results found in literature at 1500 ^{o}C: $D< 5\times10^{-21}\ m^2s^{-1}$, even though our temperature was 200 ^{o}C less. This indicates that our RBS has a better resolution than XPS. The movement of silver towards the surface was found to be due to thermal etching at 1500 ^{o}C. Neutron irradiation of these samples caused no silver diffusion but silver ^{110m}Ag due to ^{109}Ag capturing a neutron during neutron irradiation was detected in the samples. No annealing was performed on neutron irradiated samples, to reduce the chances of contaminating the oven with radio-active isotopes of silver with a long half-life and the danger of high doses of gamma-rays for subsequent users.

CHAPTER 9 APPENDIX A

Annealing is a process where material is heated to a particular temperature for a particular time, which alters the material's microstructure, thus changing its properties. Since some of the material is sublimated during annealing, it is important to know the relationship between the produced vapour pressure of material and annealing temperature so as to be able to predict the amount of material needed for annealing at a particular temperature. If encapsulation experiments are performed, the state where the amount of atoms sublimated is equal to the amount of atoms condensing is sometimes reached. This state is reached when the vapour pressure has reached a state of equilibrium; the vapour pressure at that state is termed equilibrium vapour pressure. Therefore, for encapsulation experiments the amount of atoms leaving the sample and condensing on the sample can be estimated from the equilibrium vapour pressure at a particular temperature. In this section the relationship between temperature and equilibrium vapour pressure is derived.

In doing so we consider a system *A* which is in thermal contact with a heat reservoir (system *A'*) at constant temperature T_0 and constant pressure p_0. The combined system $A^0=A+A'$ is depicted in figure A 1-1. System A is under vacuum and at room temperature.

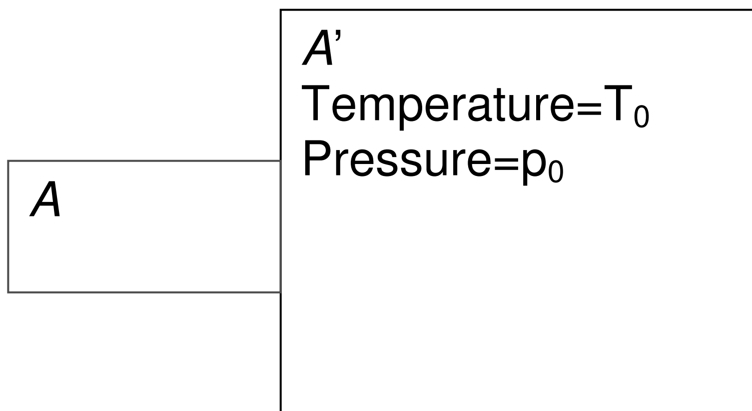

Figure A1-1: System A (in vacuum and at room temperature) in thermal contact with a heat reservoir (system A') at constant temperature T_0 and constant pressure p_0.

If A^0 is a thermally isolated system, S^0, which is the entropy of the combined system (A^0), must satisfy the condition of any spontaneous process i.e. $\Delta S \geq 0$: Now consider

a process where heat Q flows from A' to A. The change in entropy of the whole system can be written as:

$$\Delta S^0 = \Delta S + \Delta S' \geq 0 \qquad \text{... A.1}$$

where ΔS is the change in entropy of system A and $\Delta S'$ is the change in entropy of system A'. Since A absorbs heat from A', the change in entropy of A' can be written as:

$$\Delta S' = \frac{-Q}{T_0} \qquad \text{...A.2}$$

Thus the total change in entropy of the combined system (A^0) is:

$$\Delta S^0 = \Delta S - \frac{Q}{T_0} \qquad \text{...A.3}$$

Applying the 1st law of thermodynamics ($\Delta E=Q-W$) to system A, because the volume of system A alters due to the energy gained, the work done by the system A can be written as: $W=p_0\Delta V+W^*$, where $p_0\Delta V$ is the work done by system A against the constant pressure p_0 of system A' while W^* is any work done by A during the process. Therefore, the change in entropy of the whole system becomes:

$$\Delta S^0 = \frac{\Delta S T_0 - \Delta E_{in} - p_0 \Delta V - W^*}{T_0} \qquad \text{...A.4}$$

Rearranging these leads to: $$\Delta S^0 = \frac{\Delta(S T_0 - E_{in} - p_0 V) - W^*}{T_0} \qquad \text{...A.5}$$

Taking $-G=ST_0-E_{in}-p_0V$, thus $G=E_{in}-T_0S+p_0V$ and $\Delta G=\Delta E_{in}-T_0\Delta S+p_0\Delta V$, where G is the Gibbs free energy. In general [Kub67]:

$$\left(\frac{\partial G}{\partial T}\right)_p = -S \qquad \text{...A.6}$$

$$\left(\frac{\partial G}{\partial p}\right)_T = V \qquad \text{...A.7}$$

Therefore, the total differential equation of G is yielded by:

$$dG = -SdT + Vdp \qquad \text{...A.8}$$

The Gibbs free energy (G) can also be written in term of the enthalpy (H) of system A:

$$H = E + pV \Rightarrow G = H - TS \qquad \text{...A.9}$$

Using the definition of heat capacity at constant pressure:

$$C_p = \left(\frac{\partial Q}{\partial T}\right)_p \qquad \text{...A.10}$$

where $dQ = dE + p_0 dV = dH$

In general the T dependence of H and S at p_0 is given by [Gok96]:

$$\left(\frac{\partial H}{\partial T}\right)_p = C_p \quad \text{And} \quad \left(\frac{\partial S}{\partial T}\right)_p = \frac{C_p}{T} \qquad \text{....A.11}$$

If one integrates equations A.10 and A.11, the change in enthalpy and change in entropy are found respectively as:

$$\Delta H = \int_{T_1}^{T_2} C_p dT \quad \text{and} \quad \Delta S = \int_{T_1}^{T_2} \frac{C_p}{T} dT$$

Since our interest is in the system where the condensed phase and the vapour/gas phase coexist, let us consider the same combined system A^0 with system A that consists of two phases, solid (condensed) and gas (vapour) where system A' remains the same as the previous one in figure A1-1: such a system is schematically shown in figure A1-2 below. In figure A1-2 below, c and g represent the condensed and gas phases respectively.

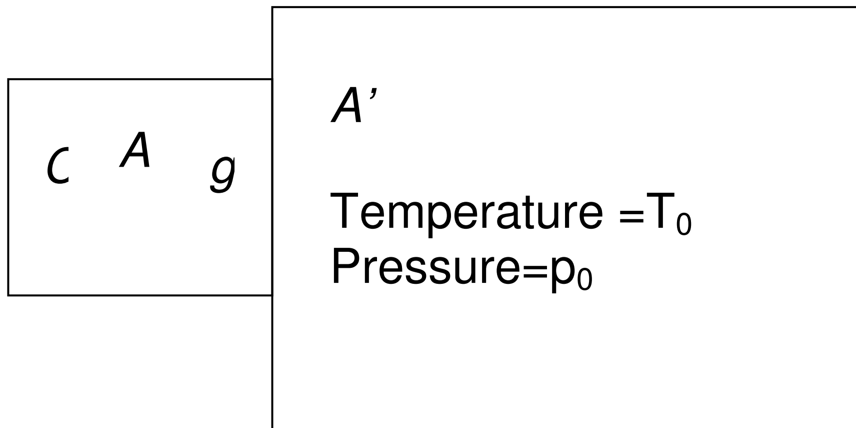

Figure A1-2: System A (where the condensed phase and the gas phase coexist) in thermal contact with a heat reservoir (system A’) at constant temperature T_0 and constant pressure p_0.

The general rule for two or more phases to coexist in equilibrium with each other is that their Gibbs free energy must be minimum, i.e. $\Delta G=0$. To find $\Delta G=0$ for a system consisting of more than one phase, such as system A, the free energy of each phase must be considered separately. This is done by introducing the chemical potential (μ), which for this case is the same as G but refers to 1 g mol. Therefore, for our system, $\Delta G=0$ can be written as:

$$\mu_g-\mu_c=0 \text{ or } \mu_c=\mu \text{ and } d\mu_c=d\mu_g \qquad \text{…A.12}$$

If equation A.8 is substituted into equation A.12 the relationship between vapour pressure (p*) and temperature is established:

$$\begin{aligned} & -S_g\,dT + V_g\,dp = -S_c\,dT + V_g\,dp \\ & \Rightarrow V_c\,dp - V_g\,dp = -S_g\,dT + S_c\,dT \\ & \Rightarrow dp\,(V_c - V_g) = dT\,(-S_g + S_c) \\ & \Rightarrow \frac{dp^*}{dT} = \frac{S_g - Sc}{V_g - V_C} \end{aligned} \qquad \text{…A.13}$$

In equation A.13 above, p* now denotes pressure that changes with temperature and is the vapour pressure of the material. Since the Gibbs free energy can be written in terms of enthalpy (*H*) i.e. $G=H-TS$, the change in entropy in equation A.13 can be written in terms of enthalpy (*H*), with the aid of the relationship in equation A.12:

$$H_g - TS_g = H_c - TS_c$$
$$\Rightarrow -TS_g + TS_c = H_c - H_g$$
$$\Rightarrow T(S_g - S_c) = H_g - H_c$$
$$\Rightarrow S_g - S_c = \frac{H_g - H_c}{T} \quad \text{...A.14}$$

If equation A.14 is substituted into equation A.13, equation A.15, known as Clausius-Clapeyron's equation, is obtained:

$$\frac{dp^*}{dT} = \frac{H_g - H_C}{T(V_g - V_C)} \quad \text{...A.15}$$

Solving this equation could lead to determining the relationship between vapour pressure (p^*) and temperature (T). To solve equation A.15 two assumptions are made. The first one is that the molar volume of a condensed phase is neglected since it is very small compared to the molar volume of vapour while the vapour is assumed to be obeying the ideal-gas law ($pV=nRT$), with n=1 as specified above.

Based on these assumptions: $V_g - V_c \approx V_g = \frac{RT}{p}$ ...A.16

The change in enthalpy in equation A.15 refers to the change of one mole of the condensed phase to the vapour phase, which is termed as the heat of sublimation:

$$H_g - H_c = \Delta H_s \quad \text{...A.17}$$

If equations A.16 and A.17 are substituted back into equation A.15, equation A.18 is obtained:

$$\frac{dp^*}{dT} = \frac{H_g - H_c}{T(Vg)} \Rightarrow \frac{dp^*}{p^*} = \frac{\Delta H_s dT}{RT^2} \quad \text{...A.18}$$

If equation A.18 is firstly integrated to obtain the relationship between p^* and T by assuming that ΔH_s is independent of temperature:

$$\ln \ p^* \approx -\frac{\Delta H_s}{RT} + const \quad \text{...A.19}$$

Now if the same integration is performed from the boiling point (2460K) of silver, where the pressure is assumed to be 1atm (1.0325×10^5 Pa), to the higher temperature (T) with vapour pressure (p*):

$$\int_{1.0132e5}^{p^*} \frac{dp^*}{p^*} = \int_{2460}^{T} \frac{\Delta H_s}{RT^2} dT$$

$$\ln p^* = \Delta H_s \left[4.892e-5 \frac{mol}{J} - \frac{1}{RT} \right] + 11.5261$$

Fitting the experimental values of vapour pressure as a function of temperature for a particular element, ΔH_s can be obtained.

The second assumption considers the changes that the molar specific heat at constant pressure undergoes with T. From this assumption the accurate p* function can be derived because the vapour pressure also alters with T. From this assumption:

$$\left(\frac{\partial H}{\partial T} \right)_p = C_p ; \Rightarrow \frac{d(\Delta H_s)}{dT} = C_{p,g} - C_{p,c} = \Delta C_p \qquad \ldots A.20$$

and by considering that near and above room temperature the specific heat may be expressed generally in the form:

$$C_p = a + bT + cT^{-2} \qquad \ldots A.21$$

where a, b, and c are numerical factors specific to a particular substance, inserting equation A.20 into A.19 leads to:

$$\Delta H_s = \Delta H_s * + \Delta aT + \frac{\Delta bT^2}{2} - \Delta CT^{-1} \qquad \ldots A.22$$

And substituting equation A.21 into A.17 and integrating results in:

$$\ln p^* = -\frac{\Delta H_s *}{RT} + \frac{\Delta a}{R} \ln T + \frac{\Delta b}{2R} T + \frac{\Delta c}{2R} T^{-2} + I \qquad \ldots A.23$$

In equation A.23, I is the integration constant. Fitting the experimental vapour pressure data to the above equation, the relationship between p* and T can be found for particular elements. Fitting the experimental data of silver vapour pressure taken

from Kubaschewski et al. [Kub70], as depicted in figure A1-3, equation A.24 was obtained.

$$\ln p^* = -\frac{428075}{T} - 306\ln T + 0.07T + 8T^{-2} + 2375 \qquad \ldots A.24$$

The equilibrium vapour pressure at 1000 ^{o}C was calculated using equation A.24 and found to be 7.85×10^{-3} Torr. From this equilibrium vapour pressure, the number of atoms condensing and evaporating per unit area per unit time was calculated at 1000 ^{o}C using equation A.25 [Kub67]:

$$\frac{dN}{Adt} = 3.513\times10^{22}(MT)^{\frac{-1}{2}}\, p^* \qquad \ldots A.25$$

where M is the molar mass in grams. The value of 9.47×10^{19} cm^{-2}s^{-1} was found. Taking the annealing time to be 10 h, the number of silver atoms per unit area was found to be 3.41×10^{28} m^{-2}. This value represents the number of silver atoms that are sublimating out and condensing on to the sample during annealing. If these atoms had been condensing on our SiC surface during annealing, they would have been detected by RBS. Therefore, deposited silver is not lost by sublimation but by other mechanisms such as a wetting problem between SiC and silver, which is responsible for the disappearing of deposited layer of silver as discussed in chapter 7.

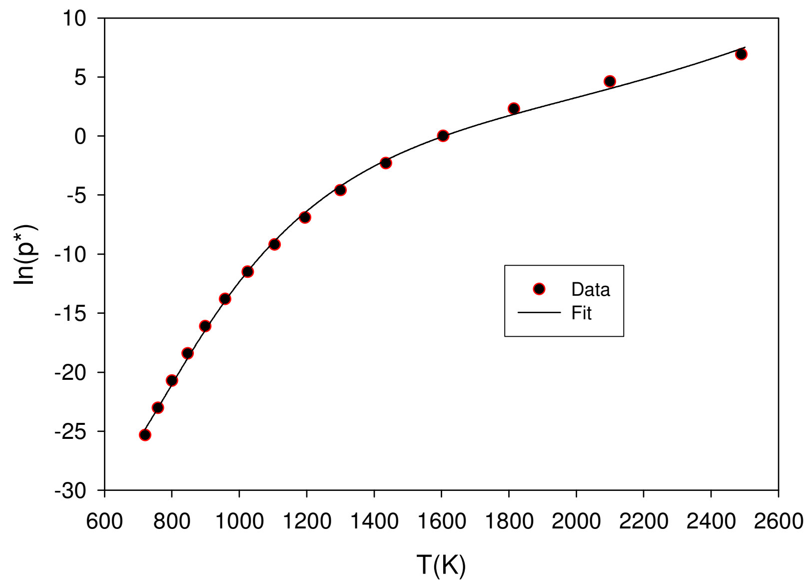

Figure A1-3: The experimental silver vapour data fitted to equation A.23.

9.1 REFERENCES

[Gok96] N. A. Gokcen, and R. G. Reddy, Thermodynamics, 2nd ed., Plenum Press, New York (1996).

[Kub67] O. Kubaschewski, E. LL. Evans, and C. B. Alcock, Metallurgical Thermochemistry. 4th ed., Pergamon Press, New York (1967).

[Mai70] L. I. Maissel and R. Glang, Handbook of Thin Film Technology, McGraw-Hill, New York (1970).

[Rei65] Federick Reif, Fundamentals of Statistical and Thermal Physics, McGraw-Hill, New York (1965).